



저작자표시-비영리-변경금지 2.0 대한민국

이용자는 아래의 조건을 따르는 경우에 한하여 자유롭게

- 이 저작물을 복제, 배포, 전송, 전시, 공연 및 방송할 수 있습니다.

다음과 같은 조건을 따라야 합니다:



저작자표시. 귀하는 원저작자를 표시하여야 합니다.



비영리. 귀하는 이 저작물을 영리 목적으로 이용할 수 없습니다.



변경금지. 귀하는 이 저작물을 개작, 변형 또는 가공할 수 없습니다.

- 귀하는, 이 저작물의 재이용이나 배포의 경우, 이 저작물에 적용된 이용허락조건을 명확하게 나타내어야 합니다.
- 저작권자로부터 별도의 허가를 받으면 이러한 조건들은 적용되지 않습니다.

저작권법에 따른 이용자의 권리는 위의 내용에 의하여 영향을 받지 않습니다.

이것은 [이용허락규약\(Legal Code\)](#)을 이해하기 쉽게 요약한 것입니다.

[Disclaimer](#)

Master's Thesis

**A multi-wavelength study of N63A:  
A supernova remnant within an H II region in the  
Large Magellanic Cloud.**

**N63A 다중파장 연구:  
대마젤란운(LMC) H II 영역 내 초신성 잔해**

August 2017

Graduate School of Seoul National University  
Department of Physics and Astronomy - Astronomy Program  
Rommy L.S.E. Aliste Castillo



**A multi-wavelength study of N63A:  
A supernova remnant within an H II region in  
the Large Magellanic Cloud.**

**N63A 다중파장 연구:  
대마젤란운(LMC) H II 영역 내 초신성 잔해**

Academic Advisor Bon-Chul Koo

Submitting a Master's Thesis of Astronomy

April 2017

Graduate School of Seoul National University

Department of Physics and Astronomy - Astronomy Program

Rommy L.S.E. Aliste Castillo

Confirming the Master's Thesis written by Rommy  
L.S.E. Aliste Castillo

June 2017

Committee:

Professor	Myungshin Im
Professor	Bon-Chul Koo
Professor	Woong-Tae Kim

*“No te rindas, por favor no cedas,  
aunque el frío queme,  
aunque el miedo muerda,  
aunque el sol se ponga y se calle el viento,  
aún hay fuego en tu alma,  
aún hay vida en tus sueños,  
porque cada día es un comienzo,  
porque esta es la hora y el mejor momento...”*

No te rindas, Mario Benedetti.

# Abstract

The nature and physical environments of SNRs are diverse, and for this reason, the understanding of the properties of nearby SNRs is useful in interpreting the emission from SNRs in remote galaxies where we cannot resolve them. In this regard, the LMC is a unique place to study SNRs due to its proximity, location, and composition compared with our galaxy.

We carried out a multi-wavelength study of SNR N63A in the LMC, a young remnant of the SN explosion of one of the most massive ( $> 40 M_{\odot}$ ) stars in a cluster. It is currently expanding within a large H II region formed by OB stars in the cluster and engulfing a molecular cloud.

First, we aimed to study the overall structure of N63A using NIR imaging and spectroscopic observations of SNR N63A. In the [Fe II] images we detected a two-lobed structure, which has a good spatial correlation with the shock-heated lobes of N63A's optical nebula. We have detected several [Fe II] lines as well as He I, H I and [P II] lines from the emitting region. This allows us to estimate the electron density ( $\sim 4700 \text{ cm}^{-3}$ ) and a smaller extinction ( $A_V \sim 0.5 \text{ mag}$ ). We also estimate the pre-shock number density of  $\sim 30 \text{ cm}^{-3}$  assuming a shock speed of  $100 \text{ km s}^{-1}$  in the [Fe II] emitting region of the SNR.

Second, we present the results of a study of the molecular gas associated with the SNR N63A. We use SEST  $^{12}\text{CO}$  J = 1-0 and 2-1 observations, which provide evidence in support of the existence of physical interaction between the SN shocks and the adjoining molecular clouds. For the cloud which is interacting with the SNR N63A, we reported a mass of  $\sim 1.2 \times 10^3 M_{\odot}$ , which is almost three times larger than the previous mass reported using X-ray observations,

and a hydrogen column density of  $N_H \sim 1.4 \times 10^{21} \text{ cm}^{-2}$ , which is 4 times smaller than the total column density derived using our NIR observations.

We also present detection of shocked  $\text{H}_2$  emission in NIR and MIR using the Spitzer IRS observations. The  $\text{H}_2$  excitation diagram shows a best-fit with a two-temperature LTE model with the temperatures of 200-300 K and 700-900 K. Comparison of  $\text{H}_2$  emission with shock models shows that slow C-shock models fit well to the warm component.

In addition to the [Fe II] features, we also detected  $\text{H}_2$  2.12  $\mu\text{m}$  emission from a region with spatial correlation with the [Fe II] emitting region. Although the molecular and ionic shocks arise from the same region, we interpret that Fe II and  $\text{H}_2$  emission are tracing independent shocks in N63A based on their properties.

Finally, we studied the environment of SNR N63A in order to investigate its interaction with its ambient medium. We found a half “ring-like” structure with an average brightness of  $\sim 2 \times 10^{-5} \text{ erg cm}^{-2} \text{ s}^{-1} \text{ sr}^{-1}$  in  $\text{H}\alpha$ , at a distance of 11 - 19 pc from the center of the SNR. This structure can correspond to circumstellar material produced by the mass loss of the N63’s progenitor or by the neighboring OB stars. Another possibility is that this structure is part of the ISM and it is not related to the SNR.

**Keywords:** ISM: supernova remnant - ISM: individual (N63A) - ISM: molecular clouds

**Student Number:** 2015-22234

# Contents

<b>Abstract</b>	<b>i</b>
<b>List of Figures</b>	<b>v</b>
<b>List of Tables</b>	<b>vii</b>
<b>Chapter 1 Introduction</b>	<b>1</b>
1.1 Supernova Remnants . . . . .	1
1.2 Large Magellanic Cloud . . . . .	2
1.3 N63A: a SNR within an H II region in the LMC . . . . .	3
1.3.1 N63A's environment . . . . .	3
1.3.2 SNR N63A . . . . .	4
1.4 Interaction of SNR N63A with Molecular Clouds . . . . .	8
1.5 Purpose of Thesis . . . . .	9
<b>Chapter 2 Near-Infrared line mapping and spectroscopy of the           SNR N63A</b>	<b>12</b>
2.1 Introduccion . . . . .	12
2.2 Observations and Data Reduction . . . . .	14
2.2.1 NIR narrow-band images . . . . .	14

2.2.2	NIR spectra . . . . .	15
2.3	Results . . . . .	17
2.3.1	Distribution of [Fe II] and [P II] emission in N63A . . . . .	17
2.3.2	NIR Extinction . . . . .	19
2.3.3	Relative Abundance and dust destruction . . . . .	22
2.3.4	NIR [Fe II] lines and electron density . . . . .	25
2.4	Discussion . . . . .	36
2.4.1	Extinction . . . . .	36
2.4.2	De-reddened NIR emission . . . . .	36
2.4.3	Shock Parameters . . . . .	37

**Chapter 3 SNR N63A interacting with Molecular Clouds in the LMC** **40**

3.1	Introduccion . . . . .	40
3.2	Observations and Data . . . . .	42
3.2.1	CO emission lines . . . . .	42
3.2.2	H <sub>2</sub> 2.12 $\mu$ m narrow-band . . . . .	43
3.2.3	Ancillary data . . . . .	43
3.3	Results . . . . .	45
3.3.1	Distribution of molecular clouds in the environs of N63A . . . . .	45
3.3.2	Molecular cloud masses and gas column densities . . . . .	49
3.3.3	Observations of Molecular Hydrogen in SNR N63A . . . . .	51
3.3.4	H <sub>2</sub> excitation diagram of N63A . . . . .	54
3.4	Discussion . . . . .	56
3.4.1	Excitation of Molecular Hydrogen . . . . .	56
3.4.2	Implication of Shock Models from Molecular Hydrogen . . . . .	60
3.4.3	Comparison of Molecular and Ionic Shocks . . . . .	66

3.4.4	The photoionized region of N63A . . . . .	67
<b>Chapter 4</b>	<b>SNR N63A clues to its Progenitor</b>	<b>70</b>
4.1	Introduction . . . . .	70
4.2	SNR N63A's environment . . . . .	71
4.3	Observational Data . . . . .	74
4.4	Results and Discussion . . . . .	74
<b>Chapter 5</b>	<b>Summary and Conclusion</b>	<b>83</b>
	<b>Bibliography</b>	<b>88</b>
	<b>초록</b>	<b>92</b>
	<b>Acknowledgements</b>	<b>94</b>

# List of Figures

Figure 1.1	<i>Image of N63 H II region in H<math>\alpha</math> narrowband.</i> . . . . .	5
Figure 1.2	<i>Three color map of N63A from Warren et al. 2003.</i> . . . . .	7
Figure 1.3	<i>Schematic structure of N63A and surroundings.</i> . . . . .	11
Figure 2.1	<i>SIRIUS/IRSF [Fe II]<sub>1.64<math>\mu</math>m</sub> narrow-band image of the two-lobed structure of N63A showing the slit positions where the spectra were obtained.</i> . . . . .	17
Figure 2.2	<i>NIR narrow-band images in comparison with a color map composed of HST images.</i> . . . . .	19
Figure 2.3	<i>[Fe II]<sub>1.26/1.64<math>\mu</math>m</sub> ratio map.</i> . . . . .	21
Figure 2.4	<i>[P II]<sub>1.19<math>\mu</math>m</sub>/[Fe II]<sub>1.26<math>\mu</math>m</sub> ratio map.</i> . . . . .	24
Figure 2.5	<i>Spectra of N63A obtained in J-band using IRIS2/AAT.</i> . . . . .	28
Figure 2.6	<i>Spectra of N63A obtained in H-band using IRIS2/AAT.</i> . . . . .	29
Figure 3.1	<i>Regions where the spectral maps of SNR N63A were obtained using the Spitzer IRS.</i> . . . . .	44
Figure 3.2	<i>Integrated <sup>12</sup>CO<sub>2-1</sub> emission line of the N63A region observed with the SEST.</i> . . . . .	46

Figure 3.3	<i>H<math>\alpha</math> image of the N63 H II region with <math>^{12}\text{CO}_{2-1}</math> and Chandra X-ray contours overlaid. . . . .</i>	48
Figure 3.4	<i>H<math>_2</math> <math>2.12\mu\text{m}</math> line map observed with SIRIUS/IRSF. . . . .</i>	52
Figure 3.5	<i>Distribution of the [Fe II]<math>_{1.64\mu\text{m}}</math> and H<math>_2</math> <math>2.12\mu\text{m}</math> emission along the N63A's two-lobes. . . . .</i>	53
Figure 3.6	<i>H<math>_2</math> excitation diagram of N63A. . . . .</i>	56
Figure 3.7	<i>Two-temperature LTE model fitted to the H<math>_2</math> excitation diagram . . . . .</i>	59
Figure 3.7	<i>Continued. . . . .</i>	60
Figure 3.8	<i>C-shock fitted to the observed excitation of H<math>_2</math> corresponding to the warm component of N63A. . . . .</i>	63
Figure 3.8	<i>Continued. . . . .</i>	64
Figure 3.9	<i>C-shock fitted to the observed excitation of H<math>_2</math> corresponding to the hot component of N63A. . . . .</i>	65
Figure 3.10	<i>C-shock fitted to the observed excitation of H<math>_2</math> corresponding to the warm component to the SW lobe of N63A. . . . .</i>	69
Figure 4.1	<i>Brightest members of the OB Association NGC 2030. . . . .</i>	73
Figure 4.2	<i>H<math>\alpha</math> emission of the N63 HII region showing a "ring-like" structure' around N63A. . . . .</i>	75
Figure 4.3	<i>Paths where the H<math>\alpha</math> brightness distribution was measured across the H II region. . . . .</i>	77
Figure 4.4	<i>Plots showing the H<math>\alpha</math> brightness variation across the N63 H II region. . . . .</i>	79
Figure 4.4	<i>Continued. . . . .</i>	80

# List of Tables

Table 2.1	<i>Specifications of SIRIUS/IRSF narrow-bands.</i> . . . . .	15
Table 2.2	<i>Emission lines identified in J-band.</i> . . . . .	26
Table 2.3	<i>Emission lines identified in H-band.</i> . . . . .	27
Table 2.4	<i>De-reddened lines and flux correction for spectral lines in J-band.</i> . . . . .	31
Table 2.5	<i>De-reddened lines and flux correction for spectral lines in H-band.</i> . . . . .	32
Table 2.6	<i>NIR line ratios obtained in N63A.</i> . . . . .	34
Table 2.7	<i>Electron densities.</i> . . . . .	35
Table 3.1	<i>Molecular clouds identified in the SNR N63A region.</i> . . . .	45
Table 3.2	<i>Physical parameters of the Clumps.</i> . . . . .	50
Table 3.3	<i>Observed H<sub>2</sub> lines in the N63A region.</i> . . . . .	55
Table 3.4	<i>Fitted Excitation Parameters to Observed Molecular Hydrogen Lines.</i> . . . . .	57
Table 4.1	<i>Brightest members of NGC 2030.</i> . . . . .	72
Table 4.2	<i>Brightness distribution of the H<math>\alpha</math> emission through the N63 HII region.</i> . . . . .	78

# Chapter 1

## Introduction

### 1.1 Supernova Remnants

Supernova (SN) explosion plays a major role in the evolution of the interstellar medium (ISM) and regulates the star formation rate in galaxies (e.g., Kim and Ostriker, 2015). When a SN occurs, stellar material is ejected outward at speeds that approach a fraction of the speed of light ( $\sim 0.01c - 0.1c$ ), distributing heavy elements throughout the ISM. Consequently, a shock wave propagates, which has the effect of heating the ISM, and also can destroy the dust grains, introducing heavier elements into the ISM, while atoms can be ionized and excited. For that reason, supernova remnants (SNRs) are an ideal astrophysical laboratory for studying the physical conditions of shock heated interstellar gas. In a typical remnant one finds both, a hot ( $T > 10^6$  K) component emitting mainly in X-rays and denser, cooler one ( $T \sim 10^4$  K) where the recombining gas emits strong lines and is therefore cooling rapidly (e.g. Mckee and Hollenbach, 1980).

Supernova explosions strongly affect the environment, and at the same time, the evolution of a SNR is strongly governed by the environment itself. Due to massive stars are formed by the gravitational collapse of molecular clouds (MCs), supernovae are expected to explode in the same dense environment where their progenitors born, because massive stars cannot drift far away from the star-forming region due to their very short life-times. As a result, we expect to find several SNRs interacting with MCs. The interaction of SNRs with dense MCs is of considerable interest because it provides an opportunity to study important topics such as: (1) the role of SN feedback in star formation and molecular cloud disruption, as well as (2) the complex physical and chemical processes associated with the shocks. The shock manifests itself in X-rays, radio synchrotron radiation, optical and infrared (IR) fine structure lines and the heating and sputtering of dust grains, whilst the molecular cloud reveals itself by rotational emission from CO.

In spite of the above prediction, there are still very few cases where the SNR-MC interaction have been well proven and investigated (e.g. *W44*, Seta et al. 1998, Reach et al. 2005, Anderl et al. 2014; *IC 443*, van Dishoeck et al. 1993; *W28*, Reach et al. 2005; *W51C*, Koo & Moon 1997; *3C 391*, Reach & Rho 1996, 1999; *HB21*, Koo et al. 2001, Shinn et al. 2010; and some others). This situation limits our understanding of the shocks driven into MCs by SNRs, and of the transition to other phases from the molecular phase that carries about half of the mass of the ISM.

## 1.2 Large Magellanic Cloud

We know about 274 SNRs in the Milky Way, and about half of them are expected to be in physical contact with MCs. However, about 20% of the known

galactic SNRs have been found to show some evidence for the interaction with MCs (Jiang et al. 2010; Froebrich et al. 2015). In our galaxy, most SNRs are located in the Galactic plane, and therefore there is usually contamination from foreground/background sources, which hampers the study of SNRs and limits the usefulness of the galactic SNRs. In this regard, SNRs in nearby galaxies are ideal targets for this kind of researchs.

The Large Magellanic Cloud (LMC) is a unique place to investigate SNRs due to their proximity ( $\sim 50$  kpc, the nearest gas-rich galaxy), which makes possible to observe the detailed structure of the SNRs; and their location (nearly face-on geometry and far-off from the galactic plane), and thus it is possible to obtain unbiased samples. Besides, the composition of the LMC is different compared with our galaxy: its metallicity is lower by a factor two, the dust-to-gas ratio is four times lower than in our galaxy, and also the dust composition is different. According to this, we can expect that the SNRs-MCs interaction will be different in such environmental conditions. In addition, over 60 SNRs are known in the LMC, and 15 of them are near to molecular clouds (Banas et al. 1997, Desai et al. 2010). Due to the nature and the physical environments of SNRs are diverse, the understanding of the properties of nearby SNRs (Magellanic and Galactic SNRs) is useful in interpreting the emission from SNRs in remote galaxies where we cannot resolve them.

## **1.3 N63A: a SNR within an H II region in the LMC**

### **1.3.1 N63A's environment**

In this research we aim at studying one of the most interesting SNRs in the LMC: N63A ( $\alpha$ :  $05^h 35^m 44.1^s$ ,  $\delta$ :  $-66^\circ 02' 14''$ , J2000), which is an unique example that it is possible to study without confusion from other sources along

the line of sight. This SNR is embedded in an extended classical H II region, with dimensions:  $\sim 6' \times 9'$ , called N63 (Henize 1956) or DEM 243 (Davies, Elliott & Meaburn, 1976) as can be seen in Figure 1.1. Also, this remnant was the first confirmed case of a SNR within an H II region.

The H II regions are composed primarily of ionized hydrogen atoms ( $H^+$ ) and other ions. These emission nebulae contain clusters with dozens of massive OB stars that input energy via ionizing radiation and stellar winds. The powerful UV radiation from these stars is responsible for photo-dissociating and photo-ionizing the once molecular clouds within which the stars were born. The energy feedback shapes their interstellar surroundings, which are the birthplaces of the next generation of stars. Thus, these emission nebulae trace key transformative processes in a galaxy. In this case, N63 contains the OB association NGC 2030 or LH83 (Lucke & Hodge, 1970), which is loosely distributed in the northern half of this H II region.

In addition, N63 also contains 14 young stellar objects (YSOs): 9 Class I, 2 flat spectrum, and 3 Class II, within  $3.5'$  ( $\sim 51$  pc) from the center of its ionizing cluster NGC 2030 (Caulet et al. 2008) and concentrated within the boundaries of the ionized front region (IF). The IF on the eastern border is delineated by a curved, knotty filament of strong mid-IR emission due to hot dust + polycyclic aromatic hydrocarbons (PAHs) dust grains. This mid-IR emission arises in the photodissociation region (PDR), which forms a broad shell around the H II region.

### 1.3.2 SNR N63A

N63A is the second brightest SNR in the LMC and was first identified as a SNR by Mathewson & Healy (1964) on the basis of its non-thermal radio spectrum. N63A is a young ( $2 - 5 \times 10^3$  yr, Hughes et al. 1998) remnant, which is believed

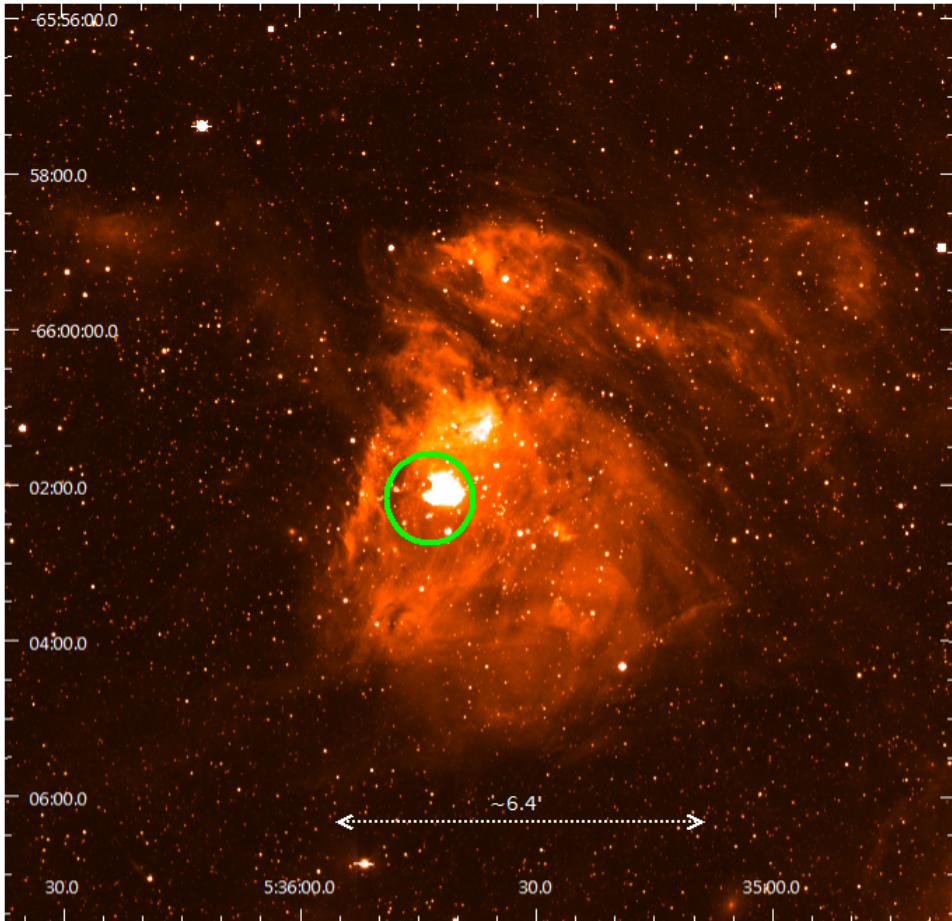


Figure 1.1: *Image of N63 H II region in H $\alpha$  narrowband. The green circle indicates the size and position of the SNR N63A, which is embedded in the northeastern quadrant of the H II region.*

to be the product of the SN explosion of one of the most massive stars in the OB association NGC 2030. The currently most luminous star in NGC 2030 is a O7 star with a mass of  $\sim 40 M_{\odot}$ , therefore the progenitor of N63A's supernova was probably more massive than this and with a main sequence spectral type earlier than O7 (Oey 1996).

The N63A's morphology varies strongly across the wave bands (see Figure 1.2). In X-ray, where the emission is consistent with swept-up ISM, the size of the remnant is about 70" diameter, which is  $\sim 3$  times the size of the N63A's optical nebula, and defines the size of the SNR. Although many SNRs are more extended sources in X-ray than in optical, the unusually large discrepancy in N63A is further incentive to understand its complex morphology. The properties of the X-ray emitting plasma in N63A are an electron density of  $n_e = 4.35 \text{ cm}^{-3}$  and a temperature of  $T_e = 0.78 \text{ keV}$  (Warren et al. 2003, using an estimated age of 3500 yr).

In optical the remnant appears as a three-lobed structure with a size of 23" (approximately 5.3 pc at the LMC distance of  $\sim 50 \text{ kpc}$ ). However optical spectroscopic observations show that only the north and southeastern (NE; SE) lobes, which have high  $[\text{S II}]/\text{H}\alpha$  ratios, are shock-heated as a result of interactions with the ISM rather than with SN ejecta (Russell & Dopita 1990), while the southwestern (SW) lobe is a photoionized H II region (Levenson et al. 1995). Also, optical imaging observations show a distinct filamentary structures indicative of a compression by SNR shocks in the two eastern lobes, whereas the western lobe shows only diffuse ionized gas and dust clouds. Moreover, in radio the remnant appears as a thick shell with a similar size than in X-ray ( $\sim 65''$ ), where its brightest emission is coincident with the two shock-heated lobes (Dickel et al. 1993).

In IR bands N63A is seen with a similar structure as in optical, with an interior concentration of material that is evident at all available wavelengths. Besides, the  $24 \mu\text{m}$  MIPS observation reveals that the extended emission in the N63A plasma (i.e., the emission over the entire X-ray/radio shell of the SNR) and in the SW optical lobe is largely due to thermal continuum emission from dust (90%), whereas the mid-IR line emission from gas in the NE and SE

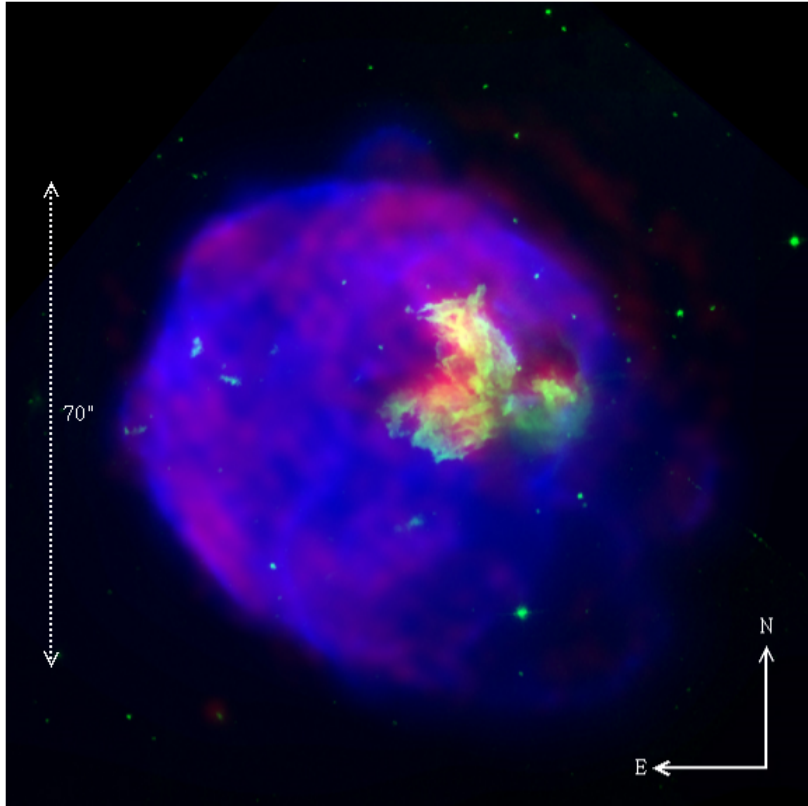


Figure 1.2: *N63A* composed image from: 8638 MHz ATCA radio (red), HST *H $\alpha$*  optical (green), and broadband Chandra X-ray (blue) images (Warren et al. 2003).

optical lobes contributes about half of the MIPS 24  $\mu\text{m}$  flux: 53% and 44%, respectively (Seok et al. 2013).

SNR N63A also shows some special features which are also a further motivation to study this object. For example, the spectral energy distribution (SED) of the SW (photoionized) lobe in IR is unexpectedly similar to the SED of the SE (shocked) lobe, while the NE lobe shows the most different SED from the others (William et al. 2006). Furthermore, the X-ray emission shows several

“crescent” shaped structures located beyond the main shell, that resemble similar features seen in other SNR ( e.g. in Vela SNR), which have been interpreted as arising from high speed clumps of SN ejecta interacting with the ambient medium (Warren et al. 2003). Additionally, a roughly “triangular hole” is seen in the Chandra X-ray observations near to the location of the optical lobes (which is also coincident with the brightest emission in radio), as well as the fact that the X-ray center is offset about 13” (3 pc) to the southeast of the optical nebula’s center of the remnant.

## 1.4 Interaction of SNR N63A with Molecular Clouds

Various observations indicate that the bright optical nebula inside N63A is a molecular cloud swept up by the SNR. First, the cloud is seen in absorption in X-ray (blocks of 80% to 98%; Warren et al. 2003), where these observations reported a mass of  $450 M_{\odot}$  and a mean density of  $\sim 250 \text{ cm}^{-3}$  for the cloud. Second, observation of only blueshifted emission from the shock-heated lobes, with a maximum expansion velocity of  $250 \text{ km s}^{-1}$  around the edges (Shull 1983), which supports the idea of shocks are being driven into the near side of the cloud. In addition, the IRAC observations indicates color ranges for molecular shocks, as well as the IRS spectra of the three-lobed region, which shows several  $\text{H}_2$  lines with dominant ionic lines and PAHs features (William et al. 2006). In fact, the transitional  $\text{H}_2$  lines are a clear sign of the interaction with a MC, because these lines are originated from the warm gas behind the part of the shock front expanding into the MC, where high columns of  $\text{H}_2$  can survive the passage of the shock.

As previously stated, the interaction SNR-MC in N63A is limited to a portion of the SNR, which resembles similar cases seen in some galactic SNRs (e.g.

*G349.7+0.2*, Dubner et al. 2004; *IC 443*, van Dishoeck et al. 1993). However, so far, CO surveys no reveal significant MC associated with this remnant (e.g. Cohen et al., 1988; Israel et al. 1993). Only the NANTEN 4m telescope CO map (Yamaguchi et al., 2001) detected a small cloud on the eastern border of this remnant.

Studies of SNR N63A across the wave bands should help us to confirm this scenario and provide deeper insights into the interaction of SNRs with their environments.

## 1.5 Purpose of Thesis

In summary, N63A is a young remnant of the SN explosion of one of the most massive ( $>40 M_{\odot}$ ) stars in a cluster in the LMC. It is currently expanding within a large H II region formed by OB stars in the cluster and engulfing a molecular cloud. As such N63A is a prototypical SNR showing the impact of SN explosion on the cluster and its environment. Figure 1.3 shows a schematic structure of SNR N63A and its environment.

The study of SNR N63A makes raise many questions such as: why N63A's optical emission region is much smaller than the SNR extent?, why there are differences between the NE and SE shocked lobes seen in IR bands?, or which are the physical and chemical processes associated with the shocks in this region?, among others questions. This research has been conducted in order to find answers to these and other questions, allowing us to improve our knowledge about SNR N63A and supernova remnants, in general, as well as how works their interaction with MCs.

The main objectives of this thesis are as follows:

- (1) Understand the overall structure of the SNR using the information ob-

tained in different wavelengths. To achieve this goal we carry out a detailed research using near-infrared (NIR) imaging and spectroscopic observations to obtain physical parameters and investigate the atomic shocks.

Besides, the interaction of SNRs with dense MCs is of considerable interest because it provides an opportunity to study important topics such as: MC disruption, and the complex physical and chemical processes associated with the shocks. As mentioned above, in SNR N63A there are evidence of both atomic and molecular shocks, but their physical relation is still uncertain and hence the shock parameters are unknown. Most of the evidence indicate that the bright optical nebula inside the SNR N63A corresponds to a molecular cloud swept-up by the SNR. For this reason, the second goal is: (2) understand how the supernova remnant- molecular cloud interaction works and reveal the structure of the shocked cloud as well as the consequences of the impact of the SNR shock on the molecular cloud.

Finally, we know that the SNR N63A is embedded in a HII region, and also that the progenitor of N63A was a star of an OB association, which mass is known. In addition, SNRs can probe earlier stages of stellar evolution of its progenitor, as they interact with the bulk of circumstellar material expelled by its progenitor during pre-SN mass loss over long timescales. For this reason the third objective is: (3) study the physical properties of the environment of SNR N63A in order to understand the interaction of N63A with its ambient medium.

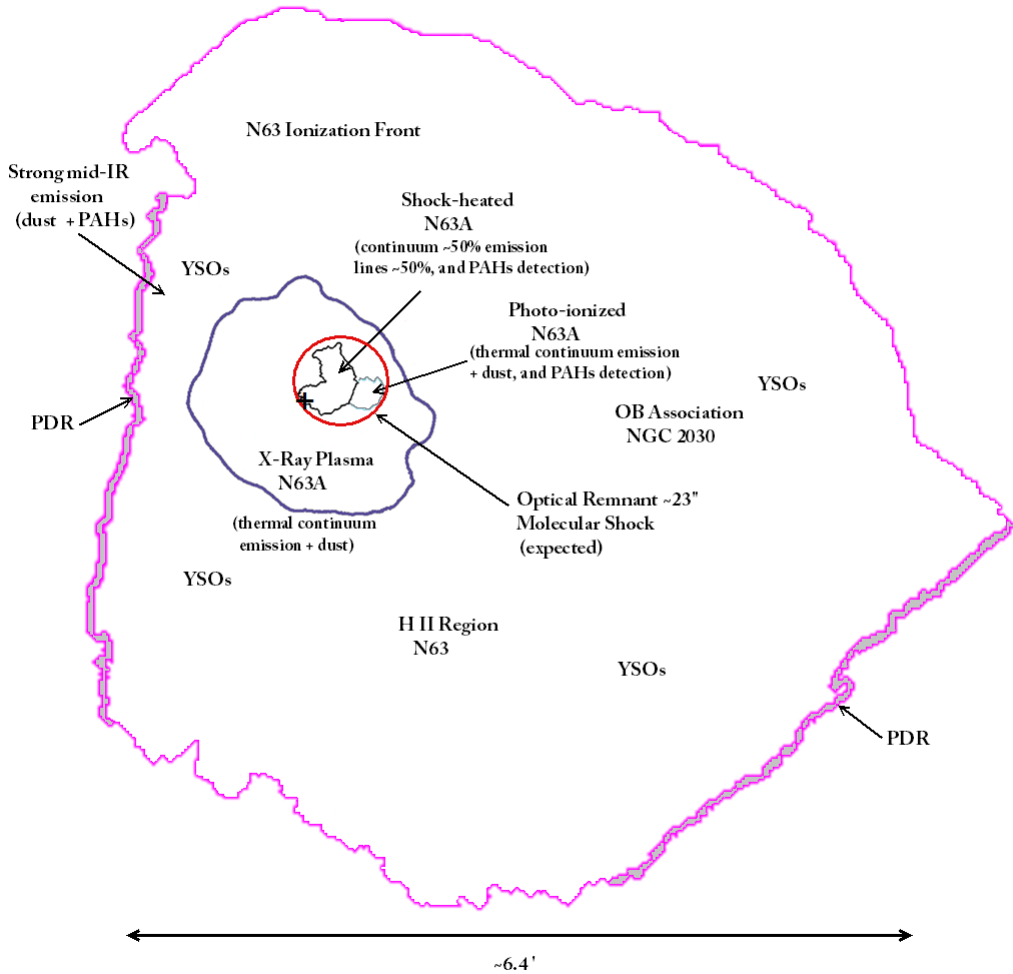


Figure 1.3: *Schematic structure of N63A and surroundings. The contours represent: the X-ray plasma of N63A (blue), which define the size of the supernova remnant; the optical two-lobed structure (black) and photoionized lobe (cyan); and the approximate boundaries of the H II region N63 (magenta). The red circle indicates the estimated region where we expect to find the SNR-MC interaction.*

## Chapter 2

# Near-Infrared line mapping and spectroscopy of the SNR N63A

### 2.1 Introduccion

Supernova remnants (SNRs) are strong thermal emitters of infrared (IR) radiation. IR observations are used to study morphology of SNRs, interaction between SN shocks and ambient medium, and especially physical processes associated with dust grain, because these, either newly synthesized or swept-up by SN shocks, radiate essentially only in IR. Mostly, the IR emission in SNRs is dominated by either line emission (ionic lines from forbidden lines of some elements such as Fe, O, Ne ions or hydrogen recombination lines; and/or molecular lines, principally molecular hydrogens lines) or thermal dust emission.

In NIR spectra of SNRs, [Fe II] emission lines are usually the most prominent and they can be used as tracer of fast radiative atomic shocks. The Fe<sup>+</sup> ion has many levels with low excitation energies, so that these levels are easily excited in shocked gas and the transitions among them result in many lines in

IR, particularly in the NIR bands. Also, [Fe II] is favored in zones of partially ionized hydrogen in which the  $\text{Fe}^+$  ions are excited by electron collisions. On the other hand, [Fe II] lines are hardly visible in H II regions due to the ionization potential for  $\text{Fe}^+$  (16.2 eV) is too low for most of the  $\text{Fe}^+$  ions to survive in a fully ionized hydrogen gas. Partially ionized zones are large when the gas is heated by X-rays (power-law photoionization), which is the characteristic mechanism of active galactic nuclei, or by shocks, where the Fe is ionized to  $\text{Fe}^+$  by FUV radiation from the shock front while H atom are mostly neutral. The last mechanism is dominant in SNRs and starburst galaxies. This peculiarity has been predicted by theoretical models of shock fronts (e.g. Mckee et al., 1984; Shull & Draine, 1987) where the ratio  $[\text{Fe II}]/\text{H}\beta$  is found to be a useful indicator of the efficiency of the shock front in destroying dust grains. In addition, the increased abundance of gas phase iron by shock-induced sputtering of the dust grains and/or the creation of an extensive partially ionized zone by shock heating can substantially enhance the [Fe II] emission.

There are many [Fe II] lines which are visible in the NIR JHK bands; these include the two strongest lines at 1.257 and 1.644  $\mu\text{m}$ . There are two direct applications of [Fe II] lines. First, the ratios of these lines provide a very good density diagnostic. Second, the extinction to the emitting region can be accurately measured from these lines. A major uncertainty in these applications is from atomic constants.

Besides, the gas-phase Fe abundance  $x(\text{Fe})$  is a measure of the shock efficiency in disrupting the cores of the dust grains where iron is locked in quiescent conditions. In this regard, a powerful way to estimate the percentage of gas-phase iron is based on [Fe II]/[P II] line ratio, which has been proposed by Oliva et al. (2001). Due to phosphorus and iron have similar ionization potentials and radiative recombination coefficients, they are expected to be in the first ionized

state in comparable percentages. Also, the NIR lines of Fe II and P II have similar excitation energies and critical densities, and therefore they are excited in similar physical conditions.

This chapter is organized as follows. Section 2.2 presents the NIR spectroscopic observations using IRIS2/AAT and SIRIUS/IRSF narrow-band images of SNR N63A. In section 2.3, we estimated the extinction toward N63A and the electron density using the information obtained from the [Fe II] emission lines detected in this SNR. In addition, we derived the percentage of gas-phase iron using the [P II] emission detected in N63A. Finally, in section 2.4 we analyzed the atomic shock parameters.

## 2.2 Observations and Data Reduction

### 2.2.1 NIR narrow-band images

We observed N63A with the NIR camera SIRIUS (Simultaneous Infrared Imager for Unbiased Survey) aboard the IRSF (Infrared Survey Facility) 1.4 m telescope, which is located at the South African Astronomical Observatory (SAAO) on May 2016. The SIRIUS camera has a field of view of  $7.7' \times 7.7'$  with a pixel scale of  $0.45''$ .

We obtained images using three different narrow-band filters: [Fe II] $_{1.26\mu m}$ , [Fe II] $_{1.64\mu m}$  and [P II] $_{1.19\mu m}$ . The specifications of each filter are listed in Table 2.1. The standard data reduction procedure was applied to the images (e.g. dark subtraction, flat-fielding, sky subtraction, and dithered-image-combining).

We also performed photometric calibration making comparison with the 2MASS Point Source Catalog. We used H-band magnitudes for the photometric calibration of the [Fe II] $_{1.64\mu m}$  image and J-band magnitudes for the photometric calibrations of the [Fe II] $_{1.26\mu m}$  and [P II] $_{1.19\mu m}$  narrow-band images, assuming

that the magnitude of each star is the same between the corresponding band and filter image. The uncertainties of the photometric calibration coefficients are:  $\sim 6\%$  for the  $[\text{Fe II}]_{1.64\mu\text{m}}$  image, and  $\sim 5\%$  for the  $[\text{Fe II}]_{1.26\mu\text{m}}$  and  $[\text{P II}]_{1.19\mu\text{m}}$  images.

Table 2.1: *Specifications of SIRIUS/IRSF narrow-bands.*

Filter	$\lambda_{iso}$ ( $\mu\text{m}$ )	$\lambda_0$ ( $\mu\text{m}$ )	$\Delta\lambda$ ( $\text{\AA}$ )	total exposure time (s)
$[\text{Fe II}]_{1.26\mu\text{m}}$	1.2642	1.2611	278.1	3000 (60 s x 50)
$[\text{P II}]_{1.19\mu\text{m}}$	1.1897	1.1887	268.3	900 (30 s x 30)
$[\text{Fe II}]_{1.64\mu\text{m}}$	1.6662	1.6436	297.6	900 (30 s x 30)

### 2.2.2 NIR spectra

NIR spectroscopic observations of SNR N63A ( $\alpha$ : 05 h 35 m 44.1 s and  $\delta$ :  $-66^\circ 02' 14''$ , J2000) were carried out using the Infrared Imager and Spectrograph (IRIS2) aboard the 3.9 m Anglo Australian Telescope (AAT) on March 2011. IRIS2 is a NIR imager and spectrograph based on a HAWAII1 HgCdTe detector, covering a  $7.7' \times 7.7'$  field of view with a  $0.4486''$  pixel scale, and long-slit spectroscopy at  $\lambda/\Delta\lambda \approx 2400$  in each of the passbands.

The observations were obtained in four different slit positions (see Figure 2.1): E1, E2 (at  $5''$  east from E1), E3 (at  $5''$  east from E2) and E4 (at  $5''$  east from E3), using a slit width of  $1''$  in J ( $1.04\text{-}1.28 \mu\text{m}$ ) and H ( $1.46\text{-}1.82 \mu\text{m}$ ) spectral bands. The total exposure time was 960 s ( $16 \times 60$  s) per each band. One “off” frame at a sky position well displaced from the target is taken for each “on” frame in an on-off-off-on pattern, per each slit position. Besides, spectra of a G2 V standard star, HIP023984, were obtained in J- and H-band to calibrate

the spectra by flux using the same on-off-off-on pattern, with a total exposure time of 94 s (4 x 24 s) per each band.

For the basic data reduction, we corrected the spectra using the flat-on and -off and also masked the bad pixels. Furthermore, we combined the spectra in a single outputs taking the appropriate dither offsets corrected by distortion using the distortion coefficient derived for each filter. Thereafter, we subtracted sky background and performed the wavelength calibration using OH lines as reference. The spectra (corresponding to the on-off-off-on pattern per each slit position) were combined using median and divided by the exposure time. We followed the same procedure to reduce the data of the G2 V HIP023984 star. However, for the star spectra, the “off” frames are lower than the “on” frames which means that the guiding of the “off” frames could be inaccurate. Therefore it is necessary to scale up the “off” frames to match with the “on” frames.

The flux calibration was done as follows. We calculated the flux density (flux per unit of wavelength) at 1.235  $\mu\text{m}$  (J-band) and 1.662  $\mu\text{m}$  (H-band) using  $F_{\lambda(iso)}$  obtained from table 2 of Cohen et al. (2003), and the magnitudes in J and H bands of the standard star obtained using the 2MASS catalog. At  $\lambda=1.235 \mu\text{m}$  the flux density correspond to  $F_{\lambda}= 2.745 \times 10^{-13} \text{ erg s}^{-1} \text{ cm}^{-2} \text{ \AA}^{-1}$ , and at  $\lambda=1.662 \mu\text{m}$  the flux density correspond to  $F_{\lambda}= 1.366 \times 10^{-13} \text{ erg s}^{-1} \text{ cm}^{-2} \text{ \AA}^{-1}$ . Additionally, we used a synthetic spectrum of a G2 V star obtained from the Kurucz models, which is scaled to make the theoretical spectrum of the HIP023984 star. Finally, the N63A spectra are calibrated by flux multiplying the spectra by the theoretical spectrum of the reference star and dividing by the observational spectrum of the star. However, G type stars have numerous intrinsic features (i.e. absorption due to the bad atmospheric transmission range), and therefore this procedure could inflate the intensities of emission lines if they fall in them. The flux calibrated spectra have a large amount of

noise in some regions, but fortunately the emission lines are not falling in these ranges. Consequently, the spectra are only used in the wavelength ranges: 1.04 to 1.115  $\mu\text{m}$  and 1.15 to 1.27  $\mu\text{m}$  in J-band, and 1.50 to 1.80  $\mu\text{m}$  in H-band.

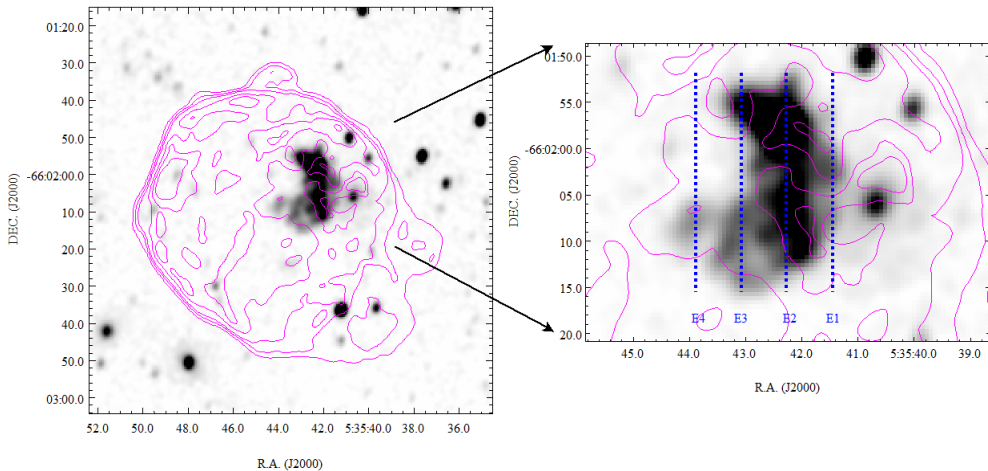


Figure 2.1: *Left: SIRIUS/IRS  $[\text{Fe II}]_{1.64\mu\text{m}}$  narrow-band image of N63A showing a two-lobed structure with a size of  $\sim 23''$  ( $\sim 5.3$  pc at the LMC distance of  $\sim 50$  kpc). Chandra X-ray contours are overlaid. Right:  $[\text{Fe II}]_{1.64\mu\text{m}}$  narrow-band image of the two-lobed structure of N63A using SIRIUS/IRSF. The dashed blue lines show the slit positions where the spectra were obtained. Chandra X-ray contours are overlaid.*

## 2.3 Results

### 2.3.1 Distribution of $[\text{Fe II}]$ and $[\text{P II}]$ emission in N63A

Figure 2.2 shows the NIR images of SNR N63A observed with the SIRIUS/IRSF in  $[\text{Fe II}]_{1.64\mu\text{m}}$ ,  $[\text{Fe II}]_{1.26\mu\text{m}}$  and  $[\text{P II}]_{1.19\mu\text{m}}$  narrow-bands. We detect a bright  $[\text{Fe II}]$  clump showing a two-lobed structure, which exhibit a similar distribution and location compared with the shock-heated structure seen in optical

wavelengths, as is shown in the color map composed of the HST images (see Figure 2.2). Also, the [Fe II] emission is closely associated with the brightest radio emission of N63A (Dickel et al., 1993). The size of the nebula is  $\sim 23'' \times 19''$  ( $\sim 5.3 \times 4.6$  pc at the LMC distance). The [Fe II] emission is just concentrated in this region, and we did not detect any other [Fe II] emission from other locations within or outside this SNR, as is seen in Figure 2.1

We notice that, in both [Fe II] images, the emission is more strong in the central part of the nebula, where the peak emission comes from the northeastern lobe of the nebula. The drop of the [Fe II] emission towards the west is coincident with the transition from the SNR (shock - heated) to the H II (photoionized) region identified as a third lobe in optical observations. Besides, the [P II] narrow-band image shows a more faint emission which comes from a similar region than the [Fe II] images. In addition, the [P II] emission is also detected toward the west, which is coincident with the third lobe of the optical nebula of N63A identified as photoionized region.

The line brightness detected in the [Fe II] $_{1.26\mu m}$  and [Fe II] $_{1.64\mu m}$  line maps correspond to  $(1.75 \pm 0.08) \times 10^{-4}$  erg s $^{-1}$  cm $^{-2}$  sr $^{-1}$  and  $(1.24 \pm 0.07) \times 10^{-4}$  erg s $^{-1}$  cm $^{-2}$  sr $^{-1}$ , respectively. These are measured in an area of  $\sim 19'' \times 8''$ , which is located in the bright part of the two-lobed nebula and centered at  $\alpha: 5^h 35^m 42.47^s$ ,  $\delta: -66^\circ 02' 04.86''$ . In the same region we detected a [P II] $_{1.19\mu m}$  line brightness of  $(2.07 \pm 0.09) \times 10^{-5}$  erg s $^{-1}$  cm $^{-2}$  sr $^{-1}$ , which is approximately 10 times weaker than the [Fe II] $_{1.26\mu m}$  line emission. Additionally, we obtained the [Fe II] $_{1.26\mu m}$ , [Fe II] $_{1.64\mu m}$  and [P II] $_{1.19\mu m}$  lines fluxes of  $(1.95 \pm 0.09) \times 10^{-12}$  erg s $^{-1}$  cm $^{-2}$ ,  $(1.38 \pm 0.08) \times 10^{-12}$  erg s $^{-1}$  cm $^{-2}$  and  $(2.3 \pm 0.1) \times 10^{-13}$  erg s $^{-1}$  cm $^{-2}$ , respectively.

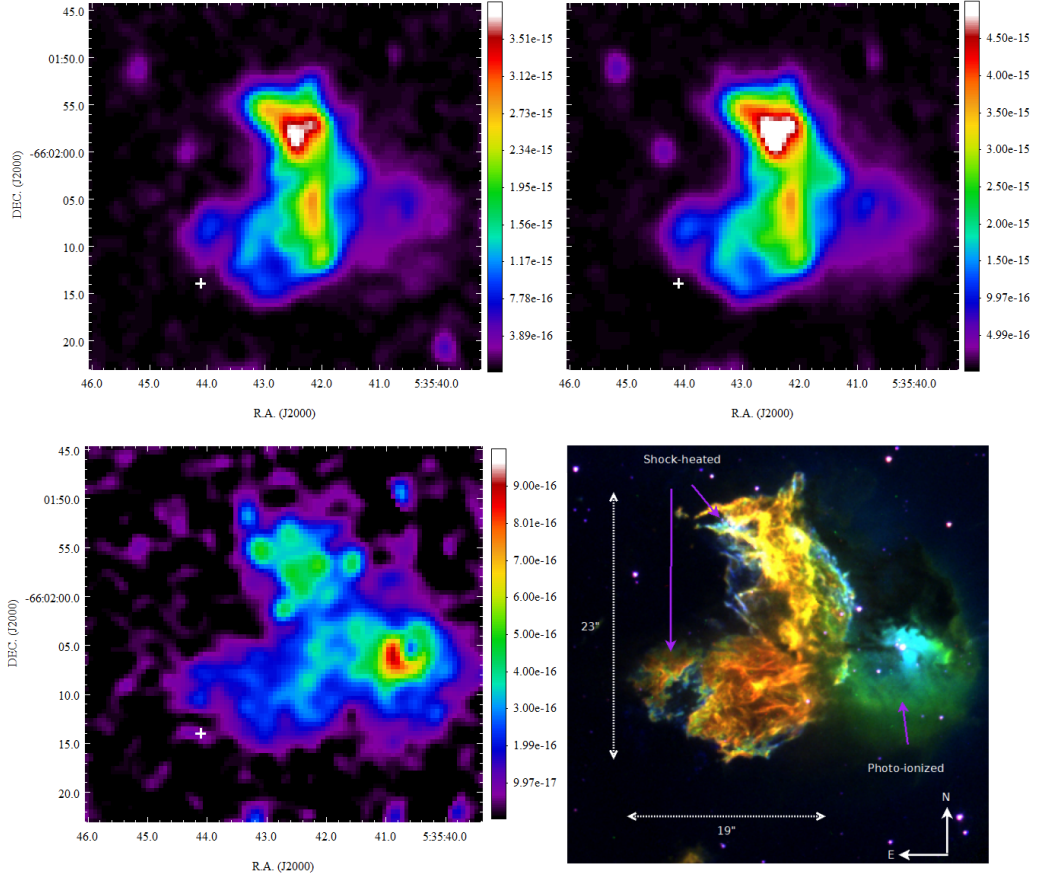


Figure 2.2: *Top-left:  $[Fe II]_{1.64\mu m}$  line map; top-right:  $[Fe II]_{1.26\mu m}$  line map; bottom-left:  $[P II]_{1.19\mu m}$  line map; bottom-right: Color map composed of HST images:  $[S II]$  (red),  $H\alpha$  (green) and  $[OIII]$  (blue; seen mostly in absorption in the shock-heated lobes). All the NIR narrow-band images were smoothed with a Gaussian kernel of 3 in sigma. The color levels are given in units of  $erg\ s^{-1}\ cm^{-2}\ pix^{-1}$ . Cross marks denote the center position of SNR N63A.*

### 2.3.2 NIR Extinction

The two major NIR forbidden iron emission lines,  $[Fe II]$  -  $1.26\ \mu m$  and  $[Fe II]$  -  $1.64\ \mu m$ , are due to electronic transitions from the same upper level, and

thus their intensity ratios do not depend on the physical conditions of the gas. Therefore, the observed  $[\text{Fe II}]_{1.26/1.64\mu\text{m}}$  intensity ratio can be used to derive the relative extinction between the two wavelengths of the J and H bands (since their central wavelengths are 1.25 and 1.65  $\mu\text{m}$ , respectively). The intrinsic line ratio is fixed at 1.36 (Nussbaumer & Storey 1988), which has an uncertainty of  $\sim 20\%$ .

We compare the observed ratio with the intrinsic ratio of 1.36 expected from the atomic parameters of  $[\text{Fe II}]$  and compute the extinction toward SNR N63A. Figure 2.3 shows the  $[\text{Fe II}]_{1.26/1.64\mu\text{m}}$  ratio map, where we obtain an  $[\text{Fe II}]$  ratio of  $1.4 \pm 0.1$  from the marked region (white contour). However, an internal region with a longitude  $\sim 12''$  exhibits a lower ratio,  $\sim 1.3$ . We derive the visual extinction using:  $A_V \approx 10 E_{J-H} = 10 (A_{1.26} - A_{1.64})$ , where  $E_{J-H} = 1.086 \ln\left(\frac{([\text{Fe II}]_{1.26/1.64\mu\text{m}})_{\text{int}}}{([\text{Fe II}]_{1.26/1.64\mu\text{m}})_{\text{obs}}}\right)$ . Thus, we obtained a visual extinction of  $A_V \sim 0$  to 0.5 mag (if we consider the uncertainty in the  $[\text{Fe II}]$  ratio), which is quite small, and also we estimated a differential extinction of  $E_{1.26-1.64} \leq 0.05$ . We adopted  $A_V = 0$  for  $[\text{Fe II}]_{1.26/1.64\mu\text{m}}$  values  $> 1.36$ .

The visual extinction derived in this research is lower compared with the values estimated in previous researches. Oliva, Moorwood & Danziger (1989) obtained an  $[\text{Fe II}]_{1.26/1.64\mu\text{m}}$  ratio of 1.26 for N63A, which is also very close to 1.36, the  $[\text{Fe II}]$  intrinsic line ratio given by Nussbaumer & Storey (1988). The derived visual extinction corresponds to 0.8 mag with a differential extinction of  $E_{1.26-1.64} \leq 0.1$ , assuming a total uncertainty of 10% on the observed and predicted values of the ratio. The visual extinction derived from optical data (e.g. Danziger and Leibowitz, 1985; Dennefeld, 1986; Levenson et al., 1995) is in a range between 0.7 and 1.0 mag.

We adopted the lower value obtained for the  $[\text{Fe II}]_{1.26/1.64\mu\text{m}}$  ratio: 1.3 (which implies  $A_V \sim 0.5$  mag), if we assume that the uncertainty in estimating

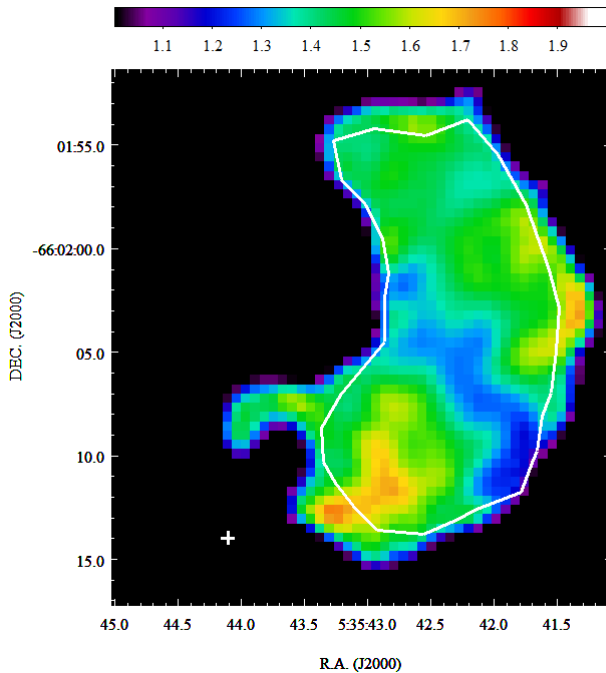


Figure 2.3: The image shows the  $[Fe II]_{1.26/1.64\mu m}$  ratio map. The image was smoothed with a Gaussian kernel of 3 in sigma. The cross denote the center position of SNR N63A. The white contour marks the region where the  $[Fe II]$  ratio is obtained.

this value is  $\sim 10\%$ . Thereafter, we determine the hydrogen column density using this ratio and the equation:

$$([Fe II]_{1.26/1.64\mu m})_{obs} = ([Fe II]_{1.26/1.64\mu m})_{int} e^{-(\sigma_{1.26,H} - \sigma_{1.64,H})N_H} \quad (1)$$

where:  $\sigma_{1.26,H} \sim 2.729 \times 10^{-23}$  ( $\text{cm}^2/\text{H}$ ) and  $\sigma_{1.64,H} \sim 1.901 \times 10^{-23}$  ( $\text{cm}^2/\text{H}$ ).

The extinction cross sections are obtained from the carbonaceous silicate model for the average LMC dust given by Weingartner & Draine (2001)<sup>1</sup>. Thus, the hydrogen nuclei column density is  $N_H \sim 5.45 \times 10^{21} \text{ cm}^{-2}$ .

<sup>1</sup><http://www.astro.princeton.edu/~draine/dust/dustmix.html>

The estimation of the extinction towards N63A (or the H nuclei column density towards N63A) is dominated by many uncertainties. For example, the exact values of the Einstein A-coefficients are somewhat controversial, where the numerical values of the Einstein A-coefficients for NIR [Fe II] lines differs  $\sim 50\%$  in the literature. Furthermore, the  $[\text{Fe II}]_{1.26/1.64\mu\text{m}}$  ratio has been derived empirically from 0.98 to 1.49, based on observations of nearby stellar objects (e.g. Rodriguez-Ardila et al., 2004; Smith & Hartigan, 2006; Giannini et al., 2015). Then, if we adopted the  $[\text{Fe II}]_{1.26/1.64\mu\text{m}}$  ratio of 1.49, the column density is even higher ( $\sim 1.65 \times 10^{22} \text{ cm}^{-2}$ ).

### 2.3.3 Relative Abundance and dust destruction

The life cycle of dust grains, the amount and relative abundances present in the ISM are determined by the balance between dust formation, grain modification, and dust destruction (Draine 2003). SNRs shock processing of interstellar dust plays an extremely important role in the ISM, where the dust destruction is known to occur in both fast and slow shocks (SNRs; Jones 2004).

Knowledge of the grain destruction plays an important role in understanding the dust abundance and the origin of the elemental depletion pattern in the local universe (Jones et al. 1996; Jones 2004; Tielens 1998; Dwek 1998). Many SNRs exhibit post-shock IR emission (Arendt 1989, Saken et al. 1992, Reach et al. 2006), but only a fraction of these have clear indication of interaction with specifically identifiable clouds in the surrounding ISM. Of these, SNR N63A in the LMC is an interesting case in which the cloud being swept up exhibits identifiable IR emission.

Fe is a well known refractory species whose gas phase abundance in the ISM is often found to be down by many orders of magnitudes relative its cosmic value. The only regions where Fe is not found to be significantly depleted are

those associated with fast ( $>100 \text{ km s}^{-1}$ ) shocks which can effectively destroy the dust grains by sputtering. The gas phase iron abundance,  $x(\text{Fe})$ , is a measure of the shock efficiency in disrupting the dust grains where iron is locked.

In addition, [P II] emission line can be used to study the shock destruction of dust grains and the origin of [Fe II] emission lines. In this regard, a powerful method to estimate the percentage of gas phase iron based on [Fe II]/[P II] line ratios has been proposed by Oliva et al. (2001). Besides Fe, P is the only abundant element whose first ionized stage has forbidden lines in the NIR range. Phosphorus is also a non-refractory species whose measured depletion in ionized gas is close to unity. The [P II] and [Fe II] lines have many interesting similarities, such as: similar excitation temperatures, critical densities, radiative recombination coefficients, and their parent ions have comparable ionization potentials (10.49 and 7.90 eV, respectively). In particular, [P II] $_{1.19\mu\text{m}}$  line originates from a level whose excitation energy is almost identical to that of [Fe II] $_{1.26\mu\text{m}}$  line, and therefore from almost the same region in shocked gas.

Consequently, the [P II] $_{1.19\mu\text{m}}$ /[Fe II] $_{1.26\mu\text{m}}$  line ratio is a good indicator of the relative abundance of the two species, which can be used to study the shock processing of dust in the ISM, because P is not depleted while Fe is mostly locked in dust grains, giving a direct estimate of the presence of robust dust in a given region. In the general ISM this ratio is high, while in fast shocks, due to the dust grains are destroyed, the gas phase Fe abundance increases and therefore the ratio decreases. These properties have been used for the study of dust processing in HH objects and the origin of [Fe II] emission in external galaxies (e.g. Garcia Lopez et al., 2010; Oliva et al., 2001).

The relation between [Fe II]/[P II] line intensity ratio and the Fe/P abundance ratio is given by Oliva et al. (2001) as follows:

$$x(\text{Fe})/x(\text{P}) \leq 2 \cdot I([\text{Fe II}]_{1.26\mu\text{m}})/I([\text{P II}]_{1.19\mu\text{m}}) \quad (2)$$

which is obtained from the relation between [Fe II] and [P II] line intensities, and  $\text{Fe}^+/\text{P}^+$  abundance ratio as:

$$x(\text{Fe}^+)/x(\text{P}^+) \simeq 2 \cdot I([\text{Fe II}]_{1.26\mu\text{m}})/I([\text{P II}]_{1.19\mu\text{m}}) \quad (3)$$

where, the relation between the  $\text{Fe}^+/\text{P}^+$  abundance ratio and the Fe/P abundance ratio is as follows:

$$x(\text{Fe}^+)/x(\text{P}^+) \geq x(\text{Fe})/x(\text{P}) \quad (4)$$

The equation (2) is accurate to within a factor of 2 for all temperatures and densities expected within the shock.

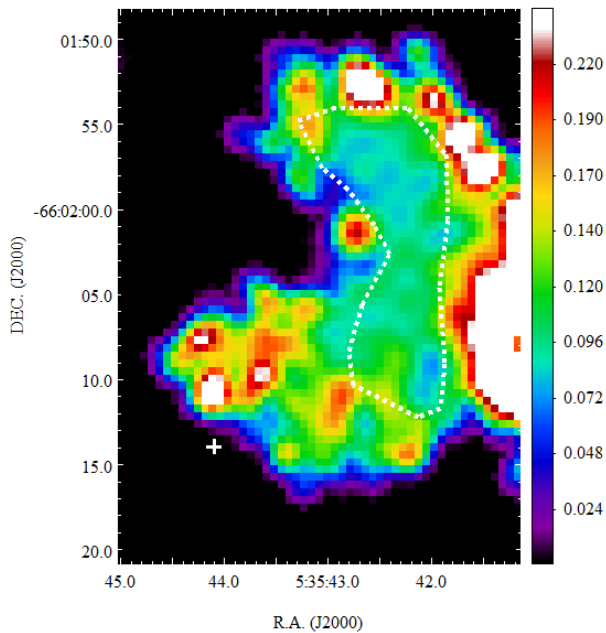


Figure 2.4: The image shows the  $[\text{P II}]_{1.19\mu\text{m}}/[\text{Fe II}]_{1.26\mu\text{m}}$  ratio map. The image was smoothed with a Gaussian kernel of 3 in sigma. The cross denote the center position of SNR N63A. The  $[\text{P II}]/[\text{Fe II}]$  ratio is obtained from the dotted region.

Figure 2.4 shows the  $[\text{P II}]_{1.19\mu\text{m}}/[\text{Fe II}]_{1.26\mu\text{m}}$  intensity ratio map for N63A. The  $[\text{P II}]/[\text{Fe II}]$  ratio obtained from the dotted region correspond to  $0.10 \pm 0.01$ ,

and the relative abundance inferred using this ratio correspond to  $x(\text{Fe})/x(\text{P}) \simeq x(\text{Fe}^+)/x(\text{P}^+) \simeq 20 \pm 2$ , or at inverse  $x(\text{P})/x(\text{Fe}) \simeq 0.05 \pm 0.005$ , which is 6 times higher than the cosmic abundance  $x(\text{P}/\text{Fe})_{\odot} = 8.1 \times 10^{-3}$ .

We also measured the  $[\text{P II}]/[\text{Fe II}]$  intensity ratio from slit positions located in the central part of the two-lobed structure (see section 2.3.4) using spectroscopic observations obtained with IRIS2/AAT. The line ratio is even lower, with an average value  $\sim 0.043$ , which infers a relative abundance of  $x(\text{Fe})/x(\text{P}) \simeq 47$  or  $x(\text{P})/x(\text{Fe}) \simeq 0.021$ , which is  $\sim 3$  times higher than the cosmic abundance.

The values obtained for SNR N63A indicate that the emitting gas has recently passed through a fast shock, which sputtered and destroyed large percentage of the dust grains.

### 2.3.4 NIR [Fe II] lines and electron density

Figures 2.5 and 2.6 show the spectra of N63A obtained from spectroscopic observations in 4 different positions (see Figure 2.1) using IRIS2/AAT in J-band and H-band, respectively. Also, OH lines are indicated in the bottom of each spectrum. The emission lines produced by the OH radical dominate the IR spectra. The removal of these lines from the spectra is an essential part of the processing of the NIR spectral data. As the flux within these lines is several order of magnitude above the sky emission from other sources, they are the dominant source of noise in the fully processed data. As we can see in Figure 2.6, the effect of the OH lines slightly decreases the accuracy of the measurements of some weak lines.

The NIR lines detected in N63A are summarized in Tables 2.2 and 2.3. The integrated fluxes are obtained by fitting gaussians over the emission lines, and the uncertainties are calculated from statistical errors. The intensity of all the emission lines is brighter in the central part of the nebula, corresponding to the

E2 and E3 slit positions (see Figure 2.1).

Table 2.2: *Emission lines identified in J-band.*

J-band							
Slit	Line ID <sup>a</sup>	$\lambda_{lab}$	RMS <sup>b</sup>	Peak <sup>c</sup>	FWHM	$\lambda_{obs}$	Flux <sup>d</sup>
		( $\mu\text{m}$ )			( $10^{-4} \mu\text{m}$ )	( $\mu\text{m}$ )	
E1	He I $^3\text{P}-^3\text{S}_1$	1.083	5.20	34.0	3.34	1.084	$285.06 \pm 0.05$
	H I 6-3 (Pa $\gamma$ )	1.094	5.22	5.49	2.67	1.095	$36.7 \pm 0.3$
	[Fe II] $\text{a}^4\text{D}_{7/2}-\text{a}^6\text{D}_{9/2}$	1.257	13.2	15.5	3.27	1.258	$127.7 \pm 0.8$
E2	He I $^3\text{P}-^3\text{S}_1$	1.083	11.9	93.1	2.84	1.084	$664.16 \pm 0.09$
	H I 6-3 (Pa $\gamma$ )	1.094	5.78	8.43	2.82	1.095	$59.6 \pm 0.2$
	[P II] $^1\text{D}_2-^3\text{P}_2$	1.189	3.94	2.68	3.19	1.190	$21.4 \pm 0.4$
	[Fe II] $\text{a}^4\text{D}_{7/2}-\text{a}^6\text{D}_{9/2}$	1.257	15.3	64.7	2.99	1.258	$486.1 \pm 0.2$
E3	He I $^3\text{P}-^3\text{S}_1$	1.083	10.2	70.1	3.09	1.084	$543.99 \pm 0.09$
	H I 6-3 (Pa $\gamma$ )	1.094	4.62	4.35	2.73	1.095	$29.9 \pm 0.3$
	[P II] $^1\text{D}_2-^3\text{P}_2$	1.189	3.60	1.46	2.42	1.190	$8.8 \pm 0.6$
	[Fe II] $\text{a}^4\text{D}_{7/2}-\text{a}^6\text{D}_{9/2}$	1.257	9.69	26.6	3.34	1.258	$223.7 \pm 0.2$
E4	He I $^3\text{P}-^3\text{S}_1$	1.083	4.35	17.3	3.06	1.084	$133.62 \pm 0.07$
	H I 6-3 (Pa $\gamma$ )	1.094	3.73	0.96	3.12	1.095	$7.5 \pm 0.9$
	[Fe II] $\text{a}^4\text{D}_{7/2}-\text{a}^6\text{D}_{9/2}$	1.257	6.75	3.13	4.27	1.258	$33.5 \pm 0.9$

(<sup>a</sup>) Ionic transitions are given as upper-lower.

(<sup>b</sup>) RMS given in units of  $10^{-13} \text{ erg cm}^{-2} \text{ s}^{-1}$ .

(<sup>c</sup>) Peak emission given in units of  $10^{-11} \text{ erg cm}^{-2} \text{ s}^{-1}$ .

(<sup>d</sup>) Integrated flux of the observed lines given in units of  $10^{-15} \text{ erg cm}^{-2} \text{ s}^{-1}$ .

Table 2.3: *Emission lines identified in H-band.*

H-band							
Slit	Line ID <sup>a</sup>	$\lambda_{lab}$	RMS <sup>b</sup>	Peak <sup>c</sup>	FWHM	$\lambda_{obs}$	Flux <sup>d</sup>
		( $\mu\text{m}$ )			( $10^{-4} \mu\text{m}$ )	( $\mu\text{m}$ )	
E1	[Fe II] a <sup>4</sup> D <sub>7/2</sub> -a <sup>4</sup> F <sub>9/2</sub>	1.644	2.491	5.062	4.523	1.645	57.3 ± 0.1
	[Fe II] a <sup>4</sup> D <sub>5/2</sub> -a <sup>4</sup> F <sub>9/2</sub>	1.534	3.728	0.607	4.903	1.535	7 ± 2
	[Fe II] a <sup>4</sup> D <sub>5/2</sub> -a <sup>4</sup> F <sub>7/2</sub>	1.677	2.724	0.430	4.459	1.679	4 ± 2
	(1)		2.646	0.291	4.062	1.575	3 ± 2
E2	[Fe II] a <sup>4</sup> D <sub>7/2</sub> -a <sup>4</sup> F <sub>9/2</sub>	1.644	4.201	48.92	4.121	1.645	505.35 ± 0.03
	[Fe II] a <sup>4</sup> D <sub>5/2</sub> -a <sup>4</sup> F <sub>9/2</sub>	1.534	3.186	5.734	4.297	1.535	61.7 ± 0.2
	[Fe II] a <sup>4</sup> D <sub>3/2</sub> -a <sup>4</sup> F <sub>7/2</sub>	1.599	2.676	3.671	3.859	1.601	35.5 ± 0.2
	[Fe II] a <sup>4</sup> D <sub>1/2</sub> -a <sup>4</sup> F <sub>5/2</sub>	1.664	3.069	2.171	3.783	1.666	20.5 ± 0.4
	[Fe II] a <sup>4</sup> D <sub>5/2</sub> -a <sup>4</sup> F <sub>7/2</sub>	1.677	3.047	3.967	4.202	1.679	41.7 ± 0.2
(2) <sup>e</sup>		2.970	1.078	3.861	1.713	10.4 ± 0.8	
E3	[Fe II] a <sup>4</sup> D <sub>7/2</sub> -a <sup>4</sup> F <sub>9/2</sub>	1.644	4.643	26.98	4.202	1.645	284.14 ± 0.08
	[Fe II] a <sup>4</sup> D <sub>5/2</sub> -a <sup>4</sup> F <sub>9/2</sub>	1.534	2.888	3.150	4.708	1.535	37.1 ± 0.2
	[Fe II] a <sup>4</sup> D <sub>3/2</sub> -a <sup>4</sup> F <sub>7/2</sub>	1.599	5.714	1.950	3.651	1.601	17 ± 2
	[Fe II] a <sup>4</sup> D <sub>1/2</sub> -a <sup>4</sup> F <sub>5/2</sub>	1.664	3.053	1.052	4.255	1.666	11.2 ± 0.9
	[Fe II] a <sup>4</sup> D <sub>5/2</sub> -a <sup>4</sup> F <sub>7/2</sub>	1.677	3.006	2.295	4.224	1.679	24.2 ± 0.4
(3) <sup>f</sup>		3.530	0.584	3.487	1.747	5 ± 2	
E4	[Fe II] a <sup>4</sup> D <sub>7/2</sub> -a <sup>4</sup> F <sub>9/2</sub>	1.644	1.613	3.492	4.592	1.645	40.19 ± 0.07
	[Fe II] a <sup>4</sup> D <sub>5/2</sub> -a <sup>4</sup> F <sub>9/2</sub>	1.534	2.774	0.496	5.773	1.535	7 ± 1
	[Fe II] a <sup>4</sup> D <sub>3/2</sub> -a <sup>4</sup> F <sub>7/2</sub>	1.599	2.016	0.271	5.666	1.601	3 ± 1
	[Fe II] a <sup>4</sup> D <sub>5/2</sub> -a <sup>4</sup> F <sub>7/2</sub>	1.677	2.145	0.513	3.327	1.679	4.2 ± 0.8

(<sup>a</sup>) Ionic transitions are given as upper-lower.

(<sup>b</sup>) RMS given in units of  $10^{-13} \text{ erg cm}^{-2} \text{ s}^{-1}$ .

(<sup>c</sup>) Peak emission given in units of  $10^{-11} \text{ erg cm}^{-2} \text{ s}^{-1}$ .

(<sup>d</sup>) Integrated flux of the observed lines given in units of  $10^{-15} \text{ erg cm}^{-2} \text{ s}^{-1}$ .

(<sup>e</sup>) This line is probably [Fe II] a<sup>4</sup>D<sub>3/2</sub>-a<sup>4</sup>F<sub>5/2</sub> - 1.712  $\mu\text{m}$  which is detected only in the E2 slit position.

(<sup>f</sup>) This line is probably [Fe II] a<sup>4</sup>D<sub>1/2</sub>-a<sup>4</sup>F<sub>3/2</sub> - 1.745  $\mu\text{m}$  which is detected only in the E3 slit position.

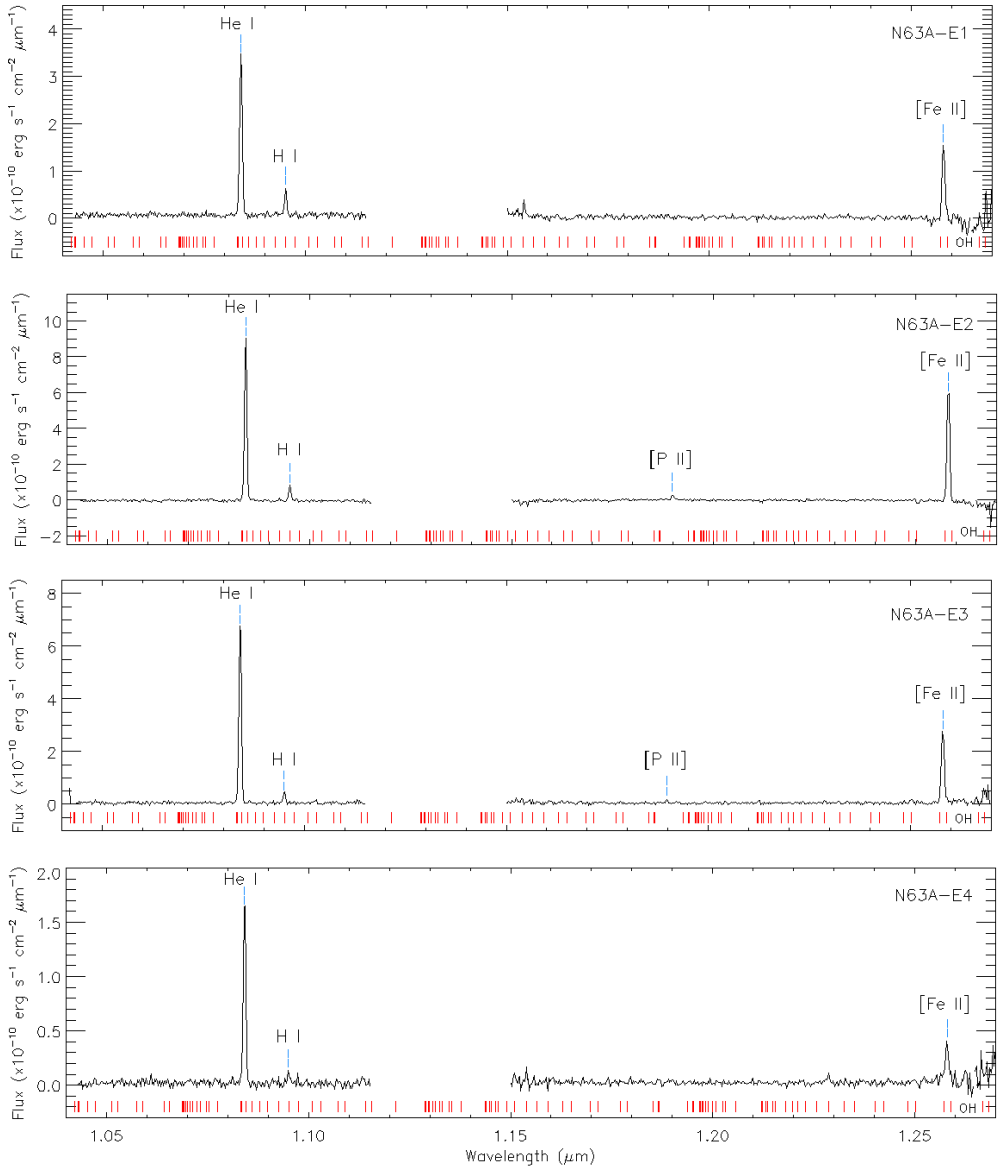


Figure 2.5: The image shows the 1-D spectra of N63A calibrated by flux, obtained in J-band using IRIS2/AAT in the slit positions shown in Figure 2.1. The emission lines correspond to He I, [Fe II], and relatively weak emission of H I and [P II]. Also, OH lines are shown in the bottom of each spectrum.

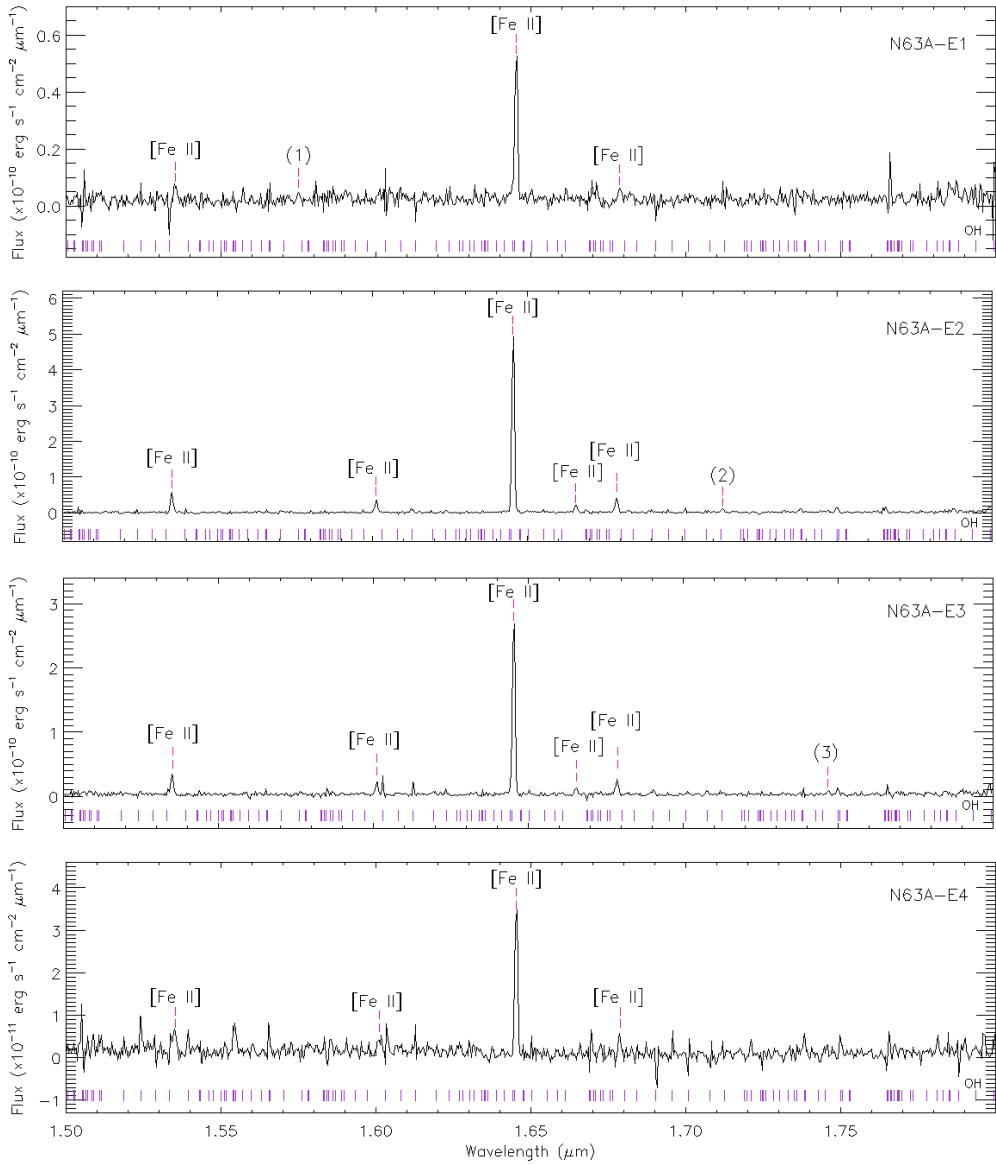


Figure 2.6: The image shows the 1-D spectra of N63A calibrated by flux, obtained in H-band using IRIS2/AAT in the slit positions shown in Figure 2.1. All the lines correspond to [Fe II] emission lines. Additionally, OH lines are shown in the bottom of each spectrum.

Most of the emission lines detected in N63A correspond to [Fe II] lines, which are important tools for radiative atomic shocks. The strong emission of [Fe II] - 1.257  $\mu\text{m}$  and [Fe II] - 1.644  $\mu\text{m}$  is typical of shock-heated gas. Besides, the spectra also show very high emission of He I - 1.083  $\mu\text{m}$  line (where its intensity is even higher than the stronger [Fe II] lines), whereas exhibit relatively faint emission of HI  $Pa\gamma$  - 1.094  $\mu\text{m}$  and [P II] - 1.189  $\mu\text{m}$  lines. In addition, there are some lines (e.g. [Fe II]- 1.664  $\mu\text{m}$ , [P II]- 1.189  $\mu\text{m}$ ) which are only detected in the central positions where the intensity of the emission lines is brighter, as aforementioned.

Furthermore, due to the uncertainty in the flux calibration of the spectra, we used the [Fe II] 1.26  $\mu\text{m}$  and [Fe II] 1.64  $\mu\text{m}$  narrow-band images to correct the flux measured in the spectral lines (Tables 2.2 and 2.3). Also, these line fluxes are de-reddened using the extinction obtained in section 2.3.2. The line fluxes re-calibrated and de-reddened are given in Tables 2.4 and 2.5.

To estimate the relative flux of the observed lines, these are normalized by the [Fe II]- 1.644  $\mu\text{m}$  for the lines obtained in the H-band, and by the [Fe II]- 1.257  $\mu\text{m}$  for the lines obtained in J-band. The line ratios are listed in Table 2.6, which correspond to the de-reddened ratios using the extinction estimated in section 2.3.2. The ratios estimated in this research are in agreement with the values measured in previous research (see last column of Table 2.6).

The line ratios corresponding to He I-1.083  $\mu\text{m}$ /[Fe II]-1.257  $\mu\text{m}$  and H I-1.094  $\mu\text{m}$ /[Fe II]-1.257  $\mu\text{m}$  exhibit different values for each spatial position. When the emission comes from thin filaments, one might expect to observe different fluxes depending on the orientation of the filaments. On the other hand, this effect disappears if the filaments are randomly oriented inside the remnant. Besides, the strong He I emission seems to be the result of the the swept-up material due to the SNR evolution.

Table 2.4: *De-reddened lines and flux correction for spectral lines in J-band.*

J-band					
Slit	Line ID	Flux <sup>a</sup>	De-reddened <sup>b</sup>	Flux <sup>c</sup>	De-reddened <sup>d</sup>
	( $\mu\text{m}$ )	( $10^{-15}$ erg cm <sup>-2</sup> s <sup>-1</sup> )		( $10^{-15}$ erg cm <sup>-2</sup> s <sup>-1</sup> )	
E1	He I - 1.083	285.06±0.05	343.9±0.1	131.12±0.02	158.21±0.02
	H I - 1.094	36.7±0.3	44.1±0.4	16.8±0.1	20.2±0.1
	[Fe II] - 1.257	127.7±0.8	148.1±0.9	58.7±0.4	68.1±0.5
E2	He I - 1.083	664.16±0.09	801.4±0.1	416.42±0.06	502.4±0.1
	H I - 1.094	59.6±0.2	71.7±0.2	37.3±0.1	44.8±0.1
	[P II] - 1.189	21.4±0.4	25.1±0.5	13.4±0.3	15.7±0.4
	[Fe II] - 1.257	486.1±0.2	564.0±0.2	304.7±0.1	353.5±0.1
E3	He I - 1.083	543.99±0.09	656.4±0.1	367.1±0.1	443.0±0.1
	H I - 1.094	29.9±0.3	35.9±0.4	20.1±0.2	24.1±0.2
	[P II] - 1.189	8.8±0.6	10.3±0.7	5.9±0.4	6.9±0.5
	[Fe II] - 1.257	223.7±0.2	259.6±0.2	150.9±0.1	175.1±0.1
E4	He I - 1.083	133.62±0.07	161.2±0.1	58.79±0.03	70.94±0.04
	H I - 1.094	7.5±0.9	9±1	3.3±0.4	4.0±0.5
	[Fe II] - 1.257	33.5±0.9	39±1	14.7±0.4	17.0±0.5

<sup>(a)</sup> Integrated flux of the observed lines.

<sup>(b)</sup> The flux was de-reddened using the extinction estimated in section 2.3.2.

<sup>(c)</sup> The flux was corrected using the [Fe II]<sub>1.26 $\mu\text{m}$</sub>  narrow-band image.

<sup>(d)</sup> The corrected flux was de-reddened using the extinction estimated in section 2.3.2.

Table 2.5: De-reddened lines and flux correction for spectral lines in H-band.

H-band					
Slit	Line ID	Flux <sup>a</sup>	De-reddened <sup>b</sup>	Flux <sup>c</sup>	De-reddened <sup>d</sup>
	( $\mu\text{m}$ )	( $10^{-15}$ erg cm <sup>-2</sup> s <sup>-1</sup> )		( $10^{-15}$ erg cm <sup>-2</sup> s <sup>-1</sup> )	
E1	[Fe II] - 1.644	57.3±0.1	63.5±0.1	37.8±0.1	41.9±0.1
	[Fe II] - 1.534	7±2	7±2	5±1	5±1
	[Fe II] - 1.677	4±2	4±2	3±1	3±1
	(1)	3±2	3±2	2±1	2±1
E2	[Fe II] - 1.644	505.35±0.03	560.50±0.03	219.82±0.01	243.81±0.01
	[Fe II] - 1.534	61.7±0.2	69.0±0.2	26.8±0.1	30.0±0.1
	[Fe II] - 1.599	35.5±0.2	39.5±0.2	15.4±0.1	17.2±0.1
	[Fe II] - 1.664	20.5±0.4	22.6±0.4	8.9±0.9	9.8±0.9
	[Fe II] - 1.677	41.7±0.2	46.1±0.2	18.1±0.1	20.0±0.1
	(2) <sup>e</sup>	10.4±0.8	11.4±0.9	4.5±0.3	4.9±0.3
E3	[Fe II] - 1.644	284.14±0.08	315.1±0.1	102.29±0.03	113.45±0.03
	[Fe II] - 1.534	37.1±0.2	41.5±0.2	13.3±0.7	14.9±0.8
	[Fe II] - 1.599	17±2	18±2	6.1±0.7	6.7±0.8
	[Fe II] - 1.664	11.2±0.9	12±1	4.0±0.3	4.4±0.3
	[Fe II] - 1.677	24.2±0.4	26.7±0.4	8.7±0.1	9.6±0.1
	(3) <sup>f</sup>	5±2	5±2	1.8±0.7	1.9±0.8
E4	[Fe II] - 1.644	40.19±0.07	44.57±0.08	10.44±0.03	11.57±0.03
	[Fe II] - 1.534	7±1	7±1	1.8±0.3	2.0±0.3
	[Fe II] - 1.599	3±1	3±1	0.7±0.3	0.7±0.3
	[Fe II] - 1.677	4.2±0.8	4.6±0.9	1.0±0.2	1.1±0.2

(<sup>a</sup>) Integrated flux of the observed lines.

(<sup>b</sup>) The flux was de-reddened using the extinction estimated in section 2.3.2.

(<sup>c</sup>) The flux was corrected using the [Fe II]<sub>1.64 $\mu\text{m}$</sub>  narrow-band image.

(<sup>d</sup>) The corrected flux was de-reddened using the extinction estimated in section 2.3.2.

(<sup>e</sup>) This line is probably [Fe II] - 1.712  $\mu\text{m}$ , which is detected only in the E2 slit position.

(<sup>f</sup>) This line is probably [Fe II] - 1.745  $\mu\text{m}$ , which is detected only in the E3 slit position.

Furthermore, we know that  $\text{Fe}^+$  has 63 “ground states” divided into 24 even terms, all lying at energies  $E/K < 55000$  K (cf. Johansson, 1978). The [Fe II] lines identified in the NIR spectra are divided into four groups of lines sharing the same upper level,  $a^4D$ . The lowest level of this quartet,  $a^4D_{7/2}$  is populated by electron collisions from the ground state,  $a^4D_{9/2}$ , whilst the other 3 levels are less favoured by collisions. At low densities ( $n_e < 10^3$ ) one expects that the lines arising from  $a^4D_{7/2}$  (e.g. 1.644 and 1.257  $\mu\text{m}$ ) are more than 10 times brighter than the lines from the other 3 levels of the quartet.

There are many [Fe II] lines with comparable excitation energies that can be used as density diagnosis. The flux ratios of these lines are mainly a function of electron density ( $n_e$ ) of the emitting region, depending only weakly on temperature ( $T_e$ ). At low densities ( $n_e \ll n_{cr}$ ), their ratios are equal to the ratio of their statistical weights, while at high densities ( $n_e \gg n_{cr}$ ), their ratios are given by statistical weights times the ratio of Einstein coefficients. Koo et al. (2016) gives a linear approximations for the electron density as function of the line flux ratios of the different [Fe II] lines, as follows:

$$n_e = 10^{2.93+5.95r_{1.534/1.644}}, \text{ for } 0.10 \leq r_{1.534/1.644} \leq 0.32 \quad (5)$$

$$n_e = 10^{3.16+7.01r_{1.600/1.644}}, \text{ for } 0.06 \leq r_{1.600/1.644} \leq 0.24 \quad (6)$$

$$n_e = 10^{3.14+13.7r_{1.664/1.644}}, \text{ for } 0.03 \leq r_{1.664/1.644} \leq 0.13 \quad (7)$$

$$n_e = 10^{2.93+8.14r_{1.667/1.644}}, \text{ for } 0.07 \leq r_{1.667/1.644} \leq 0.23 \quad (8)$$

The maximum error of the above fits in electron density is less than 15%. We calculated the upper limit of electron density in the emitting region of N63A, which are listed in Table 2.7, using the approximations given by Koo (2016) and the [Fe II] line ratios (see Table 2.6). Thus, we estimated a post-shock electron density in the range  $3.1 \times 10^3 \text{ cm}^{-3} \leq n_e \leq 8.7 \times 10^3 \text{ cm}^{-3}$ . We adopted an average electron density of  $\sim (4.7 \pm 0.7) \times 10^3 \text{ cm}^{-3}$ . This value should be much higher than the uncompressed pre-shock density for a radiative shock.

Table 2.6: *NIR line ratios obtained in N63A.*

H-band						
Line	$\lambda$ ( $\mu\text{m}$ )	Flux( $\lambda$ )/Flux(1.644) <sup>a</sup>				
		E1	E2	E3	E4	Ref
[Fe II]	1.644	1	1	1	1	1
[Fe II]	1.534	0.12±0.04	0.1232±0.0004	0.131±0.001	0.17±0.03	0.13±0.03 <sup>b</sup>
[Fe II]	1.599		0.0704±0.0004	0.06±0.01	0.07±0.03	0.09±0.02 <sup>c</sup>
[Fe II]	1.664		0.040±0.001	0.039±0.003		
[Fe II]	1.677	0.07±0.03	0.0822±0.0004	0.085±0.001	0.10±0.02	
[Fe II] <sup>d</sup>	1.712		0.020±0.002			
[Fe II] <sup>e</sup>	1.745			0.017±0.007		
J-band						
Line	$\lambda$ ( $\mu\text{m}$ )	Flux( $\lambda$ )/Flux(1.257) <sup>f</sup>				
		E1	E2	E3	E4	Ref
He I	1.083	2.32±0.01	1.421±0.001	2.528±0.002	4.1±0.1	
H I	1.094	0.298±0.003	0.128±0.001	0.139±0.001	0.23±0.03	
[P II]	1.188		0.045±0.001	0.040±0.003		<0.06 <sup>g</sup>
[Fe II]	1.257	1	1	1	1	1

(<sup>a</sup>) Flux normalized by [Fe II] 1.644  $\mu\text{m}$  line.

(<sup>b</sup>) Reference from Koo, Raymond & Kim (2016).

(<sup>c</sup>) Reference from Oliva, Moorwood & Danziger (1989).

(<sup>d</sup>) This line appears as (2) in Figure 2.3, which is detected only in the E2 slit position.

(<sup>e</sup>) This line appears as (3) in Figure 2.3 and is detected only in the E3 slit position.

(<sup>f</sup>) Flux normalized by [Fe II] 1.257  $\mu\text{m}$  line.

(<sup>g</sup>) Reference from Oliva et al. (2001).

Table 2.7: *Electron densities.*

Line ratio	$n_e$ (cm <sup>-3</sup> )				
	E1	E2	E3	E4	Mean
[Fe II] <sub>1.534/1.644</sub>	4406±720	4603±8	5122±21	8740±1071	~ 5.7 x 10 <sup>3</sup>
[Fe II] <sub>1.599/1.644</sub>		4503±8	3807±162	4474±570	~ 4.2 x 10 <sup>3</sup>
[Fe II] <sub>1.664/1.644</sub>		4875±24	4724±70		~ 4.8 x 10 <sup>3</sup>
[Fe II] <sub>1.677/1.644</sub>	3161±417	3973±7	4187±18	5546±488	~ 4.2 x 10 <sup>3</sup>

Oliva et al. (1989) derived a post-shock electron density for N63A using the [Fe II]<sub>1.60/1.64</sub> ratio, which is determined in the range  $4.6 \times 10^3 \text{ cm}^{-3} \leq n_e \leq 1.09 \times 10^4 \text{ cm}^{-3}$ . These values are in agreement with our estimation.

Moreover, Oliva et al. (1989) derived an electron density for N63A based on the [S II]<sub>0.6716/0.6731</sub> ratio, which is estimated in the range  $1.4 \times 10^3 \text{ cm}^{-3} \leq n_e \leq 2.6 \times 10^3 \text{ cm}^{-3}$ . Levenson et al. (1995) also used this ratio to infer an electron density between  $0.9 \times 10^3$  and  $1.4 \times 10^3 \text{ cm}^{-3}$  for N63A. These electron densities obtained using optical lines are smaller than our estimation. In fact, we know that the [Fe II] line ratios can probe much higher densities,  $n_e = 10^3$  to  $10^5 \text{ cm}^{-3}$ , compared with the densities obtained using optical lines, because the [Fe II] lines have much larger critical density compared with the optical transitions of [S II]. Additionally, in a region where various components of gas at different densities contribute to the emission of both, [S II] and [Fe II] lines, we can expect to measure different values of the electron densities using the line ratios mentioned above.

## 2.4 Discussion

### 2.4.1 Extinction

In section 2.3.2 using an [Fe II] ratio map, we estimated a visual extinction of  $A_V \sim 0.5$  mag towards N63A, which implies an hydrogen column density of  $N_H \sim 5.45 \times 10^{21} \text{ cm}^{-2}$ .

From extinction maps of the LMC, the extinction to the column density ratio was estimated as  $A_V/N_H \sim 1.5 - 1.74 \times 10^{-22} \text{ mag/cm}^{-2}$  (e.g. Imara & Blitz, 2007; Dobashi et al., 2008), where this values are corrected by the average Milky Way extinction across the LMC. Using these relations and the visual extinction measured towards N63A, we obtained an hydrogen column density range of  $N_H \sim 2.9 - 3.3 \times 10^{21} \text{ cm}^{-2}$ , which is smaller than our previous estimation. Staveley-Smith et al. (2003) found a mean galactic reddening of  $\langle E(B-V) \rangle \sim 0.06$  mag over the LMC disk. If we applied this correction to the visual extinction measured from the [Fe II] ratio map, we obtained an hydrogen column density of  $N_H \sim 3.6 \times 10^{21} \text{ cm}^{-2}$ , which approaches to the column density estimated using the extinction to the column density ratio for the LMC.

### 2.4.2 De-reddened NIR emission

The location of the [Fe II] emission suggests that it is almost certainly from shocked gas. The shock must be radiative and the [Fe II] emission should originate from the cooling layer behind the shock. Using the extinction derived in section 2.3.2, we estimated the de-reddened [Fe II] $_{1.26\mu m}$ , [Fe II] $_{1.64\mu m}$  and [P II] $_{1.19\mu m}$  surface brightness of  $(2.03 \pm 0.09) \times 10^{-4} \text{ erg s}^{-1} \text{ cm}^{-2} \text{ sr}^{-1}$ ,  $(1.37 \pm 0.07) \times 10^{-4} \text{ erg s}^{-1} \text{ cm}^{-2} \text{ sr}^{-1}$  and  $(2.4 \pm 0.1) \times 10^{-5} \text{ erg s}^{-1} \text{ cm}^{-2} \text{ sr}^{-1}$ , respectively.

Also, we obtained the total dereddened [Fe II] $_{1.26\mu m}$ , [Fe II] $_{1.64\mu m}$  and [P

II] $_{1.19\mu m}$  fluxes, which are:  $(2.2 \pm 0.1) \times 10^{-12} \text{ erg s}^{-1} \text{ cm}^{-2}$ ,  $(1.37 \pm 0.07) \times 10^{-12} \text{ erg s}^{-1} \text{ cm}^{-2}$  and  $(2.7 \pm 0.1) \times 10^{-13} \text{ erg s}^{-1} \text{ cm}^{-2}$ , respectively.

### 2.4.3 Shock Parameters

In the SNR N63A, the [Fe II] emission is surrounded by hot X-ray emitting gas, with a density of  $4.35 \text{ cm}^{-3}$ , which is obtained dividing its ionization timescale by the age of the SNR. The ionization timescale is given by Warren et al. (2003) as  $\log(n_e t) = 11.66 \pm 0.16 \text{ (cm}^{-3} \text{ s)}$ , and the age of N63A is given by Hughes et al. (1998) in the range 2000-5000 yr, where we adopted a mean age of 3500 yr. Moreover, the temperature of the X-ray emitting gas corresponds to  $T_e = 0.78 \text{ keV} \sim 9.05 \times 10^6 \text{ K}$ , which is estimated from Chandra X-ray observations (Warren et al., 2003). Therefore, its pressure becomes:  $p/k_B \sim 8 \times 10^7 \text{ cm}^{-3} \text{ K}$ , where  $k_B$  is the Boltzmann constant. Furthermore, the electron temperature derived from the X-ray emitting gas corresponds to a shock speed  $v_s = (16 k_B T_e / 3 \mu)^{1/2} \sim 810 \text{ km s}^{-1}$  (where  $\mu = 1.4 m_H / 2.3 = 0.61 m_H$  is the mean mass per particle and  $m_H$  is the mass of H nuclei), which is a fairly large speed. We assume that this SNR is in its adiabatic phase. Then, using the Sedov solution, the SN explosion energy corresponds to  $E_{SN} = 2.1 \times 10^{51} n_0 (R/10 \text{ pc})^3 (v_s/10^3 \text{ km s}^{-1})^2 = 3.07 \times 10^{51} \text{ ergs}$ , where  $n_0 (= n_e/1.2) = 3.63 \text{ cm}^{-3}$  is the number density of hydrogen nuclei of the medium, and the radius  $R$  of the SNR N63A is  $35''$  (or  $8.5 \text{ pc}$  at LMC distance of  $50 \text{ kpc}$ ).

Also, we estimate the ionized gas pressure using the mean electron density obtained from the [Fe II] lines:  $\sim (4.7 \pm 0.7) \times 10^3 \text{ cm}^{-3}$ . Generally in a shocked gas, the [Fe II] lines are emitted in the far downstream where hydrogen atoms are mostly neutral (i.e. a gas with a low degree of ionization), at  $10^3$ - $10^4 \text{ K}$  (McKee et al., 1984; Hollenbach et al., 1989; Oliva et al., 1989). This occurs due to the ionization potential of the Fe atom is low ( $7.9 \text{ eV}$ ) and the far-UV

photons from hot shocked gas can penetrate far downstream to maintain the ionization state of  $\text{Fe}^+$ . We adopted a mean temperature of 5000 K as the temperature of the [Fe II] line emitting region. Consequently, we get a ionized gas pressure of  $(n_e + n_p) T = (4.7 \pm 0.7) \times 10^7 \text{ cm}^{-3} \text{ K}$ , which is approximately 3/5 of the pressure from the X-ray for N63A, indicating that the ionization fraction of the [Fe II] emitting gas is not high.

Besides, the ionization fraction of the post-shock region is expected to be low inside the line emitting region (Oliva et al., 1989). We estimated the density of the hydrogen nuclei as  $n_H \approx n_e / 0.11 \approx 4.3 \times 10^4 \text{ cm}^{-3}$ , if the mean ionization corresponds to 0.11 (Oliva et al., 1989), and using the mean electron density derived from the [Fe II] lines.

In addition, the total gas pressure (neglecting He) corresponds to  $p/k_B = (1 + f_e)/2f_e \times n_e T_e$ . We applied the pressures obtained from the X-ray emitting gas and the ionized gas to obtain:  $f_e \sim 0.42$ , consistent with a low ionization fraction.

The pre-shock density can be estimated from  $n \approx p/\mu_H v_s^2$ , where  $\mu_H = 2.34 \times 10^{-24} \text{ g}$  is the mean mass per hydrogen nuclei, including the cosmic abundance of He, and  $p$  is the ionized gas pressure. If we assume that the shock speed is  $v_s = 100 \text{ km s}^{-1}$ , the pre-shock density of the [Fe II] emitting gas corresponds to  $n \approx 30 \text{ cm}^{-3}$ .

For comparison, the pre-shock density may be estimated from the  $[\text{Fe II}]_{1.64\mu\text{m}}$  surface brightness, where for a shock propagating at  $100 \text{ km s}^{-1}$  into atomic gas of  $n_H = 100 \text{ cm}^{-3}$ , the brightness corresponds to  $2.5 \times 10^{-4} \text{ ergs cm}^{-2} \text{ s}^{-1} \text{ sr}^{-1}$  (McKee et al. 1984). On the other hand, for a shock propagating at  $80 - 150 \text{ km s}^{-1}$  into a gas of  $n_H = 1000 \text{ cm}^{-3}$  corresponds to a surface brightness of  $(0.3 - 2) \times 10^{-3} \text{ ergs cm}^{-2} \text{ s}^{-1} \text{ sr}^{-1}$ , if the gas-phase abundance of iron is solar (Hollenbach et al. 1989). We measured an  $[\text{Fe II}]_{1.64\mu\text{m}}$  brightness of  $(1.37 \pm$

$0.07) \times 10^{-4} \text{ erg s}^{-1} \text{ cm}^{-2} \text{ sr}^{-1}$ , and therefore we can expect that the pre-shock density is probably  $\leq 100 \text{ cm}^{-3}$  for N63A.

Also, we can use the  $f_e$  factor to estimate the pre-shock density, where  $n_H \approx n_e / 0.42 \approx 1.1 \times 10^4 \text{ cm}^{-3}$ , where  $n_e$  is the mean electron density obtained from the [Fe II] lines. Hollenbach & McKee (1989) estimated that the final compression factor would be  $\sim 80$  for a shock of  $100 \text{ km s}^{-1}$ . Then, the above post-shock density implies a pre-shock density of  $\sim 140 \text{ cm}^{-3}$ , which is similar to the pre-shock density obtained from the [Fe II] $_{1.64\mu m}$  brightness.

In previous researches, Shull (1983) estimated the pre-shock density for SNR N63A in the range  $\sim 50 - 300 \text{ cm}^{-3}$  from optical observations. Meanwhile, Caulet et al. (2012) also investigate the possible range of shock velocities and pre-shock hydrogen densities,  $n_H$ , based on mid-IR Spitzer observations in N63A's shocked lobes. Using radiative planar shock models which predict the intensities of [Ne II] $_{12.8\mu m}$ , [Ne III] $_{15.5\mu m}$ , [Fe II] $_{26\mu m}$  and [Si II] $_{34.8\mu m}$ , the pre-shock hydrogen density is estimated between  $n_H = 100 \text{ cm}^{-3}$  and  $n_H = 1000 \text{ cm}^{-3}$ , which implies shock velocities of  $\sim 60 \text{ km s}^{-1}$  and  $\sim 100 \text{ km s}^{-1}$ , respectively. Thus, the incident ram pressure exerted by the shock models ranges for  $1.9 \times 10^7 \text{ cm}^{-3} \text{ K}$  to  $5.3 \times 10^8 \text{ cm}^{-3} \text{ K}$ , respectively. The incident ram pressure estimated from our data is in agreement with the values predicted by these models.

In summary, the pre-shock properties of the emitting gas corresponds to a shock propagating at speed of  $\sim 100 \text{ km s}^{-1}$  into a gas of density  $\sim 30 \text{ cm}^{-3}$ , which implies a pressure of  $(4.7 \pm 0.7) \times 10^7 \text{ cm}^{-3} \text{ K}$ . These shock properties seems to explain roughly the observed parameters of the [Fe II] emission and the destruction of the dust grains.

## Chapter 3

# SNR N63A interacting with Molecular Clouds in the LMC

### 3.1 Introduction

Supernova (SN) explodes near their natal molecular clouds (MCs), and consequently we often see supernova remnants (SNRs) interacting with MCs. There are many observable effects on the MC when it is hit by the SN blast waves, because the shocks driven into the cloud can heat, compress, dissociate and accelerate the ambient medium. Therefore, SN explosions strongly affect the environment, and at the same time, the evolution of a SNR is strongly governed by the environment itself. The study of these interactions between SNRs and MCs provides a lab where we can study the stellar feedback in star formation, MC destruction, as well as the physics and chemistry of molecular shocks.

In our galaxy, most SNRs are located in the Galactic plane, and consequently the contamination by the foreground/background emission limits their usefulness. In this regard, the Large Magellanic Cloud (LMC) is a unique place

to study and identify SNRs interacting with MCs due to its proximity ( $\sim 50$  kpc), location (nearly face-on geometry and far-off from the galactic plane), relatively unobscured (low galactic foreground absorption), and also it has been extensively observed at nearly all wavebands. Approximately 25% of the known SNRs in the LMC show interaction with MCs (e.g. Banas et al. 1997, Desai et al. 2010). The number of known SNR interacting with MCs has increased over the last few years. The growing number of these interactions provides a valuable opportunity to study the shock physics, as well as to compare the strong SN shocks with other kind of shocks (e.g. wind shocks, outflows).

CO molecules are sensitive diagnostics to determine the density, temperature, and velocity structure of cold, dense clouds with high molecular content. Also, the detection of CO emission lines are a strong evidence for SNR interacting with MCs. Comparisons between  $^{12}\text{CO}$  J=2-1 and J=1-0 emission intensities are used to probe denser and warmer gas by ultraviolet radiation originated from the SN explosions. Besides, rotational transitions of molecular hydrogen ( $\text{H}_2$ ) emission lines are also an excellent indicator of SNR- MC interactions. The  $\text{H}_2$  line emission originates from the warm gas behind the part of the shock front expanding into the molecular cloud, where high columns of  $\text{H}_2$  can survive the passage of the shock.

In this research we aim to study N63A, which is an unique example where we can study the above topics without confusion from other sources along the line of sight. N63A is a young remnant ( $2 - 5 \times 10^3$  yr, Hughes et al. 1998) of the SN explosion of the most massive stars in a cluster in the LMC (the OB association NGC 2030, Lucke & Hodge 1970), which is currently expanding within a large H II region (N63, Henize 1956). In addition, N63A is also engulfing a molecular cloud, where many observations indicate that bright optical nebula inside N63A is a MC swept up by the SNR (e.g. cloud seen in absorption in X-ray, Warren

et al. 2003; only blueshifted emission from the shock-heated lobes, Shull 1983; IRAC colors associated with molecular shocks, Williams et al. 2006). Thus, the interaction SNR-MC is limited to the central portion of the SNR (e.g. galactic SNR G349.7+0.2; Dubner et al. 2004). For this reason, N63A is a prototypical SNR showing the impact of SN explosion on the cluster and its environment. On the other hand, large-scale CO surveys did not reveal significant MC associated with N63A (e.g. Cohen et al., 1988; Israel et al. 1993), and the NANTEN survey only detected a small cloud on the eastern border of the remnant (Yamaguchi et al. 2001).

This chapter is organized as follows. In section 3.2 we presented the ESO-SEST observations of CO and the infrared observations of H<sub>2</sub> toward N63A. In section 3.3, we present the clouds identified in the N63A region with their physical parameters obtained from the CO line emission observations. Also we show the molecular hydrogen emission measured toward N63A and the H<sub>2</sub> excitation diagram obtained using these observations. Finally, in section 3.4 we analyze the results of the two-temperature fits to explain the H<sub>2</sub> excitation diagram, as well as the properties of the molecular shocks.

## 3.2 Observations and Data

### 3.2.1 CO emission lines

Observations of <sup>12</sup>CO J=1–0 (at 115 GHz) and <sup>12</sup>CO J=2–1 (at 230 GHz) emission lines were taken on 2001 using the SEST (Swedish-ESO Submillimeter Telescope) at La Silla Observatory in Chile, with a full width beam at half maximum (FWHM) of 45" (11 pc linear size) and 23" (6 pc linear size), respectively. SEST was a single dish antenna of 15 m of diameter operating in the range of frequencies 70–365 GHz. The central coordinates of the mapped region are:  $\alpha$ : 05 h 35 m 48.31 s and  $\delta$ : -66° 01' 50" (J2000). To obtain the ra-

diation temperature of the sources, the images were corrected for the antenna efficiency  $\eta= 0.7$  and  $0.5$  for CO(1-0) and CO(2-1), respectively. Furthermore, the CO emission data are integrated over a velocity range from 277 to 291 km s<sup>-1</sup>.

### 3.2.2 H<sub>2</sub> 2.12 μm narrow-band

We obtained an H<sub>2</sub> 2.12μm narrow-band image of N63A on May, 2016, using the NIR camera SIRIUS (Simultaneous Infrared Imager for Unbiased Survey) on the IRSF (Infrared Survey Facility) 1.4 m telescope. This telescope is located at the South African Astronomical Observatory (SAAO). The SIRIUS camera has a field of view of 7.7' x 7.7' with a pixel scale of 0.45". The specifications of the H<sub>2</sub> 2.12μm narrow-band filter are:  $\lambda_{iso}= 2.1223 \mu\text{m}$ ,  $\lambda_0= 2.1214 \mu\text{m}$  and  $\Delta\lambda= 311.9 \text{ \AA}$ . We used a total exposure time of 3000 s (60s x 50).

The standard data reduction procedure was applied to the image (e.g. dark subtraction, flat-fielding, sky subtraction, and dithered-image-combining), and also performed photometric calibration making comparison with the 2MASS Point Source Catalog. We used K-band magnitudes for the photometric calibration, assuming that the magnitude of each star is the same between the corresponding band and filter image. The uncertainties of the photometric calibration coefficients correspond to ~10%.

### 3.2.3 Ancillary data

We complement our data set with the LMC HI map from Kim et al. (2003), which combines data from the Australian Telescope Compact Array (ATCA, Kim et al. 1998) and the Parkes Multibeam receiver (Staveley-Smith et al. 1997). The angular resolution of the HI data is 1 arcmin (a spatial resolution of 15 pc in the LMC). The HI data cube is integrated over the heliocentric

velocity range of 190 to 380 km s<sup>-1</sup>. The data cube has a velocity resolution of 1.65 km s<sup>-1</sup> approximately, a brightness temperature sensitivity of  $\sim 2.4$  K, and a column density sensitivity of  $7.2 \times 10^{18}$  per  $\sim 1.65$  km s<sup>-1</sup> channel.

Additionally, we use spectral observation data from Spitzer Space Telescope, where many rotational H<sub>2</sub> lines within the IRS wavelength range are detected (Caulet & Williams 2012). The SNR N63A was mapped at high resolution ( $R \sim 600$ ) and low resolution ( $R \sim 62$ -124), covering the wavelength range from 5 to 37  $\mu$ m. The total areas of the regions where the Spitzer IRS spectral maps were obtained correspond to: 156.805 arcsec<sup>2</sup> in N63A SW lobe, 101.592 arcsec<sup>2</sup> in N63A NE lobe and 101.726 arcsec<sup>2</sup> in N63A SE lobe (see Figure 3.1).

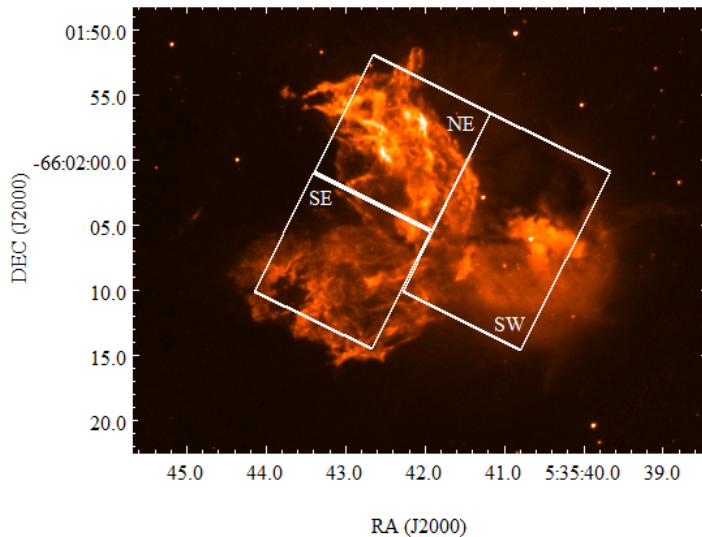


Figure 3.1: *HST H $\alpha$  image shows the regions where the spectral maps of SNR N63A were obtained using the Spitzer IRS, which correspond to the three lobed structure N63A's optical nebula. The abbreviated labels correspond to: NE = N63A NE lobe, SE = N63A SE lobe and SW = N63A SW lobe.*

### 3.3 Results

#### 3.3.1 Distribution of molecular clouds in the environs of N63A

The identification of the molecular clouds in the N63A region was done using the  $^{12}\text{CO}_{2-1}$  line emission observed with the SEST, which has an angular resolution twice that of the  $\text{CO}_{1-0}$  line emission. Figure 3.2 shows the integrated  $^{12}\text{CO}_{2-1}$  line emission in units of  $\text{K km s}^{-1}$  with the peak positions of the identified molecular clouds.

We use ClumpFind algorithm (Williams et al. 1994) to identify the individual molecular clouds. ClumpFind is an IDL procedure which works by effectively contouring the data array at many different levels, starting at a value close to the peak value in the array and working down to a specified minimum contour level. At each contour level, all contiguous areas of pixels that are above the contour level are found and considered in turn. If a set of pixels includes no pixels that have already been assigned to a clump, then it is marked as a new clump. If the set includes pixels that have already been assigned to a clump, then if such pixels belong to the same clump, the clump is extended to include these pixels in the set.

Table 3.1: *Molecular clouds identified in the SNR N63A region using  $^{12}\text{CO}_{2-1}$ .*

Cloud	$\alpha_{peak}$ (J2000)	$\delta_{peak}$ (J2000)	R pc	$L_{CO(2-1)}$ $\text{K km s}^{-1} \text{ pc}^2$	$r_{2-1/1-0}$
C1	5:35:50	-66:01:40	8.5	$790 \pm 68$	1.39
C2	5:35:53	-66:02:20	7.2	$413 \pm 49$	1.59
C3	5:35:42	-66:02:10	6.4	$273 \pm 40$	2.30

Table 3.1 lists the final set of individual molecular clouds identified with ClumpFind and their properties. Columns (2) and (3) summarize the peak

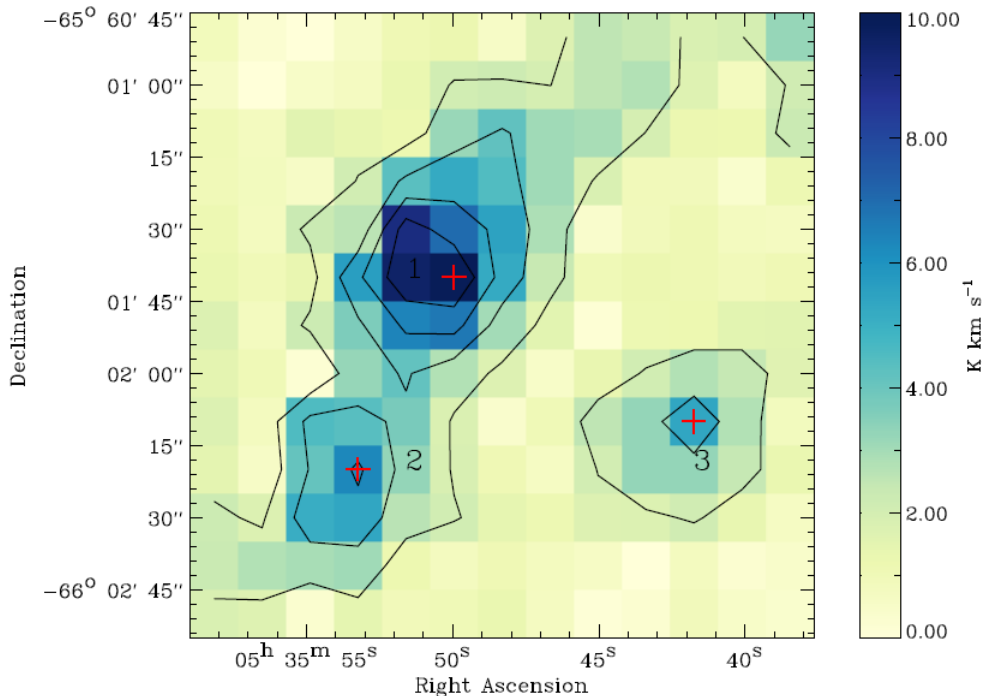


Figure 3.2: Integrated  $^{12}\text{CO}_{2-1}$  emission line of the N63A region observed with the SEST. Contours levels are from 2.0 to 8.0 by 2.0 in  $\text{K km s}^{-1}$ . Red crosses mark the position of the molecular clouds listed in Table 3.1

positions, i.e., their coordinates. The radii of each molecular cloud, shown in column (4), correspond to the equivalent circular radius which is obtained as  $R = \sqrt{N_{pix} \cdot A_{pix} / \pi}$ , where  $N_{pix}$  is the number of pixels assigned to the clump by ClumpFind, and  $A_{pix}$  is the area subtended by a single pixel. Column (5) lists the luminosity of  $^{12}\text{CO}_{2-1}$  emission. Also, we compute the average ratio of the intensity lines in  $\text{K km s}^{-1}$ ,  $r_{2-1/1-0}$ , for each molecular cloud by measuring the emission within an aperture defined by the size of the molecular clouds (see column (6) of Table 3.1).

In molecular clouds well apart from H II regions, the  $^{12}\text{CO J=2-1/J=1-0}$  ratios are found in the range 0.5 to 1.0, while  $r_{2-1/1-0}$  ratios larger than 1 are often observed toward molecular clouds interacting with H II regions (Sakamoto et al. 1994), where the high ratio can be explained in terms of externally heated clumps in the PDR. On the other hand, a very high  $r_{2-1/1-0}$  ratio is a marker of interaction with SNR (Seta et al. 1998), where this high ratio can be understood as CO lines emitted from warm and dense shocked gas. In case of smaller brightness temperature with comparable  $r_{2-1/1-0}$  ratio to other SNRs with larger brightness temperature, implies that either the shocked gas is composed by much smaller clumps or is less dense gas. In this regard, we expect that clumps C1 and C2 correspond to MCs interacting with the H II region N63, whereas clump C3 is consistent with a MC which is interacting with the SNR N63A.

Figure 3.3 shows the N63 H II region in  $\text{H}\alpha$  narrow-band with  $^{12}\text{CO}_{2-1}$  and Chandra X-ray contours overlaid. The molecular clouds identified as C1 and C2 overlaps the northeastern border of the N63A H II nebula. In fact, the eastern border of the H II region suddenly drops compared with the southeastern border of the nebula as shown in Figure 3.3. This may indicate the presence of a molecular cloud which blocks the  $\text{H}\alpha$  emission of the H II region. Furthermore, the  $^{12}\text{CO}_{2-1}$  emission of cloud C3 is coincident with the three-lobed structure of SNR N63A (seen in optical). As referred to earlier, many observations indicate that bright optical nebula inside N63A correspond to a molecular cloud swept up by the SNR, which resemble similar cases seen in other SNRs, e.g. the galactic SNR G349.7+0.2, where the interaction is limited to the central portion of the SNR.

Due to the absence of high angular and kinetic resolution images of the molecular CO emission, we cannot investigate the molecular shocks and re-

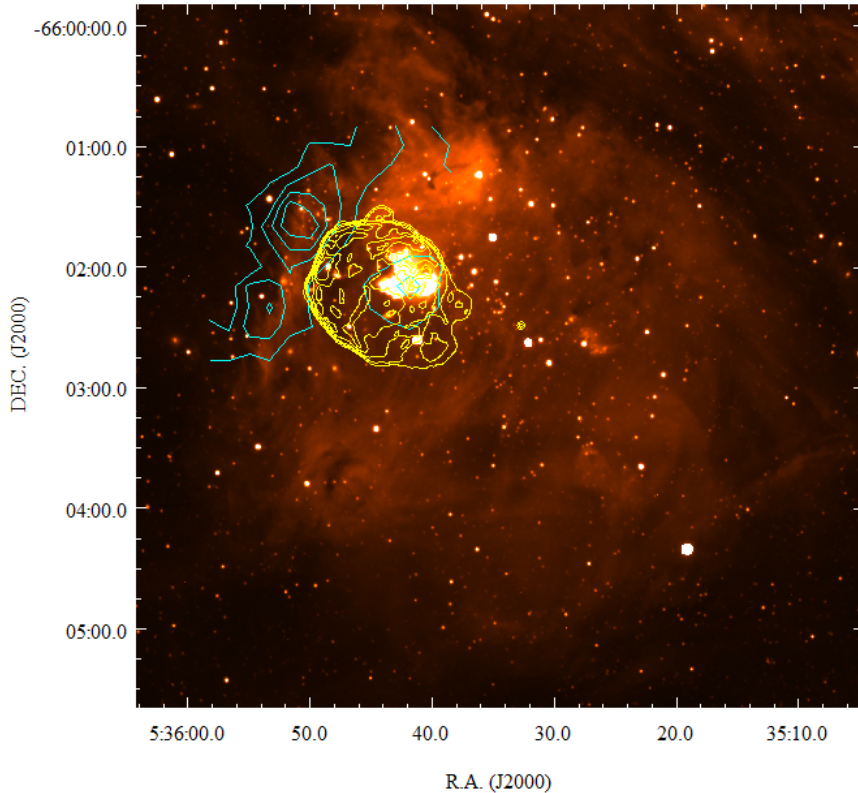


Figure 3.3:  $H\alpha$  image of the N63 H II region with  $^{12}\text{CO}_{2-1}$  (in cyan) and Chandra X-ray contours (in yellow) overlaid.  $^{12}\text{CO}_{2-1}$  emission of cloud 3 (C3) is coincident with the optical nebula of N63A. Abrupt drop of  $H\alpha$  emission in the region where the clouds 1 and 2 (C1; C2) are overlapped to the H II region.

veal the detailed structure of the shocked cloud using this information. On this subject, we are sure that future sub-millimeter observations of N63A (e.g observations using ALMA) can reveal unambiguously the internal structure of the shocked cloud, as well as the kinematical consequences of the impact of the SNR shock on the MC.

### 3.3.2 Molecular cloud masses and gas column densities

We estimate the masses of the molecular clouds based on the CO luminosity. The ratio between the CO<sub>1-0</sub> integrated intensity,  $W_{CO}$ , and the H<sub>2</sub> column density,  $N(\text{H}_2)$ , is the  $X_{CO}$ -factor ( $N(\text{H}_2) = X_{CO} W_{CO}$ ). In the Milky Way, empirical studies yield values in the range  $2 - 4 \times 10^{20} \text{ cm}^{-2} (\text{K km s}^{-1})^{-1}$ . However, several studies (e.g. Cohen et al. 1988; Israel et al. 1993; Hughes et al. 2010) show that the Galactic conversion factor does not apply to MCs in the LMC. In this work, we adopt the  $X_{CO(1-0)}$ -factor computed from the molecular clouds observed in the LMC (Hughes et al. 2010) which corresponds to  $4.7 \times 10^{20} \text{ cm}^{-2} (\text{K km s}^{-1})^{-1}$ .

To estimate the masses based on the CO luminosity ( $M_{CO}$ ) by using the  $X_{CO(1-0)}$  factor, we scale the  $L_{CO(2-1)}$  luminosities by the  $r_{2-1/1-0}$  ratio values, both listed in Table 3.1. The inferred CO luminosity masses are listed in column (2) of Table 3.2, and they range from 1 to  $6 \times 10^3 M_{\odot}$ . There is no previous studies which report the mass of these molecular clouds, except for cloud C3, where Warren et al. (2003) using the Chandra X-ray observations reported a mass of  $450 M_{\odot}$ , which is three times smaller than our estimation. This mass was determined by integrating the  $N_H$  map, obtained from the X-ray observations, over the region where is measured the hard X-ray spectra of N63A, which is close to the location of the N63A's optical nebula.

The main uncertainty on the CO masses comes from the  $X_{CO}$  factor as well as the detection of diffuse gas. First, we know that the LMC  $X_{CO}$  factor should be larger than the factor measured in the Milky Way because in low metallicity environments, the CO is dissociated by UV radiation from nearby massive stars. However, there is a wide range of values reported in the LMC, ranging from 2 to 6 times higher than in our galaxy. Second, the difference in

the mass estimation can be product of the detection of diffuse gas. Therefore, It is possible that the diffuse gas was consider in the mass derived using the CO observations, and probably this diffuse material could not be detected in the X-ray observations.

Table 3.2: *Physical parameters of the Clumps.*

Cloud	Mass	N(H <sub>2</sub> )	N (HI)	N <sub>H</sub>
	10 <sup>3</sup> M <sub>⊙</sub>	10 <sup>21</sup> cm <sup>-2</sup>	10 <sup>20</sup> cm <sup>-2</sup>	10 <sup>21</sup> cm <sup>-2</sup>
C1	5.7 ± 0.5	1.1 ± 0.1	9.4 ± 2.2	3.2 ± 0.3
C2	2.6 ± 0.3	0.74 ± 0.09	7.9 ± 2.2	2.2 ± 0.3
C3	1.2 ± 0.2	0.43 ± 0.06	5.5 ± 1.4	1.4 ± 0.2

In addition, we estimate the gas column density for each of three clouds identified in the N63A region. Table 3.2 shows the H<sub>2</sub> column density, N(H<sub>2</sub>), which is listed in column (3). To trace the atomic gas, we use the HI map published by Kim et al. (2003). The HI column density, N(HI), is obtained according to: N (HI) (cm<sup>-2</sup>) = 1.823 x 10<sup>18</sup> I<sub>HI</sub> (K km s<sup>-1</sup>), where the I<sub>HI</sub> is the HI data cube integrated over the heliocentric velocity range (Hughes et al. 2010), assuming the HI emission as optically thin (see column (4) of Table 3.2). Finally, column (5) lists the total gas column density, which is computed as: N<sub>H</sub>= N(HI) + 2 N(H<sub>2</sub>).

There is no previous report of the hydrogen column density for these clouds, except for cloud C3. Warren et al. (2003) reported a total column density of ~ 3.03 x 10<sup>21</sup> cm<sup>-2</sup> over a region coincident with the cloud 3, where is measured the hard X-ray spectra of N63A which includes the contribution of the molecular cloud as well as the Galactic extinction towards the LMC. Thus, the estimated column density attributed just to the molecular cloud by Warren et al. (2003) is

in the range  $N_H \sim (1.35 - 2.20) \times 10^{21} \text{ cm}^{-2}$ . Besides, the total column density for the entire SNR N63A was calculated from X-ray observations in the range:  $N_H \sim 1.1 \times 10^{21} \text{ cm}^{-2} - 1.4 \times 10^{21} \text{ cm}^{-2}$  (Schenck et al., 2016; Hughes et al., 1998).

Furthermore, in section 2.3.2 we estimated a total column density of  $N_H \sim 5.45 \times 10^{21} \text{ cm}^{-2}$  towards N63A using NIR observations, which includes the contribution the Galactic extinction towards the LMC. This column density is about 4 times larger than the column density given for the cloud 3 in Table 3.2. As mentioned above, the main uncertainty comes from the  $X_{CO}$  factor. If we adopt the LMC  $X_{CO(1-0)}$ -factor of  $1.7 \times 10^{21} \text{ cm}^{-2}$  computed by Cohen et al. (1988), we obtain an  $\text{H}_2$  column density of  $N(\text{H}_2) \sim 1.6 \times 10^{21} \text{ cm}^{-2}$ , which implies a total column density of  $N_H \sim 3.75 \times 10^{21} \text{ cm}^{-2}$ , which is 1.5 times smaller than the total column density obtained from NIR lines.

### 3.3.3 Observations of Molecular Hydrogen in SNR N63A

Molecular hydrogen ( $\text{H}_2$ ) is the most abundant molecule in the Universe and plays a crucial role in the ISM as a catalyst of chemistry and a major coolant. This molecule is excited by energetic processes (e.g. shocks and photodissociation regions), with many bright emission lines in the near- and mid-IR available as diagnostics of the excited gas. Thus,  $\text{H}_2$  lines can be used as excellent diagnosis of physical conditions in the shocked gas, because high columns of  $\text{H}_2$  can survive the passage of the shock, being an evidence of the interaction between SNRs and MCs. Infrared  $\text{H}_2$  emission lines have been frequently observed in SNRs interacting with nearby clouds.

Figure 3.4 shows the  $\text{H}_2$   $2.12\mu\text{m}$  line map obtained using SIRIUS/IRSF for N63A. For comparison we used the  $[\text{Fe II}]_{1.64\mu\text{m}}$  emission line map observed with SIRIUS/IRSF. According to this, the  $\text{H}_2$   $2.12\mu\text{m}$  emission is located in a

region which has a good spatial correlation with the emitting region of the  $[\text{Fe II}]_{1.64\mu\text{m}}$  emission, demonstrating that the molecular and the ionic shocks arise from the same region. Also the  $\text{H}_2$  emission is detected from a region toward the west, which has a similar location compared with the third lobe of the optical nebula of N63A, identified as a photoionized region. We did not detect any other  $\text{H}_2$  emission from other locations associated within or outside the SNR N63A.

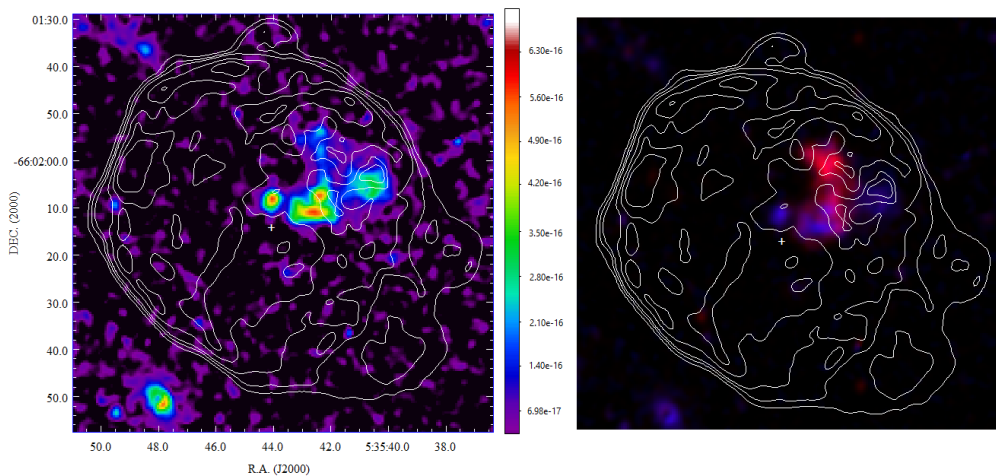


Figure 3.4: (Left)  $\text{H}_2$   $2.12\mu\text{m}$  line map observed with SIRIUS/IRSF; (right) color composed image of  $[\text{Fe II}]_{1.64\mu\text{m}}$  emission (red) and  $\text{H}_2$   $2.12\mu\text{m}$  emission (blue). Both images were smoothed with a Gaussian kernel of 3 in sigma. The color levels are given in units of  $\text{erg s}^{-1} \text{cm}^{-2} \text{pix}^{-1}$ . Cross marks denote the center position of SNR N63A. Chandra X-ray contours are overlaid.

In the color composed image using  $[\text{Fe II}]_{1.64\mu\text{m}}$  and  $\text{H}_2$   $2.12\mu\text{m}$  line maps, we appreciate that the  $\text{H}_2$  peak is located in the southeastern lobe, whereas the  $[\text{Fe II}]$  peak comes from a region in the northeastern lobe of the nebula (see also Figure 3.5). We detected an  $\text{H}_2$   $2.12\mu\text{m}$  line brightness of  $(1.5 \pm 0.2) \times 10^{-5} \text{ erg s}^{-1} \text{cm}^{-2} \text{sr}^{-1}$  from a region of dimensions  $\sim 19'' \times 8''$  centered

at  $\alpha$ :  $5^h 35^m 42.47^s$ ,  $\delta$ :  $-66^\circ 02' 04.86''$  (same region used to obtain the line intensities in section 2.3.1), which correspond to the the bright part of the two-lobed structure seen in the  $[\text{Fe II}]_{1.64\mu\text{m}}$  line map. Additionally, we measured the  $\text{H}_2$   $2.12\mu\text{m}$  flux of  $(1.7 \pm 0.2) \times 10^{-13} \text{ erg s}^{-1} \text{ cm}^{-2}$ . The surface brightness and flux of the  $\text{H}_2$  emission are de-reddened using the hydrogen column density toward this source obtained from the NIR  $[\text{Fe II}]$  lines (section 2.3.2), which correspond to  $(1.6 \pm 0.2) \times 10^{-5} \text{ erg s}^{-1} \text{ cm}^{-2} \text{ sr}^{-1}$  and  $(1.8 \pm 0.2) \times 10^{-13} \text{ erg s}^{-1} \text{ cm}^{-2}$ , respectively. The  $\text{H}_2$   $2.12\mu\text{m}$  line brightness is  $\sim 10$  times weaker than the  $[\text{Fe II}]_{1.64\mu\text{m}}$  line brightness measured in the same region.

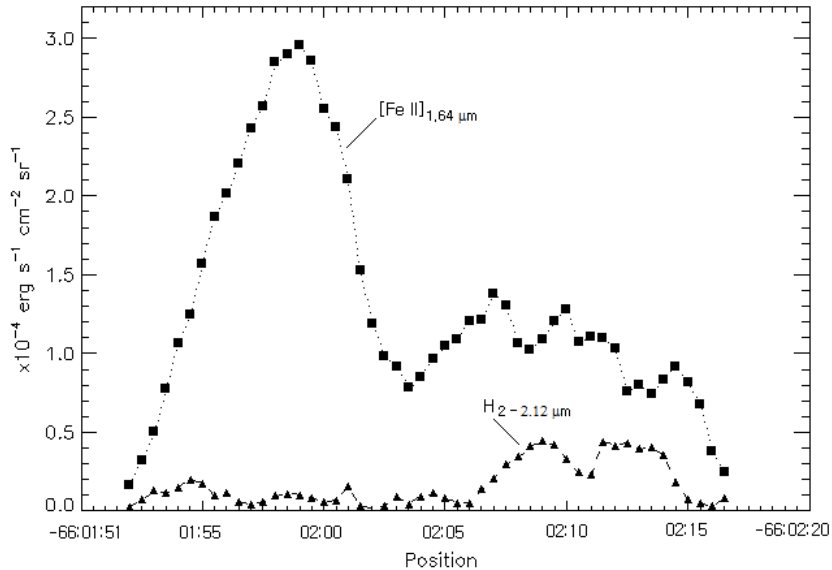


Figure 3.5: *Distribution of the  $[\text{Fe II}]_{1.64\mu\text{m}}$  and  $\text{H}_2$   $2.12\mu\text{m}$  emission along the bright emission of N63A's two-lobes with position RA:  $05^h 35^m 42.5^s$  and declination given in the X axis.*

### 3.3.4 H<sub>2</sub> excitation diagram of N63A

In this research, we also used the mid-infrared H<sub>2</sub> emission lines detected in N63A, which are obtained from the Spitzer IRS spectral observations (Caulet & Williams 2012). The spectral map observations were done in three different regions (see Figure 3.1) which compose the three-lobes structure of N63A: SW Lobe (photoionized), NE Lobe and SE Lobe (both shock-heated).

The detected H<sub>2</sub> lines correspond to: S(0) at 28  $\mu\text{m}$ , S(1) at 17  $\mu\text{m}$ , S(2) at 12  $\mu\text{m}$ , S(3) at 9.6  $\mu\text{m}$ , and S(5) at 6.9  $\mu\text{m}$ . There is no detection of H<sub>2</sub> S(4) - 8  $\mu\text{m}$ , S(6) - 6.1  $\mu\text{m}$  and S(7) - 5.5  $\mu\text{m}$  lines. We combine these mid-IR observations with the NIR H<sub>2</sub> - 2.12  $\mu\text{m}$  line map, where we measured the line intensities in the same regions mapped in the Spitzer spectra. All the H<sub>2</sub> intensity lines are listed in Table 3.3.

The H<sub>2</sub> emission from N63A is probably collisionally excited from a shock (e.g. SNR IC 443, SNR RCW103). We can see that the lines leading the bright emission of molecular hydrogen correspond to S(3) and S(5) pure rotational lines in the SE and NE lobes, which correspond to the shock-heated region of N63A. Besides, the H<sub>2</sub> emission in the SW lobe is essentially purely fluorescent with no influence from collisional processes. Also, the H<sub>2</sub> emission is higher in the SE lobe compared with the NE and SW lobes, which is in agreement with the H<sub>2</sub>-2.12  $\mu\text{m}$  line emission.

We used the H<sub>2</sub> line intensities listed in Table 3.3 to derive the observed column densities of the levels from which these transitions arise. All molecular hydrogen lines remain optically thin due to the small radiative transition probabilities. Therefore, the corresponding ‘‘observed’’ upper level column density can be computed from the observed line flux as:

$$N_{obs} = (4 \pi \lambda / h c) I_{obs}(v, J \rightarrow v', J') / A(v, J \rightarrow v', J')$$

Table 3.3: *Observed H<sub>2</sub> lines in the N63A region.*

Line	$\lambda$	$g(J)$	$E_{upper}$	A	Brightness <sup>a</sup> $10^{-5}$ erg s <sup>-1</sup> cm <sup>-2</sup> sr <sup>-1</sup>			Ref. <sup>b</sup>
	$\mu\text{m}$	upper	K	$10^{-7}$ s <sup>-1</sup>	SW lobe	NE lobe	SE lobe	
0-0 S(0)	28.2	5	510	0.0003	0.17 (0.02)	0.15 (0.02)	0.15 (0.02)	(1)
0-0 S(1)	17.0	21	1015	0.0048	1.76 (0.36)	0.97 (0.03)	2.18 (0.03)	(1)
0-0 S(2)	12.2	9	1682	0.0276	1.30 (0.05)	0.44 (0.06)	2.33 (0.07)	(1)
0-0 S(3)	9.66	33	2504	0.0984	1.81 (0.12)	1.51 (0.09)	7.68 (0.12)	(1)
0-0 S(5)	6.90	45	4586	0.588	0.43 (0.05)	1.28 (0.05)	6.36 (0.05)	(1)
1-0 S(1)	2.12	21	6956	3.47	0.73 (0.07)	0.94 (0.09)	1.72 (0.17)	(2)

(<sup>a</sup>) De-reddened emission lines, with errors shown in parenthesis. The observed H<sub>2</sub>-2.12  $\mu\text{m}$  lines emission ( $f_{obs\ 2.12\mu\text{m}}$ ) are de-reddened as follows:

$f_{0\ 2.12\mu\text{m}} = f_{obs\ 2.12\mu\text{m}} / e^{-\sigma_{2.12,H} N_H}$ , with the hydrogen column density ( $N_H$ ) toward this source obtained from near-IR [Fe II] lines. To derive the hydrogen column density we use:  $N_H = -\ln([Fe\ II]_{1.26/1.64})_{obs} / ([Fe\ II]_{1.26/1.64})_{int} / (\sigma_{1.26,H} - \sigma_{1.64,H})$

where the observed flux ratio of [Fe II]<sub>1.26/1.64</sub> is 1.30, obtained from the SIR-IUS/IRSF data aforementioned, and the intrinsic flux ratio of ([Fe II]<sub>1.26/1.64</sub>)<sub>int</sub> corresponds to 1.36 (Nussbaumer & Storey, 1988)

(<sup>b</sup>) References for the observed line: (1) Caulet & Williams (2012); (2) This work.

where  $I_{obs}(v,J \rightarrow v',J')$  and  $A(v,J \rightarrow v',J')$  are the observed line flux and the Einstein-A radiative transition probability of the transition from level (v,J) to (v',J'), respectively. A convenient way to visualize the level column densities is to divide them by the level degeneracy  $g(J)$  and plot this against the upper level energy,  $E_{upper}$ . All these parameters are given in Table 3.3. The excitation diagram from the de-reddened brightnesses of the H<sub>2</sub> lines is presented in Figure 3.6.

This test is used to discriminate between thermal and non-thermal excitation of the H<sub>2</sub> IR lines, where thermal excitation is characterized by a smooth distribution between subsequent ortho- and para-states, whilst many jumps are expected if the lines are produced by non-thermal mechanisms. Some curvature

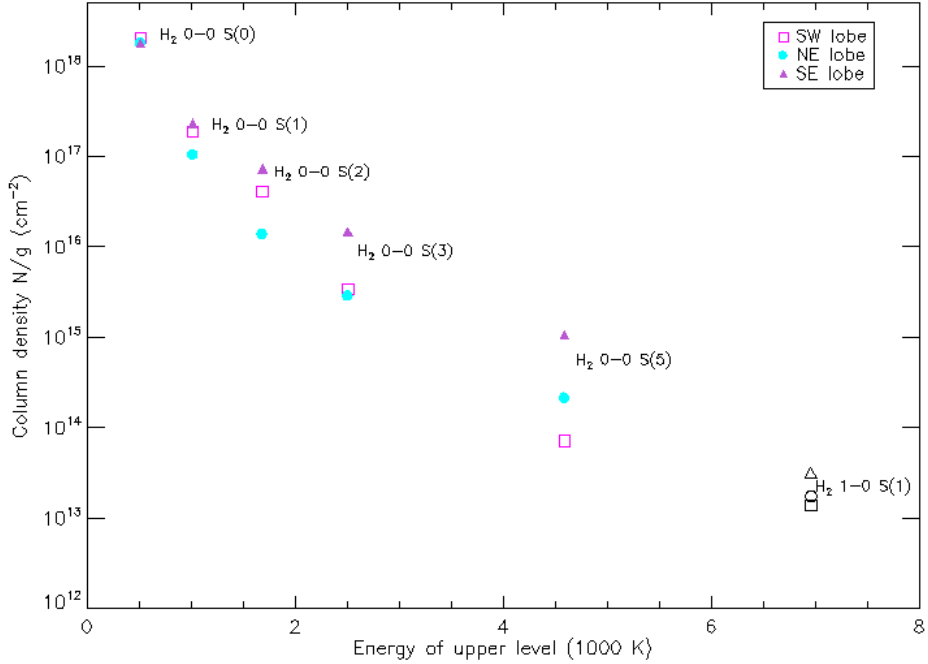


Figure 3.6:  $H_2$  excitation diagram of  $N63A$ . The IRS data are marked as magenta squares (SW lobe), cyan circles (NE lobe) and purple triangles (SE lobe). The square, circle and triangle in black represent the SIRIUS/IRSF  $H_2 - 2.12 \mu\text{m}$  data for the SW, NE and SE lobes, respectively.

is expected if there are components at different temperatures contributing to the line emission.

## 3.4 Discussion

### 3.4.1 Excitation of Molecular Hydrogen

We assume that the lines are optically thin, the radiation is isotropic and the rotational levels of  $H_2$  are thermalized. Under these assumptions, the level pop-

ulation follows the Boltzmann distribution law at a given temperature.

The total H<sub>2</sub> column densities  $N(\text{H}_2)_{tot}$  can be determined in the local-thermal equilibrium (LTE) condition, using:  $N/g = N(\text{H}_2)_{tot} e^{-E_j/kT} / z(T)$ , where  $z(T)$  is the partition function. We have fit the H<sub>2</sub> excitation diagram data using a model of two-temperature LTE for each of the regions (i.e. SE lobe, NE lobe and SW lobe of N63A). It is clear that a simple LTE excitation model for the observed H<sub>2</sub> lines cannot fit both curvatures from a range of gas temperatures.

The results of the two-temperature LTE best fits from the least squares fitting are shown in Figure 3.7. The dashed line shows the contribution of the warm component ( $N1(\text{H}_2)$ , T1), while the dotted line shows the contribution of the hot component ( $N2(\text{H}_2)$ , T2). The temperatures and total H<sub>2</sub> column densities obtained for the two temperature distributions are listed in Table 3.4. We also note that the values obtained for the warm and hot component in the Boltzmann distribution show similar results for the three regions (the two shock heated regions and the photoionized region).

Table 3.4: *Fitted Excitation Parameters to Observed Molecular Hydrogen Lines.*

Parameter	SE lobe	NE lobe	SW lobe
T1 (K)	$373 \pm 89$	$244 \pm 43$	$304 \pm 62$
$N1(\text{H}_2) \text{ cm}^{-2}$	$5.22 \times 10^{19}$	$7.10 \times 10^{19}$	$6.86 \times 10^{19}$
T2 (K)	$726 \pm 32$	$874 \pm 42$	$814 \pm 221$
$N2(\text{H}_2) \text{ cm}^{-2}$	$8.19 \times 10^{18}$	$1.05 \times 10^{18}$	$1.39 \times 10^{18}$

Previous studies of IR H<sub>2</sub> emission lines observed in SNRs interacting with nearby clouds present a common result. These show that the H<sub>2</sub> level-population diagram exhibits an “ankle-like” curve, which has been usually interpreted as

a population of two temperature ( $\sim 10^2$  and  $\sim 10^3$  K)  $\text{H}_2$  gas in LTE. Such a population cannot be explained by a single planar shock model.

Hewitt et al. (2009) presents the excitation diagrams of molecular hydrogen for six galactic SNRs (Kes 69, 3C 396, Kes 17, G346.6-0.2, G348.5-0.0 and G349.7+0.2), where the  $\text{H}_2$  emission has a warm component with temperatures in the range 250 to 550 K and a column density in the range  $10^{19}$  to  $10^{20}$   $\text{cm}^{-2}$ , and a hot component with temperatures  $\sim 1000 - 2000$  K and column densities  $\sim 10^{18}$  to  $10^{19}$   $\text{cm}^{-2}$ . In the case of the galactic SNR G357.7+0.3, Rho et al. (2017) found that the warm component has a temperature and column density of 197 K and  $\sim 10^{21}$   $\text{cm}^{-2}$ , respectively, while in the hot component, the temperature and column density correspond to 663 K and  $\sim 10^{19}$   $\text{cm}^{-2}$ , respectively.

According to the results of this research, N63A presents a warm temperature in the range of temperatures exhibited by these galactic SNRs. For the hot component of N63A, it shows a lower temperature than the most of the SNRs, except for the galactic SNR G357.7+0.3.

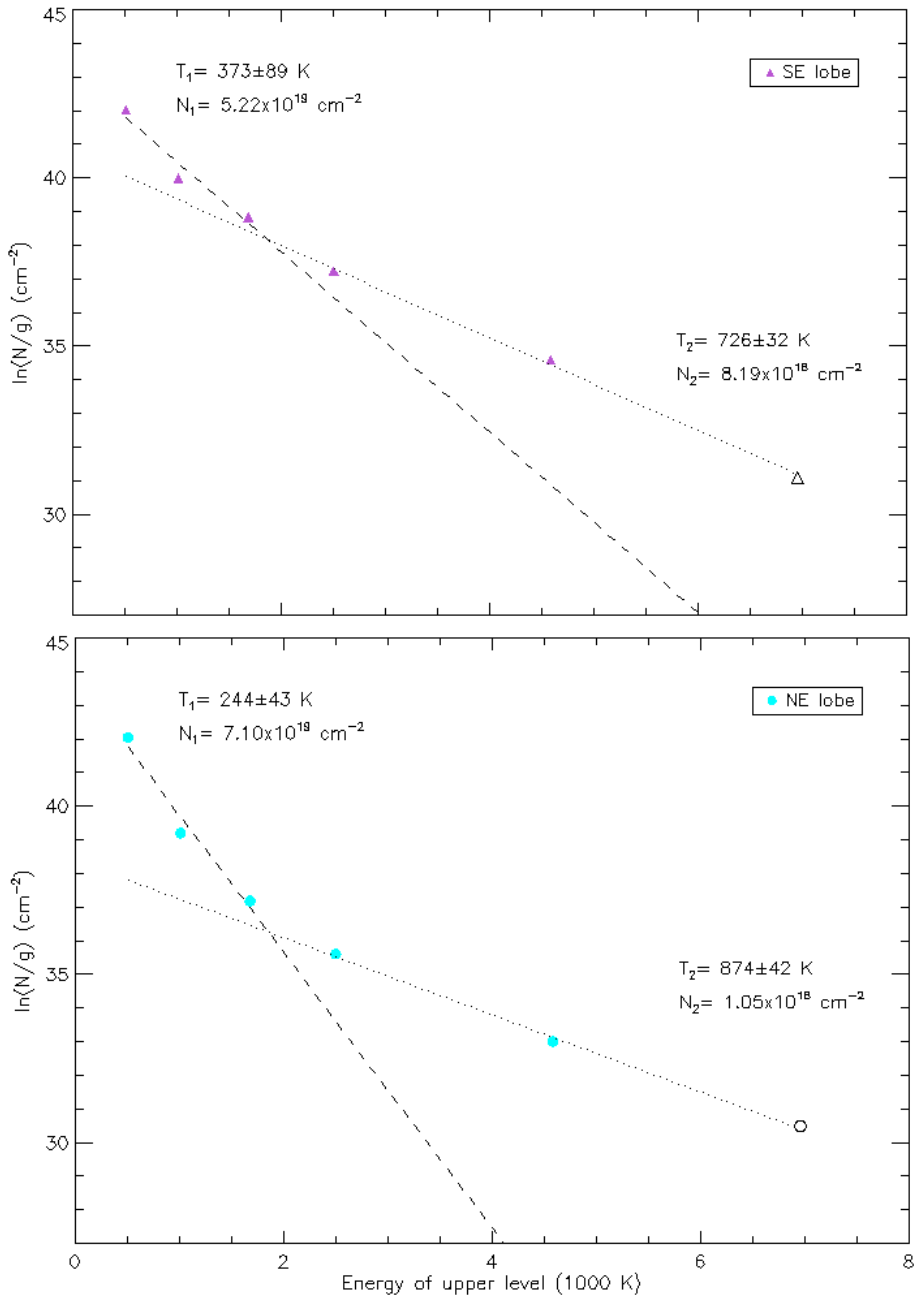


Figure 3.7: The two-temperature LTE model fitted to the  $H_2$  excitation diagram for each region in N63A. The dashed and the dotted lines show the contribution of the warmer and the hotter component, respectively.

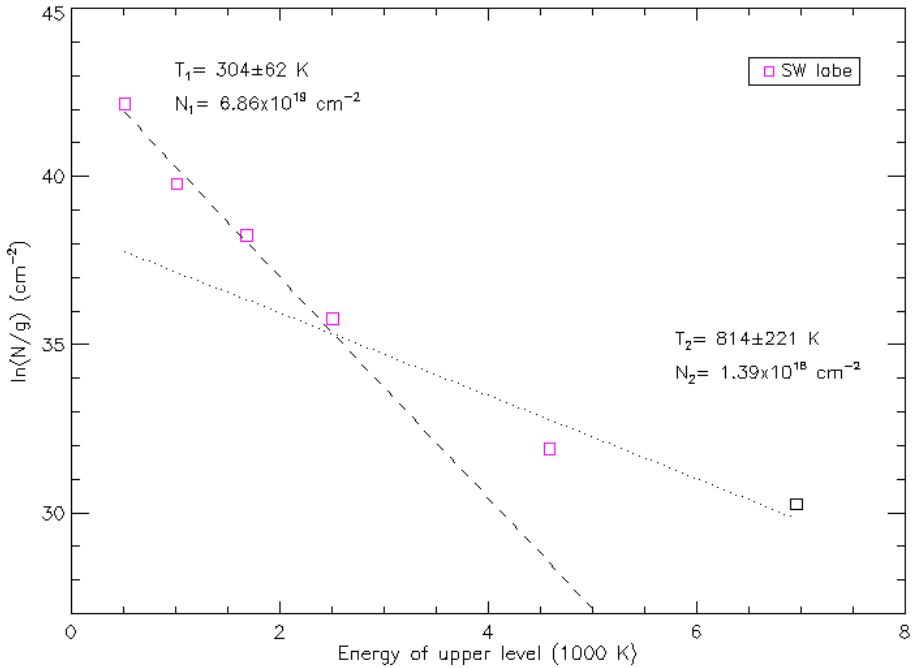


Figure 3.7: *Continued.*

### 3.4.2 Implication of Shock Models from Molecular Hydrogen

Many mechanisms have been proposed in order to explain the two-temperature level population distribution (e.g. a partially dissociative J-shock, a bow shock, a nonstationary shock, etc), but the interpretation of the  $\text{H}_2$  population diagram is still under debate.

In general, shocks propagating into molecular clouds are divided in C-type and J-type shocks depending on whether the physical quantities vary continuously or discontinuously. There is a significant difference in the physical properties of  $\text{H}_2$  behind the different shocks. Behind a nondissociative C-type shock, the  $\text{H}_2$  molecules are heated without being dissociated and they are continu-

ously accelerated to high velocities. The neutral gas temperature behind such shocks reaches  $10^3$  K and then cools rapidly, leading to bright emission from the S(3) and S(5) pure rotational lines (Draine et al., 1983). On the other hand, in the case of J-type faster shocks,  $\text{H}_2$  molecules are destroyed and the H ionized, but the molecules are reformed ( $\sim 10^{17}$  cm behind the shock) when the shock has swept up enough column density. The cooling is somewhat slower because of the lower density, leading to bright emission from the S(7) and S(9) pure rotational lines (Hollenbach & McKee 1989).

Previous studies compare the observed  $\text{H}_2$  emission lines with a grid of shock models. These galactic SNRs generate an equivalent quality of the fitting between a model of two C-shocks and a combination of C- and J-shock models (eg. Rho et al., 2017; Hewitt et al., 2009), over a single shock model which cannot reproduce the positive curvature observed in the Boltzmann diagrams. A slow C-shock gives the best fit to the lower excitation lines (e.g.  $\text{H}_2$  S(1)), but cannot predict the observed brightness of higher excitation lines. In this regard, a second faster C-shock or a fast J-shock show a good fit to the higher excitation lines. A combination of two C-shocks is generally better to reproduce the observed excitation in these galactic SNRs.

We compare the results of the observed  $\text{H}_2$  emission in N63A with published shock models. We used models of slow C-shocks (Wigenbus et al. 2000) and fast J-shock models (Hollenbach & McKee 1989). We reduced the predicted  $\text{H}_2$  intensities, due to they are typically more than an order of magnitude brighter than the observed  $\text{H}_2$  line emission in N63A. The fit to the observed  $\text{H}_2$  lines was performed using a least squares fitting. The results are shown in Figures 3.8 and 3.9.

No single shock was found that can reproduce the  $\text{H}_2$  excitation diagram, and therefore it is required a combination of models. A slow C-shock of  $v_s =$

10 km s<sup>-1</sup> and density n= 10<sup>6</sup> cm<sup>-3</sup> gives a good fit to the lower excitation lines of the SE and NE lobes of N63A. However, in the case of the NE lobe, the model underestimates the observed brightness of the H<sub>2</sub> 28 μm line. We also found other two slow C shocks: n= 10<sup>4</sup> cm<sup>-3</sup> and v<sub>s</sub>= 10-20 km s<sup>-1</sup>, and n= 10<sup>3</sup> cm<sup>-3</sup> and v<sub>s</sub>= 20-40 km s<sup>-1</sup>, which have larger χ<sup>2</sup> compared with the C-shock of n= 10<sup>6</sup> cm<sup>-3</sup> and v<sub>s</sub>= 10 km s<sup>-1</sup>, but also they fit well to the data. The J-shock models do not fit well to the lower excitation lines. In addition, in general an OPR of 3 reproduces well the observed lines. An OPR observed at equilibrium suggests that the shock has had sufficient time to establish a steady state C-shock.

In the case of the higher excitation lines, these cannot be predict using the J-shock models due to these models underestimated the molecular hydrogen corresponding to the S(3) and S(5) pure rotational lines. A second C-shock with a velocity a little higher but the same density shows a better results to the higher excitation lines. However, it is necessary to test fast C- shocks models to fit the high excitation component of the H<sub>2</sub>, which will be done in a future work.

We can check the validity of the fitting results comparing the shock model fits to the simple analytic treatment of energy conservation in C-shocks given by Neufeld et al. 2006, where the characteristic gas temperature of a C-shock is given by  $T_s = 375 b^{-0.36} (v_s / 10 \text{ km s}^{-1})^{1.35} \text{ K}$ , where  $b = B / \mu G (n_0 / \text{cm}^{-3})^{-0.5}$ , assuming the standard value of b= 1. The results are, in general, in agreement with the parameters fitted to de H<sub>2</sub> diagrams.

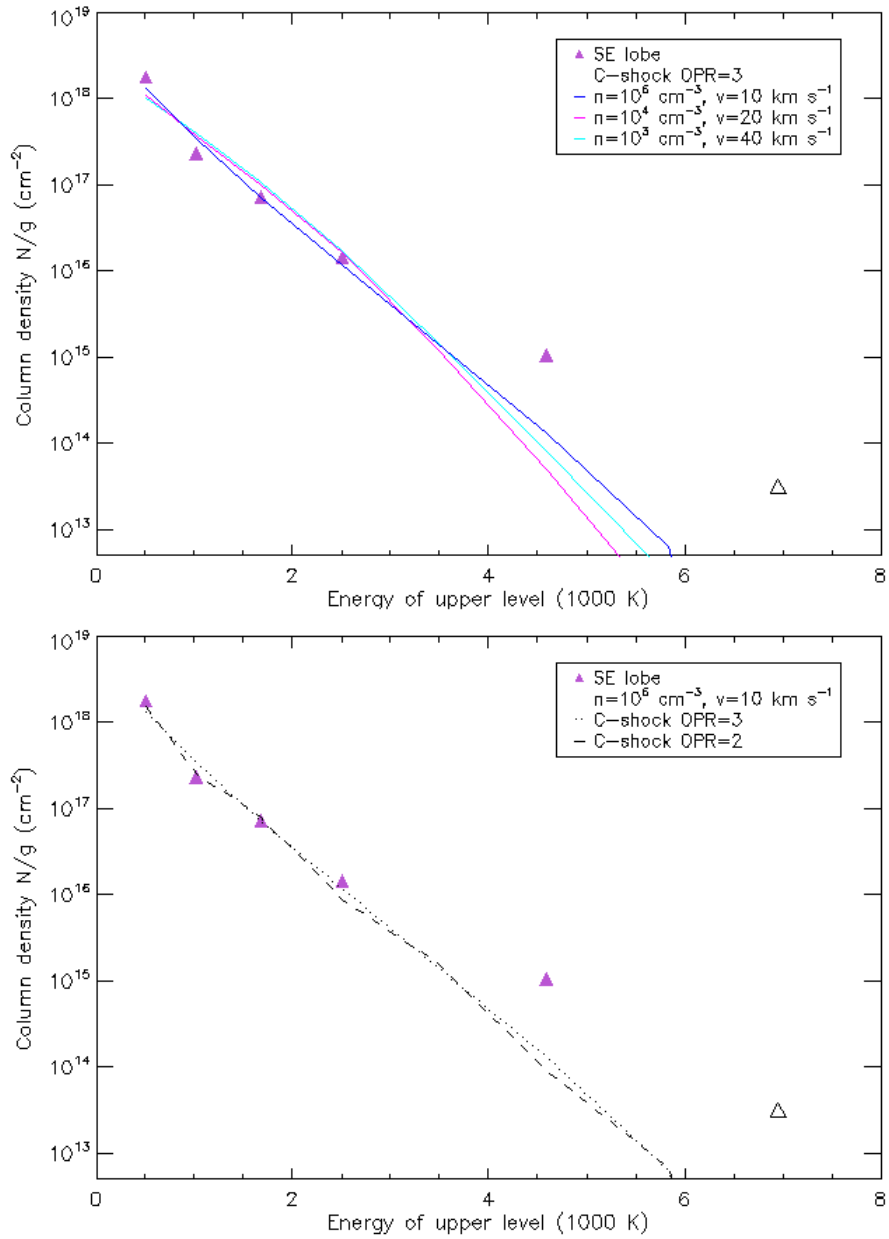


Figure 3.8: *C*-shock fitted to the observed excitation of  $\text{H}_2$  in the warm component for the SE and NE lobes regions of N63A. The dotted line shows the contribution of the slower shock.

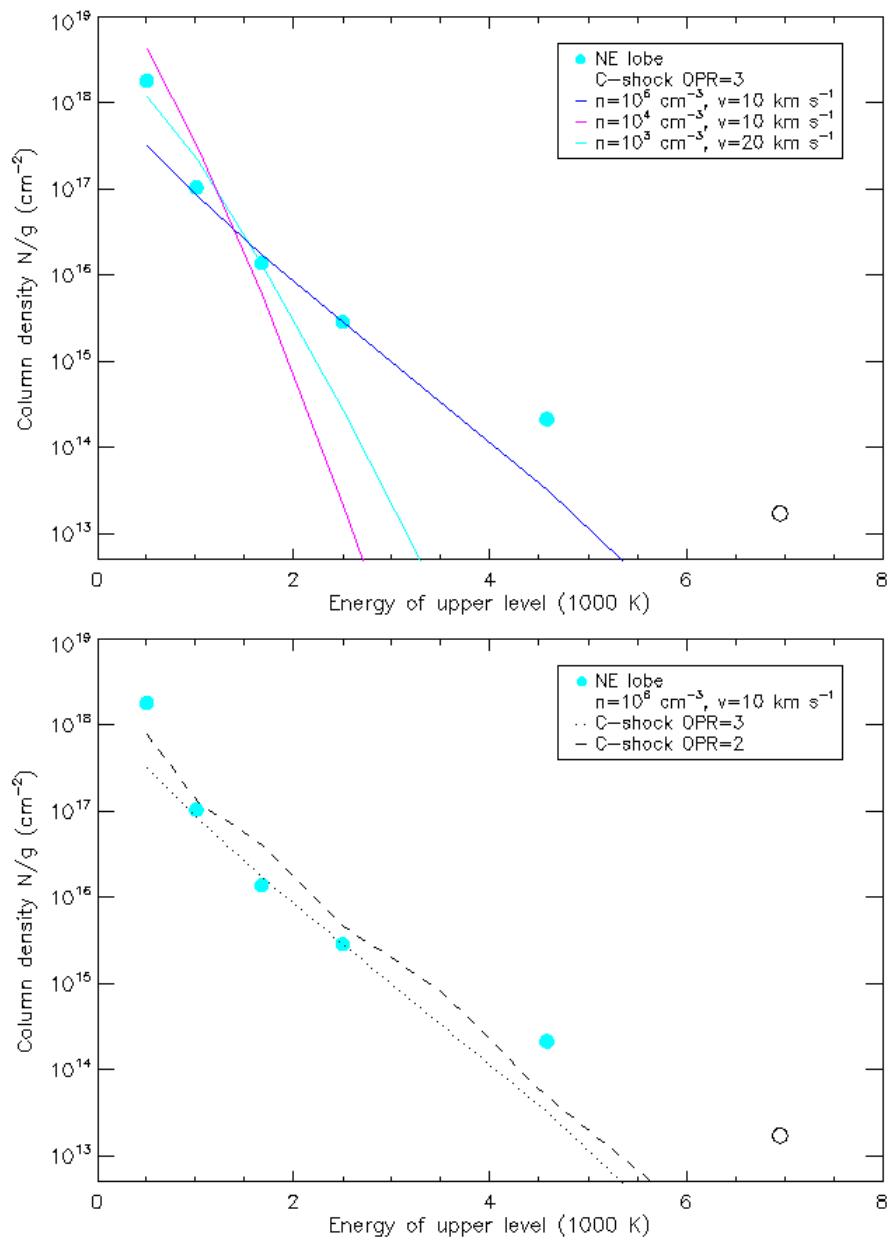


Figure 3.8: *Continued.*

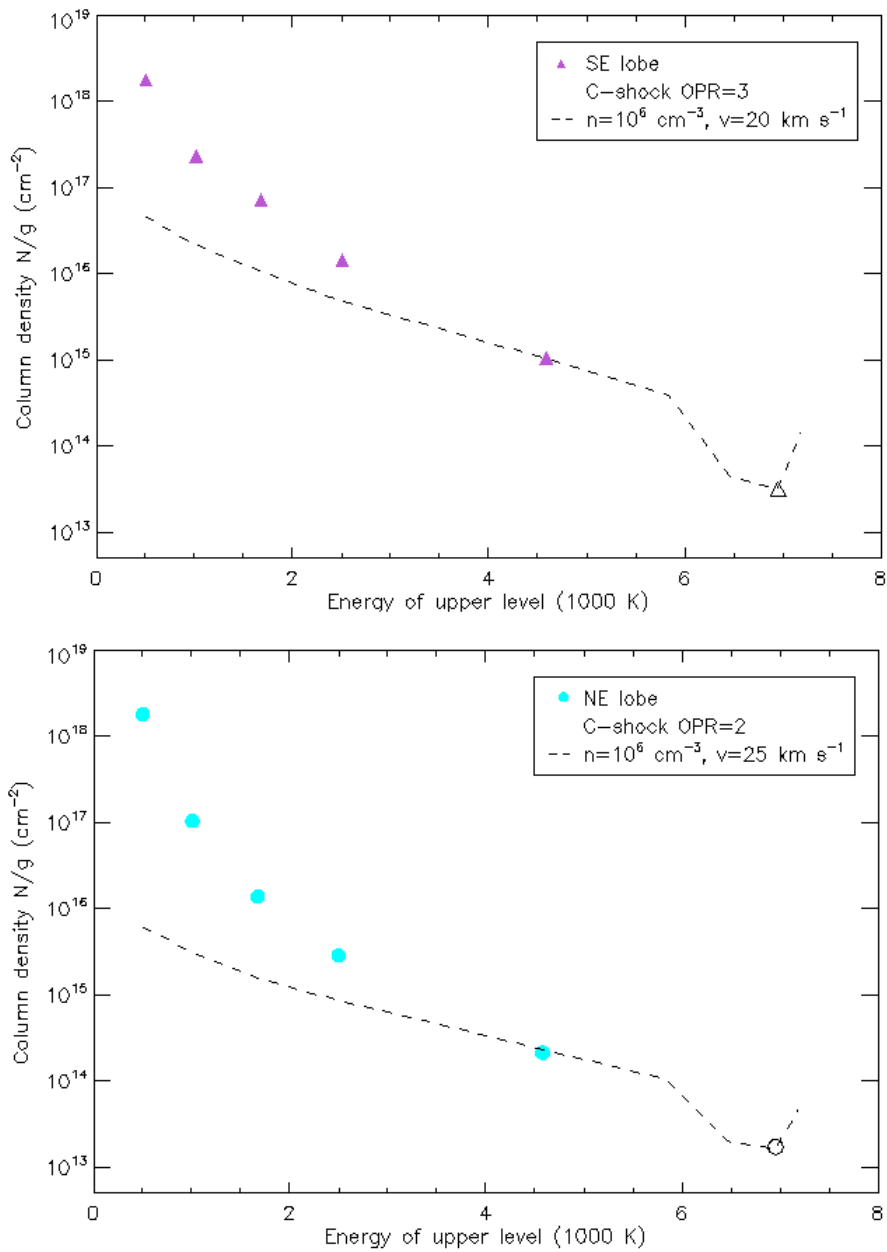


Figure 3.9: *C*-shock fitted to the observed excitation of  $H_2$  in the hot component of the SE and NE lobes regions of N63A.

### 3.4.3 Comparison of Molecular and Ionic Shocks

N63A shows a large range of pressures. We determine the shock ram pressure from the shock modeling studied in section 3.4.2, where is obtained the best fit parameters from C-shocks derived from H<sub>2</sub> line observations. Although the pressure derived from the shock models may have large uncertainties, the H<sub>2</sub> emission is originated from regions where the pressure is  $\sim 2 \times 10^{-6}$  dyn cm<sup>-2</sup> using a slow C-shock of  $v_s = 10$  km s<sup>-1</sup> and density  $n = 10^6$  cm<sup>-3</sup>, if we consider only the warm component of the H<sub>2</sub> distribution for the SE-and NE-lobes of N63A.

The incident pressure is derived in section 2.4.1 from the best fast and diffuse J-shock traced by ionic lines. The pression obtained from the NIR [Fe II] lines correspond to  $\sim 6.5 \times 10^{-9}$  dyn cm<sup>-2</sup>. This estimation is in the range of the incident ram pressure exerted by the shocks measured using mid-IR ionic lines in N63A's shocked-lobes (Caulet et al., 2012), which ranges from  $2.6 \times 10^{-9}$  dyn cm<sup>-2</sup> to  $7.3 \times 10^{-8}$  dyn cm<sup>-2</sup>. The pressure estimated from the [Fe II] lines is 300 times smaller than the pressure derived from the C-shocks. In general, the pressure estimated from molecular shocks (C-shocks) are comparable with the thermal pressure of the remnant. Although, there are some exceptions, like the galactic SNR G346.6-0.2, where the ionic pressure is two orders lower than the pressure from the C-shocks.

If we use the other two C-shock models that fit to the H<sub>2</sub> data, we found a pressure in the range of  $\sim (2-9) \times 10^{-7}$  dyn cm<sup>-2</sup> for a C-shock of  $n = 10^4$  cm<sup>-3</sup> and  $v_s = 10-20$  km s<sup>-1</sup>, and a pressure in the range of  $(0.9-4) \times 10^{-8}$  dyn cm<sup>-2</sup> for a C-shock of  $n = 10^3$  cm<sup>-3</sup> and  $v_s = 20-40$  km s<sup>-1</sup>. This last is more comparable to the ionic pressure in N63A.

As we mentioned in section 2.4.1, the pressure of the hot thermal X-ray gas

observed in the interior of the SNR N63A is estimated to be of the order  $1.1 \times 10^{-8} \text{ dyn cm}^{-2}$  (from the Chandra X-ray observations by Warren et al. 2003), which is smaller but in the same order of the shock pressure derived from the ionic line diagnostics.

We can interpret that the Fe II and H<sub>2</sub> emission are tracing independent shocks in N63A. On the one hand, Fe II traces fast, grain-destroying shocks into  $n < 10^3 \text{ cm}^{-3}$  gas, whereas H<sub>2</sub> traces denser shocks. Their correspondence on the sky probably reflects the preshock structure of the molecular cloud. When approaching a dense portion of the molecular cloud, the blast wave first encounters the less dense material at its surface, yielding the ionic shocks. Then, slower shocks begin propagating into the denser material, yielding the molecular shocks.

#### 3.4.4 The photoionized region of N63A

The HST image (Figure 2.2) shows the structure of the SW lobe of N63A as an ionized cavity illuminated by a bright star, surrounding by a dusty shell which probably corresponds to the PDR.

Molecular hydrogen through its IR rotational transitions is also an important coolant in photodissociation regions, and thereby a particularly well suited tracer of the fluorescently gas. The first pure rotational lines (e.g., 0-0 S(0) and S(1)) essentially result from collisional excitation, since their upper states are relatively low lying and their critical densities are low even at low temperatures, where these line intensities depend mainly on the gas temperature at the photodissociation front.

On the other hand, high rotational and ro-vibrational lines (e.g., 1-0 S(1)) result essentially from the decay of electronically excited states that are pumped through the absorption of FUV photons, where UV pumping could also con-

tribute significantly to the excitation of the pure rotational 0-0 S(2)-S(5) lines, since their upper states are relatively high and their critical densities are high even at moderate temperatures.

Habart et al. (2011) also use Spitzer spectroscopic observations to detect H<sub>2</sub> pure rotational lines emission in PDRs. A single temperature cannot describe the full set of observed H<sub>2</sub> line intensities, where a combination of at least two H<sub>2</sub> gas components, with one cool/warm ( $\sim 100 - 300$  K) and another warm/hot ( $\sim 300 - 700$  K) with much lower column densities is required to explain the distribution. This is in agreement with our estimations of from the two-temperature LTE fit for the SW lobe of N63A.

We compare the results of the observed H<sub>2</sub> emission in the SW lobe of N63A with the shock models (see Figure 3.10). We found that a slow C-shock of  $v_s = 10$  km s<sup>-1</sup> and density  $\sim 10^5$  cm<sup>-3</sup> gives a good fit to the lower excitation lines of the SW lobe of N63A. The ortho-to-para ratios derived are about 1 for the cool/warm component, which is also in agreement with the results of Habart et al. (2011). The non-equilibrium behavior has already been noted in ISO observations of PDRs.

On the other hand, we did not find a model which fit well to the warm/hot component. For future work, to investigate the physical conditions in the SW lobe, we will compare the observed emission lines to PDR models.

Caulet et al. (2012) determine a pressure of  $\sim 7.7 \times 10^{-10}$  dyn cm<sup>-2</sup> using the electron density  $n_e = 384$  cm<sup>-3</sup> and electron temperature  $T_e = 14640$  K derived from the optical line intensities ([S II] and [O II], respectively) obtained in the SW lobe of N63A. Then, its warm atomic region (PDR) has a density of  $n_H = 10^4$  cm<sup>-3</sup>, assuming pressure equilibrium with the ionized gas. Also it is calculated the atomic gas temperature at the PDR surface, which corresponds to  $\sim 1000$  K.

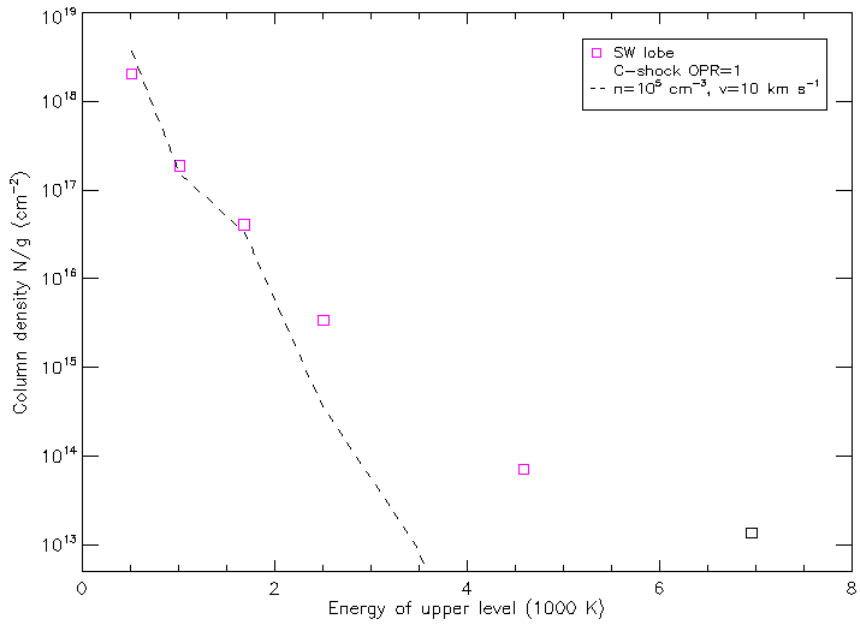


Figure 3.10: *C-shock* fitted to the observed excitation of  $H_2$  in the warm component for the SW lobe of N63A. The dashed line shows the contribution of the slower shock.

# Chapter 4

## SNR N63A clues to its Progenitor

### 4.1 Introduction

Supernovae shape the ISM, chemically enrich their host galaxies, and generate powerful interstellar shocks that drive future generations of star formation. The shock produced by a SN event acts as a type of time machine, probing the mass loss history of its progenitor. In this regard, SNRs can probe a much earlier stage of stellar evolution as they interact with the bulk of the circumstellar material expelled by its progenitor (structures up to several pc in size) during pre-SN mass loss over much longer timescales (several thousands to millions of years before the explosion).

Massive stars can easily lose their mass thanks to their large luminosities which make the radiation pressure in their envelope high. This means that there must be the circumstellar medium (CSM) originated from the evolution of its progenitor around core-collapse SN. The massive stars lose mass via various forms of stellar winds as they evolve. Firstly, a massive star loses mass via a

fast stellar wind during its main sequence (MS) stage, and the stellar wind sweeps up the ambient ISM to form a bubble (e.g. McKee et al., 1984). After the star evolves off the MS, this can lose mass via a slow wind at the red supergiant (RSG) stage or via violent outbursts at the luminous blue variable (LBV) phase. Finally, at the blue supergiant (BSG) or the Wolf-Rayet (WR) phase, fast stellar wind can sweep up the surrounding stellar material into a circumstellar shell. Following the explosion of a massive star, the SN ejecta expands outward and encounters the relics from previous episodes of stellar mass loss.

To connect the remnant properties to those of the progenitor often involves a detailed analysis of the remnant’s broadband spectrum combined with comparisons to hydrodynamical models for SNR ejecta evolution. In particular, the bulk properties, such as: emission line strengths, energy centroids, and chemical abundances depend on different aspects of a SN explosion.

In this chapter, we studied the environment of SNR N63A in order to investigate its interaction with its ambient medium.

## 4.2 SNR N63A’s environment

SNR N63A is a remnant embedded within the classical H II region, N63, with dimensions of  $\sim 6' \times 9'$ . N63A is not the only SNR very close to an H II region in the LMC; in fact, the massive stars that ionize the H II regions are the same that result in supernova, as shown by the massive Population I stars that dominate most environments surrounding SNRs in the LMC (Chu & Kennicutt, 1988).

Besides, N63A corresponds to a core-collapse SNR with a radius smaller than 10 pc and an age of  $2 - 5 \times 10^3$  yr (Hughes et al. 1998). This remnant is believed to be the product of the SN explosion of one of the most massive stars in the OB association, NGC 2030. The progenitor of N63A’s supernova

was probably more massive than  $40M_{\odot}$  and with a main sequence spectral type earlier than O7 (Oey 1996), which explodes in a dense and complex environment (Shull, 1983; Hughes et al., 1998).

Table 4.1: *Brightest members of NGC 2030.*

ID	RA <sup>1</sup>	DEC <sup>2</sup>	log $T_{eff}$	$M_{bol}$	E(B-V)	Sp. Type	V	B-V	U-B
D243-1a	41.27	02 36.9	4.46	-8.6	0.11	B0 Ib	12.82	-0.13	-0.99
D243-1b	41.27	02 36.9	4.52	-8.3	0.11	O9.5 III	13.62	-0.13	-0.99
D243-2	32.26	02 38.0	4.60	-9.4	0.10	O7 III	13.07	-0.22	-1.04
D243-3	35.21	01 45.9	4.52	-9.0	0.23	O9.5 III	13.37	-0.07	-0.94
D243-4	44.57	03 21.0	4.32	-6.7	0.09	B1 III	13.98	-0.17	-0.96
D243-5	36.27	01 14.8	4.56	-8.0	0.03	O7 I	13.98	-0.30	-0.86
D243-6	36.68	02 02.9	4.58	-8.3	0.08	O8 V	14.01	-0.23	-1.01
D243-7	32.08	01 29.2	4.52	-7.8	0.12	O9.5 III	14.15	-0.18	-1.01
D243-9	27.73	02 38.3	4.56	-7.8	0.11	O9 V	14.36	-0.20	-1.01
D243-10	30.55	02 48.0	4.38	-6.8	0.15	B1 V	14.52	-0.11	-1.00
D243-12	54.18	03 30.2	4.58	-8.0	0.19	O8 V	14.55	-0.12	-1.00
D243-14	46.81	02 30.6	4.40	-6.3	0.08	B0.5 V	14.95	-0.20	-0.96
D243-15	40.73	01 14.8	4.54	-7.2	0.13	O9.5 V	14.98	-0.17	-0.96
D243-16	31.24	02 36.5	4.56	-7.1	0.10	O9 V	15.08	-0.21	-1.01
D243-17	36.33	01 15.5	4.25	-5.0	0.11	B2.5 III-V	15.34	0.51	-1.83
D243-18	34.91	02 07.9	4.56	-6.8	0.09	O9 V	15.37	-0.22	-1.00
D243-35	28.04	03 15.2	4.34	-4.5	0.07	B1.5 V	16.29	-0.18	-0.81

<sup>(1)</sup> RA:  $05^h 35^m$  (J2000). The values correspond to seconds (s).

<sup>(2)</sup> DEC:  $-66^{\circ}$  (J2000). The values correspond to arcminute (') and arcsecond (").

The OB association NGC 2030 has been studied in some previous researchs. The table 4.1 shows the spectroscopic and photometric data for the most luminous members of this OB association ( $V < 16.3$  mag), obtained from Oey (1996)

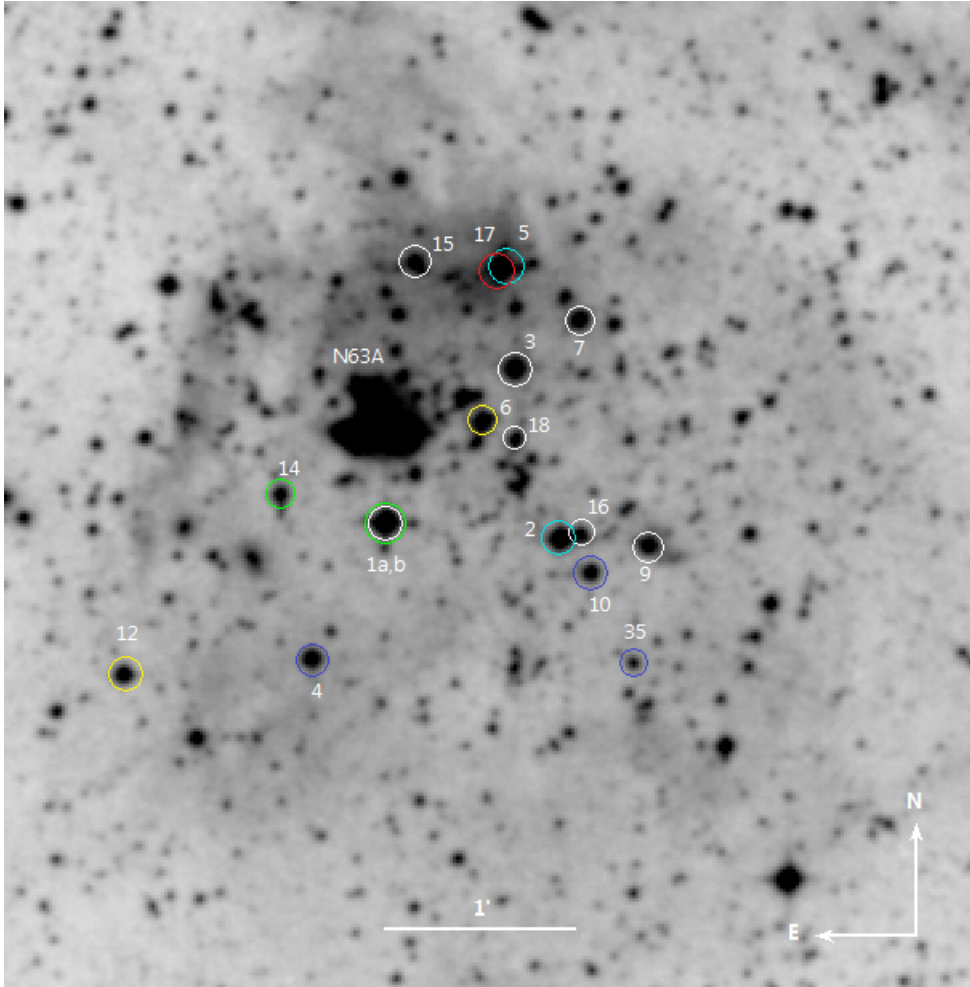


Figure 4.1: *Optical nebula of N63A and the brightest members of the OB Association NGC 2030 in R band, from AAO. The spectral types of the stars are shown in different colors: O7 (cyan), O8 (yellow), O9 (white), B0 (green), B1 (blue) and B2 (red).*

and Oey (1996a). Figure 4.1 shows the positions of these OB stars around the optical nebula of N63A.

As mentioned by Chu (1997), the evolution of a middle-age SNR is highly dependent on whether its progenitor star was isolate or in an OB association, because the further evolution would be dictated by the interstellar environment, which has been modified by the progenitor massive star, as well as the neighboring stars (i.e. by the OB association collectively).

We believe that the N63A's progenitor lost much of its mass during its life before the SN explosion, due to fast MS winds, slow RGS winds and probably fast WR winds. Consequently, accreting materials may exist around N63A.

### 4.3 Observational Data

We used the MCELS H $\alpha$  narrowband observation (Smith, 1996), which was carried out with the 0.6 m Cerro Tololo Inter-American Observatory (CTIO) Curtis Schmidt telescope, equipped with a SITe 2048 x 2048 CCD, with a pixel scale of 2.4". The specifications of the H $\alpha$  narrow-band filter are:  $\lambda_c = 6563 \text{ \AA}$  and  $\Delta\lambda = 30 \text{ \AA}$ . The mosaicked image have a pixel size of 3". We subtract the stars and calibrate by flux the image using the standard procedure.

We also used the high-resolution H $\alpha$  image, which was obtained with the MOSAIC II camera on the Blanco 4-m telescope at the CTIO.

### 4.4 Results and Discussion

For SNRs inside an H II region without a superbubble structure, the H $\alpha$  image would show diffuse emission around the SNR. On the other hand, the presence of a superbubble can be recognized by the ring-nebula morphology in the H $\alpha$  images (Chu, 1997).

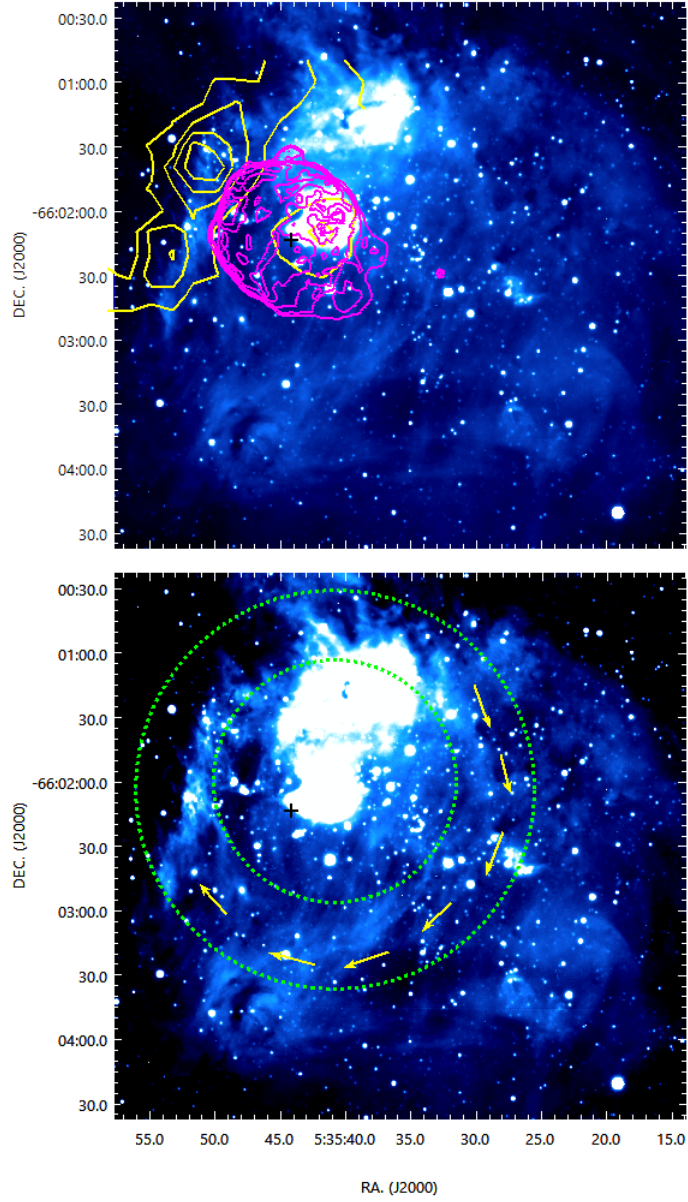


Figure 4.2:  $H\alpha$  emission of the N63 HII region. The upper panel shows the Chandra X-ray contours (magenta) which define the size of the SNR N63A with a radius of  $\sim 8.5$  pc. Also  $^{12}\text{CO}_{2-1}$  contours (yellow) are overlaid. The lower panel shows a “ring-like” structure (indicated by the arrows in yellow) around the SNR N63A.

We examined an  $H\alpha$  narrow-band image of the N63 HII region to find some kind of pattern indicating the presence of an accreting material surrounding the SNR N63A. We identified a kind of half “ring-like” structure around the SNR N63A (see Figure 4.2, lower panel). We cannot see this structure towards the eastern border of the HII region. This is probably due to the presence of molecular clouds which blocks the  $H\alpha$  emission of the H II region (see Figure 4.2, upper panel).

We can interpret this “ring-like” structure as a wind material confined by the ambient pressure. The ring structure appears clumpy and elliptical, features not normally associated with airy diffraction rings or artifacts of filter reflections or scattering.

Thereafter, we investigated how the  $H\alpha$  brightness varies through the H II region to check if this material correspond to the N63A’s progenitor. For this reason, we measured the brightness variation following a radial distribution, which is shown in Figure 4.3.

Table 4.2 shows in column (2) the direction of the path in which the brightness variation was measured, and in column (4) the peak of the brightness distribution across the N63 H II region, which correspond to the structure indicated in Figure 4.2. The brightness was not corrected by extinction. The distance in column (3) is estimated using as reference the center of the SNR N63A ( $\alpha$ :  $05^h 35^m 44.1^s$ ,  $\delta$ :  $-66^\circ 02' 14''$ , J2000).

The peak measured in different paths shows a similar value,  $\sim 2 \times 10^{-5}$  erg  $\text{cm}^{-2} \text{s}^{-1} \text{sr}^{-1}$ , as well as the distance at which is measured the peak brightness in the “ring-lik” structure. The distance to the peak position across the X1 path is shorter than through the other paths. However, this distribution is measured towards the location of molecular clouds which may affect the expansion of this material.

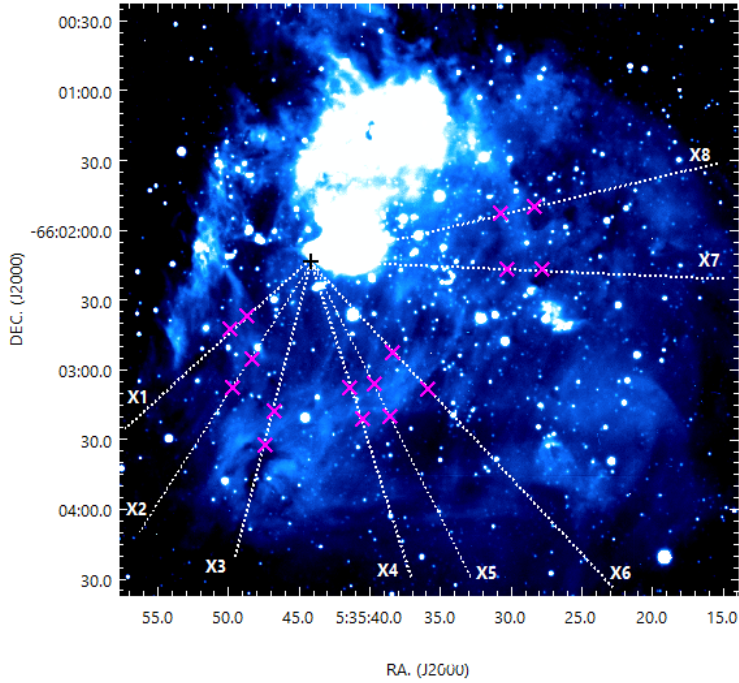


Figure 4.3: *The imagen indicates the paths where the  $H\alpha$  brightness distribution was measured (dotted lines) across the  $H\ II$  region. The  $x$  in magenta delimit the regions where the peak in the brightness variation was identified within the “ring” structure. The black cross indicates the center of the SNR N63A.*

Figure 4.4 shows the brightness distribution across the paths indicates in Figure 4.3. The plots show that the  $H\alpha$  brightness decreases as we move far away from the N63A’s optical nebula. The brightness variation was plotted from 8 pc to 36 pc (measured from the center of the SNR) to avoid measuring the emission of the N63A’s optical nebula. Following the peak identified as the ring structure, other secondary peaks are detected.

Table 4.2: *Brightness distribution of the H $\alpha$  emission through the N63 HII region.*

Path	Angle	Distance	Peak Brightness
		pc	erg cm <sup>-2</sup> s <sup>-1</sup> sr <sup>-1</sup>
X1	223°	10.8	1.67 x 10 <sup>-5</sup>
X2	237°	13.0	1.63 x 10 <sup>-5</sup>
X3	255°	16.4	2.08 x 10 <sup>-5</sup>
X4	288°	14.7	2.04 x 10 <sup>-5</sup>
X5	297°	14.7	2.19 x 10 <sup>-5</sup>
X6	313°	13.6	2.13 x 10 <sup>-5</sup>
X7	358°	19.8	1.75 x 10 <sup>-5</sup>
X8	13°	18.6	2.07 x 10 <sup>-5</sup>

Based on these results it is difficult to determine which is the origin of this ring structure. It is possible that this structure corresponds to circumstellar material produced by the mass loss of the N63A's progenitor. Also, this structure could be product of the neighboring OB stars, due to these massive stars can be losing mass by fast and strong stellar winds. However, the N63A's progenitor was a more massive star, which evolved faster than the other OB stars of this association. Due to its large mass, we expect that the N63A's progenitor lost mass in many stages during its evolution (e.g. MS, RSG, WR). Therefore, the contribution of the N63A's progenitor to the ambient medium is probably dominant compared with the contribution of the others OB stars. Another possibility is that this structure is part of the ISM and is not related to the SNR.

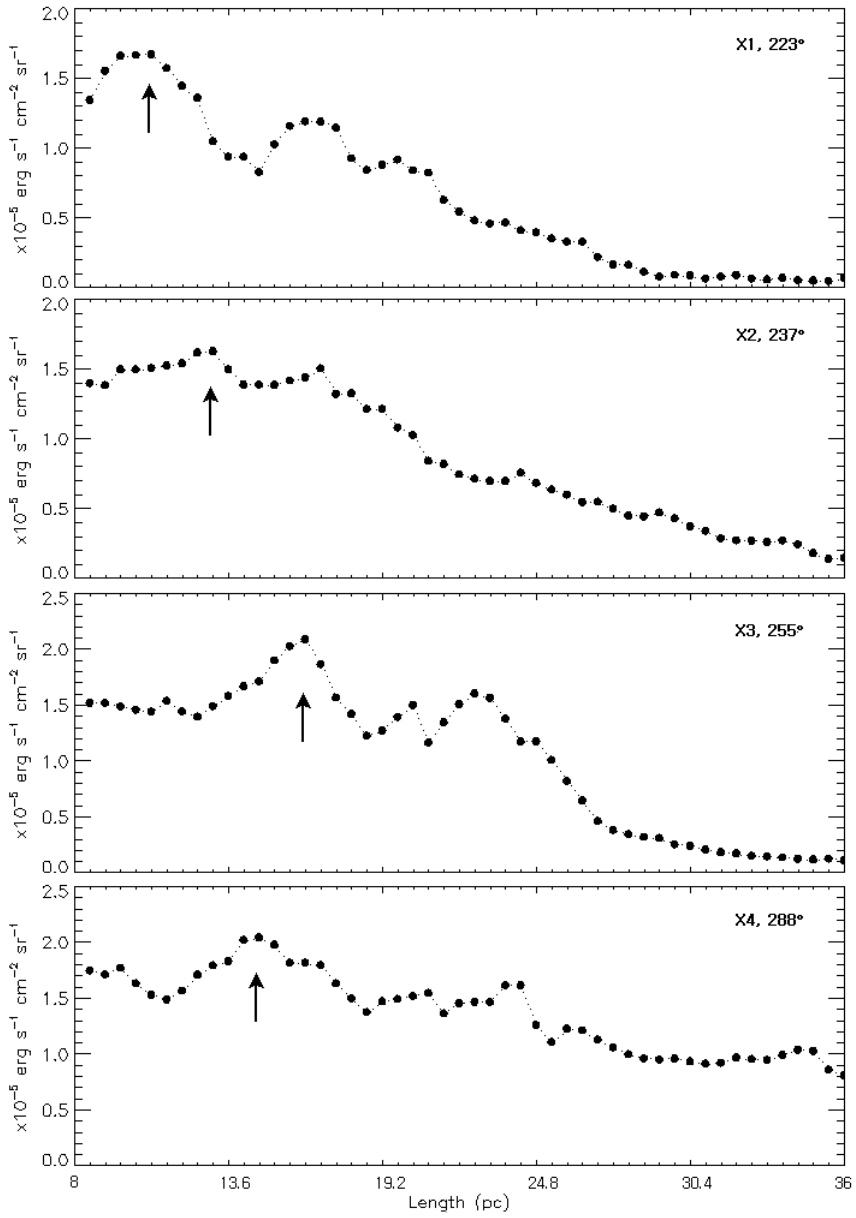


Figure 4.4: *Plots showing the  $H\alpha$  brightness variation across the N63 H II region. The path distributions are indicated in Figure 4.3. The arrows marks the peak of the brightness which corresponds to the ring structure indicated in Figure 4.2.*

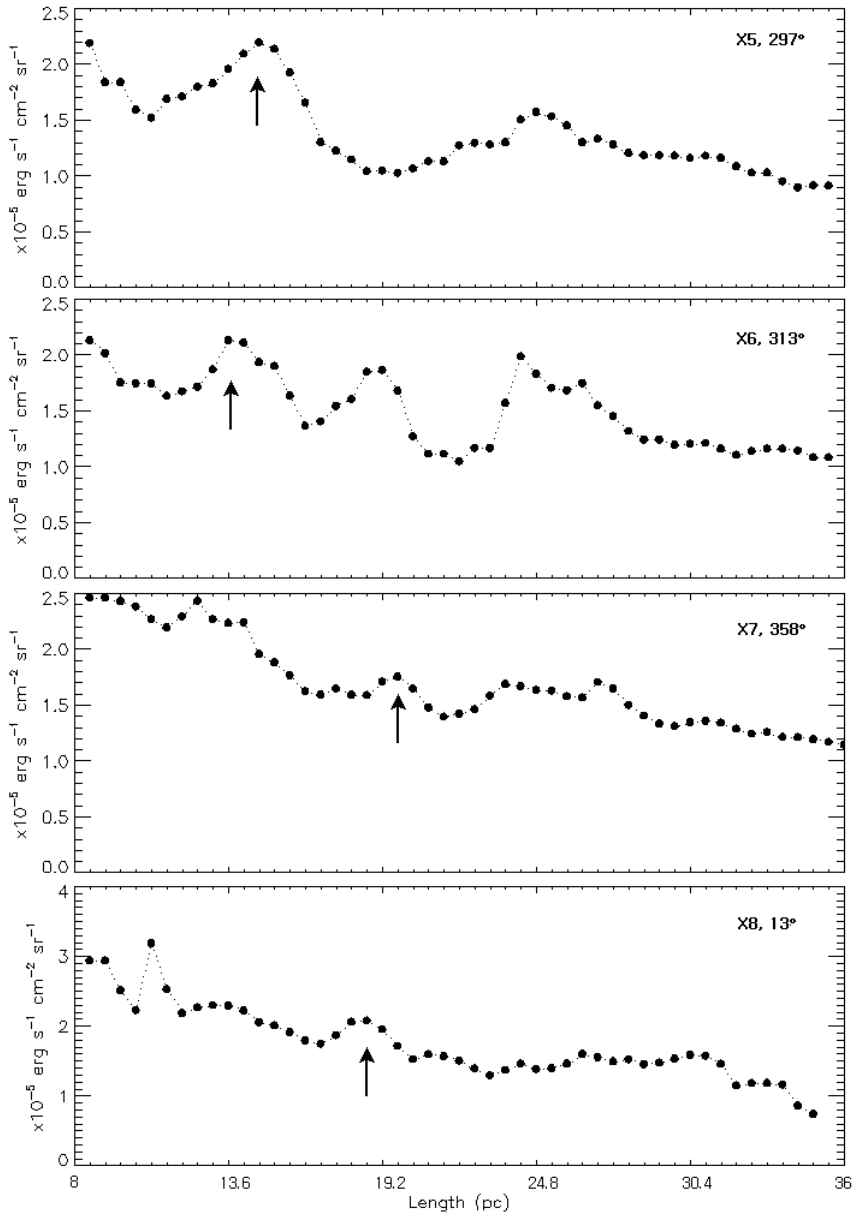


Figure 4.4: *Continued.*

However, we can analyze some puzzling properties of SNR N63A which may to give us some clues about this subject. For example, the discrepant optical and X-ray sizes in N63A, where the X-ray size of N63A is almost three times larger than the size of its optical nebula. Chu (1997) explained this property based on the case that the supernova progenitor are in a bubble. Thus, the SNR may be interacting mostly with the inner wall of the bubble, producing detectable X-ray emission but not optical emission; only dense, shocked cloudlets produce detectable optical emission.

Furthermore, the winds of hot stars are characterized by two global parameters, the terminal velocity  $v_w$  and the rate of mass-loss  $\dot{M}$ . Since these winds are initiated and then continuously accelerated by the absorption of photospheric photons in spectral lines, the velocity  $v_w$  reached at very large distances from the star (where the radiative acceleration approaches zero because of the geometrical dilution of the photospheric radiation field) corresponds to the maximum velocity of the stellar wind. If we assume that winds are stationary and spherically symmetric, then the equation of continuity yields at any radial coordinate  $r$  in the wind:  $\dot{M} = 4 \pi r^2 n_w \mu_H v_s$ .

Massive luminous OB stars, like the N63A's progenitor, have strong stellar winds. In the case of fast and strong winds in the MS phase which produces interstellar bubbles, the characteristic parameters correspond to a mass-loss rate of  $\dot{M} \leq 10^{-5} M_\odot \text{ yr}^{-1}$ , a velocity of  $v_w \geq 1000 \text{ km s}^{-1}$  and a bubble radius of  $\sim 28 \text{ pc}$ , for stars with spectral types between B0 and O4 (McKee et al. 1984). For slow and strong winds in the RSG phase, the characteristic parameters are a mass-loss rate of  $\dot{M} \leq 10^{-4} M_\odot \text{ yr}^{-1}$ , a velocity of  $v_w \sim 15 \text{ km s}^{-1}$  and a RSG wind radius of  $\leq 10 \text{ pc}$ . Finally, for fast and strong winds in WR phase, which produce circumstellar bubbles, the characteristic parameters correspond to a mass-loss rate of  $\dot{M} \geq 10^{-5} M_\odot \text{ yr}^{-1}$ , a velocity of  $v_w \sim 2000$

km s<sup>-1</sup> and a bubble of  $\geq 10$  pc radius surrounded by a thick fragmented RSG shell.

As a future work, we want to study the density variation through the H II region to constrain if the structure detected in this research corresponds to circumstellar material produced by the mass loss of the N63A's progenitor, or if it is product of some artifact seen in the H $\alpha$  emission. Additionally, it might be useful to check if this filament structure is seen in other wavelengths.

# Chapter 5

## Summary and Conclusion

The SNR-MC interaction in N63A offers the opportunity to investigate the dynamics of shocks, molecular astro-chemistry, and high-energy phenomena in shocks and dense environment in an unbiased sampled which has been covered widely in other wavelengths.

We carried out a multi-wavelength study of SNR N63A in the LMC, which is a young remnant of the SN explosion of one of the most massive ( $> 40 M_{\odot}$ ) stars in a cluster. This remnant is currently expanding within a large H II region formed by OB stars in the cluster and engulfing a molecular cloud.

In the first part we carry out a research using the NIR imaging and spectroscopic observations of SNR N63A, which allowed us to obtain physical parameters and investigate the atomic shocks. From the [Fe II] narrowband images we detect the emission from a two-lobed structure, where its location and distribution is coincident with the shock-heated lobes of the N63A's optical nebula. Using an  $[\text{Fe II}]_{1.26/1.64\mu\text{m}}$  ratio map we derive a visual extinction of  $A_V \sim 0$  to 0.5 mag, which is lower than values obtained in previous researches. Also, the

[Fe II] ratio map shows an internal region which exhibits a lower [Fe II] ratio ( $\sim 1.3$ ). It is probably that this characteristic can be product of the molecular cloud which is swept-up by the SNR and has a good spatial correlation with the N63A's optical nebula.

Additionally, we used the detected [P II] emission to create a [P II] 1.19/[Fe II] 1.26  $\mu\text{m}$  ratio map used to study the shock processing of dust in this region. We calculated a  $x(\text{P})/x(\text{Fe}) \approx 0.05 \pm 0.005$ , which is 6 times higher than the cosmic abundance,  $x(\text{P}/\text{Fe})_{\odot}$ . This indicates that the emitting gas has recently passed through a fast shock which sputtered and destroyed large percentage of the dust grains.

Moreover, we detected many [Fe II] lines in the spectroscopic observations of N63A. We used these lines to obtain density diagnosis of the emitting region, because the [Fe II] lines can probe much higher densities compared with optical density-sensitive lines. We estimated a mean electron density of  $n_e \sim (4.7 \pm 0.7) \times 10^3 \text{ cm}^{-3}$  in the emitting region. If we assume that the shock speed is  $\sim 100 \text{ km s}^{-1}$ , the pre-shock density of the emitting gas corresponds to  $n_0 \sim 30 \text{ cm}^{-3}$ . The pressure obtained from the NIR [Fe II] lines corresponds to  $\sim 6.5 \times 10^{-9} \text{ dyn cm}^{-2}$ . These shock properties seems to explain roughly the observed parameters of the [Fe II] emission and the destruction of the dust grains.

In the second part we study the SNR- molecular cloud interaction. First, we identified three clouds in the N63A region using the integrated SEST  $^{12}\text{CO}_{2-1}$  emission line. The cloud identified as cloud 3 has a good spatial correlation with the N63A's optical nebula, and as predicted in previous studies, it would be consistent with a molecular cloud being swept-up by the SNR. Thus, the interaction SNR-MC is limited to the central portion of the SNR, as has been reported in some galactic SNRs. Additionally, two other clouds were identified near the east rim of the SNR, which seems to be interacting with the H II

region.

We also estimated the physical parameters of the clouds. For cloud 3 we reported a mass of  $\sim 1.2 \times 10^3 M_{\odot}$ , which is almost three times larger than the previous mass reported using X-ray observations, and a hydrogen column density of  $N_H \sim 1.4 \times 10^{21} \text{ cm}^{-2}$ , which is 4 times smaller than the total column density derived using our NIR observations. The uncertainties can be product of the detection of diffuse material, which maybe it is not detected in the X-ray observations, and mainly the  $X_{CO}$  factor used to estimate the mass from the CO emission, which has a wide range of values reported. If we adopt the large LMC  $X_{CO}$  factor reported by Cohen et al. (1988), we obtain  $N_H \sim 3.8 \times 10^{21} \text{ cm}^{-2}$ , which is more comparable to the total column density derived from NIR lines.

Besides,  $H_2$  emission lines are detected toward the optical nebula region of N63A, indicative of radiative cooling from shocks interacting with dense clouds. We found that the excitation of the  $H_2$  lines are explained by two components: a warm component, with temperatures in the range 200 - 300 K, and column densities of  $\sim 10^{19} \text{ cm}^{-3}$ ; and a hot component, with temperatures between 700 to 900 K and column densities  $\sim 10^{18} \text{ cm}^{-3}$ . Slow C-shocks with  $OPR \sim 3$  seems to reproduce well the excitation of the warm component in the shock-heated regions (SE and NE). The hot component is still unclear. Future studies require to compare the emission of the high excitation lines to fast C-shocks. Using different C-shock models we obtained a pressure range from  $9 \times 10^{-9}$  to  $2 \times 10^{-6} \text{ dyn cm}^{-2}$ , where the lower limit is comparable to the pressure obtained from ionic lines.

In the case of the SW lobe, a less dense  $\sim 10^5 \text{ cm}^{-3}$  with an  $OPR= 1$  seems has the best fit to the warm component of the Boltzmann distribution. For future work, we will compare the observed emission lines in the SW lobe with

PDR models to investigate the physical conditions in the photoionized region.

Additionally, we examine the  $H_{22.12\mu m}$  emission detected in N63A, which is located in a region which has a good spatial correlation with the emitting region of  $[Fe II]_{1.64\mu m}$ , even though the  $H_{22.12\mu m}$  emission is one order more fainter than the  $[Fe II]$  emission demonstrating that the molecular and ionic shocks arise from the same region. Also, the peak of the  $H_{22.12\mu m}$  emission is detected in the SE lobe, whilst the peak of the  $[Fe II]$  emission is detected in the NE lobe. However, we interpret that Fe II and  $H_2$  emission are tracing independent shocks in N63A based on physical parameters. On the one hand, Fe II traces fast, grain-destroying shocks into  $n < 10^3 \text{ cm}^{-3}$  gas, while  $H_2$  traces denser shocks,  $n > 10^3 \text{ cm}^{-3}$ , and their correspondence on the sky probably reflects the preshock structure of the molecular cloud.

Finally, we studied the environment of SNR N63A in order to investigate its interaction with its ambient medium. We believe that the N63A's progenitor lost most of its mass via various forms of stellar winds while evolving. Consequently, accreting material may exist around N63A. We found a half "ring-like" structure with an average brightness of  $\sim 2 \times 10^{-5} \text{ erg cm}^{-2} \text{ s}^{-1} \text{ sr}^{-1}$  in  $H\alpha$ , at a distance of 11 - 19 pc from the center of the SNR. This structure can correspond to circumstellar material produced by the mass loss of the N63's progenitor or by the neighboring OB stars. Another possibility is that this structure is part of the ISM and it is not related to the SNR.

The study of MC-SNR interactions is advancing rapidly because of multi-wavelength observations, where the strong correlations among them provide opportunities to discover true samples of SNRs interacting with clouds, one example of them is N63A.

The NIR spectra used in this investigation did not have enough resolution to study the kinematics in N63A. Therefore, it is necessary a high-spectral

resolution map in IR wavelengths to study this subject, which it would be a good opportunity considering the different components of this SNR.

Also, due to absence of high angular and kinetic resolution images of the molecular CO emission, we cannot reveal the detailed structure of the shocked cloud. In this regard, we are sure that future sub-millimeter observations of N63A can reveal unambiguously the internal structure of the shocked cloud, and the kinematical consequences of the impact.

# Bibliography

- [1] Anderl et al., 2014, *A&A*, 569, 81.
- [2] Arendt, R. G., 1989, *ApJS*, 70, 181.
- [3] Banas et al., 1997, *ApJ*, 480, 607.
- [4] Caulet et al., 2008, *ApJ*, 678, 200.
- [5] Caulet, A. & Williams, R.M, 2012, *ApJ*, 761, 107 (and references therein).
- [6] Cohen et al., 1988, *ApJ*, 331, L95.
- [7] Cohen et al., 2003, *AJ*, 126, 1090.
- [8] Chu, Y.H. & Kennicutt, Jr. R.C., 1988, *AJ*, 96, 1874.
- [9] Chu, Y. H., 1997, *AJ*, 113, 1815.
- [10] Davies, R. D., Elliott, K. H. & Meaburn, J., 1976, *MmRAS*, 81, 89.
- [11] Desai et al., 2010, *AJ*, 140, 584.
- [12] Dickel et al., 1993, *A&A*, 275, 265.
- [13] Dobashi et al., 2008, *A&A*, 484, 205.

- [14] Draine et al., 1983, ApJ, 264, 485.
- [15] Draine, B. T. 2003, ARA&A, 41, 241.
- [16] Dubner et al., 2004, A&A, 426, 201.
- [17] Dwek, E. 1998, ApJ, 501, 643.
- [18] Froebrich, D. et al., 2015, MNRAS, 454, 2586.
- [19] Garcia Lopez et al., 2010, A&A, 511, AA5.
- [20] Habart et al., 2011, A&A, 527,A122.
- [21] Henize, K.G., 1956, ApJS, 2, 315.
- [22] Hewitt et al., 2009, ApJ, 694, 1266 (and references therein).
- [23] Hollenbach, D. J., & McKee, C. F. 1989, ApJ, 342, 306.
- [24] Hughes, J.P., Hayashi, I. & Koyama, K., 1998, ApJ, 505, 732.
- [25] Hughes et al., 2010, MNRAS, 406, 2065.
- [26] Imara & Blitz, 2007, ApJ, 662, 969.
- [27] Israel et al., 1993, A&A, 276, 25.
- [28] Jiang et al. 2010, ApJ, 712, 1147.
- [29] Johansson, S., 1978, Phys. Scripta, 18, 217.
- [30] Jones, A. P., Tielens, A. G. G. M., & Hollenbach, D. J., 1996, ApJ, 469, 740.
- [31] Jones, A. P., 2004, Astrophysics of Dust, 309, 347.

- [32] Kim et al., 2003, ApJS, 148, 473 (and references there in).
- [33] Kim, C.G. & Ostriker, E. C., 2015, ApJ, 802, 99.
- [34] Koo, B.-C. & Moon, D.-S., 1997, ApJ, 485, 263.
- [35] Koo et al., 2001, ApJ, 552,175.
- [36] Koo, B. C., Raymond, J. C. & Kim, H. J., 2016, JKAS, 49, 109 (and references therein).
- [37] Levenson et al., 1995, AJ, 110, 739.
- [38] Lucke, P.B & Hodge, P.W., 1970, AJ, 75, 171.
- [39] Mathewson, D.S. & Healey, J.R., 1964, IAUS, 20, 283.
- [40] Mckee, C. F. & Hollenbach, D. J., 1980, ARA&A, 18, 219.
- [41] McKee, C. F., Chernoff, D. F. & Hollenbach, D. J., 1984, ASSL, 108, 103.
- [42] McKee et al., 1984, ApJ, 278, L115.
- [43] Nussbaumer, H., & Storey, P. J., 1988, A&A, 193, 327.
- [44] Oey, M.S., 1996, ApJ, 465, 231.
- [45] Oey, M.S., 1996a, ApJS, 104,710.
- [46] Oliva, E., Moorwood, A. F. M. & Danziger, I.J, 1989, A&A, 214, 307 (and references therein).
- [47] Oliva et al., 2001, A&A, 369, L5.
- [48] Reach, W. T., & Rho, J., 1996, A&A, 315, L277.
- [49] Reach, W. T. & Rho, J., 1999, ApJ, 511, 836.

- [50] Reach et al., 2005, ApJ, 618, 297.
- [51] Reach, W. T., et al. 2006, AJ, 131, 1479.
- [52] Rho et al., 2017, ApJ, 834, 12R.
- [53] Russell, S.C. & Dopita, M.A., 1990, ApJS, 74, 93.
- [54] Sakamoto et al., 1994, ApJ, 425, 641.
- [55] Saken, J. M., Fesen, R. A., & Shull, J. M. 1992, ApJS, 81, 715.
- [56] Schenck et al., 2016, AJ, 151, 161S.
- [57] Seok et al., 2013, AJ, 779, 134.
- [58] Seta et al., 1998, ApJ, 505, 286.
- [59] Shinn et al., 2010, AdSpR, 45, 445.
- [60] Shull, P., 1983, ApJ, 275, 592.
- [61] Shull, J. M. & Draine, B. T., 1987, ASSL, 134, 283.
- [62] Staveley-Smith et al., 2003, MNRAS, 339, 87.
- [63] Tielens, A. G. G. M. 1998, ApJ, 499, 267.
- [64] van Dishoeck et al., 1993, A&A, 279, 541.
- [65] Warren et al., 2003, ApJ, 583, 260.
- [66] Wilgenbus et al., 2000, A&A, 356, 1010.
- [67] Williams, de Geus & Blitz, 1994, ApJ, 428, 693.
- [68] Williams et al., 2006, AJ, 132, 1877.
- [69] Yamaguchi et al., 2001, AJ, 553, L185.

## 초록

SNR의 성질과 물리적 환경은 다양하기 때문에, 근거리 SNR의 특성을 이해하는 것은 우리가 분해할 수 없는 먼 거리의 은하의 SNR에서의 방출을 해석하는 데 유용하다. 이런 점에서, LMC는 그 근접성, 위치, 조성으로 인해 우리 은하와 비교해서 SNR을 연구할 수 있는 유일한 장소이다.

본 연구에서는 LMC에서 SNR N63A에 대해 다중파장 연구를 수행했다. N63A는 성단에서 가장 무거운 별 ( $> 40 M_{\odot}$ )의 초신성 폭발의 젊은 잔해이다. 그리고 현재는 성단 내 OB형 별에 의해 생성된 거대한 H II 영역에서 팽창하고 있으며, 분자운을 에워싸고 있다.

먼저, 본 연구에서는 근적외선 영상 및 분광 관측을 통해서 N63A의 전체적인 구조를 연구했다. [Fe II] 영상에서 두 개의 로브 구조가 발견되었으며, 이 구조는 N63A의 광학 성운의 충돌 가열된 로브와 좋은 공간적 상관관계를 보였다. 또한, 본 연구에서는 방출 영역으로부터 몇 개의 [Fe II] 선뿐만 아니라, He I, H I 그리고 [P II] 선을 검출했으며, 이로부터 전자 밀도 ( $\sim 4700 \text{ cm}^{-3}$ )와 작은 소광 ( $A_V \sim 0.5 \text{ mag}$ )을 추정할 수 있었다. 또한, SNR의 [Fe II] 방출 영역 내에서 충격파의 속도를  $100 \text{ km s}^{-1}$ 로 가정할 때, 충돌 전의 개수 밀도는  $\sim 30 \text{ cm}^{-3}$ 으로 추정할 수 있었다.

두 번째로, 본 연구에서는 SNR N63A와 관련된 분자 기체에 대한 연구 결과를 제시하였다. 관측은 SEST  $^{12}\text{CO}$  J= 1-0 및 2-1을 이용하였으며, 이 관측은 초신성 충격파와 인접한 분자운 사이의 물리적 상호 작용이 존재함을 뒷받침하는 증거를 제공한다. 본 연구에서는 SNR N63A와 상호 작용하는 분자운의 질량으로  $\sim 1.2 \times 10^3 M_{\odot}$ 를 얻었으며, 이 질량은 X선 관측을 이용하여 보고된 이전 질량의 약 3 배에 해당된다. 또한 본 연구에서는 SNR N63A와 상호 작용하는 분자운의 수소 기둥 밀도를  $N_H \sim 1.4 \times 10^{21} \text{ cm}^{-2}$ 로 추정했으며, 이 기둥 밀도는 NIR 관측치를

이용하여 얻은 총 기동 밀도보다 4 배가량 작은 값이었다.

또한, NIR 및 MIR 영역에서의 Spitzer IRS 관측을 이용해서, 충격을 받은 H<sub>2</sub> 방출을 감지했다. H<sub>2</sub> 들뜸 그림(excitation diagram)은 200-300 K와 700-900 K의 온도를 갖는 두 가지 온도의 LTE 모형에 가장 잘 맞는 것을 보여줬다. H<sub>2</sub> 방출과 충격파 모형을 을 비교하면 느린 C- shock 모형이 따뜻한 구성 물질과 잘 맞음을 보여준다.

[Fe II] 특징 이외에도, 이 연구에서는 [Fe II] 방출 영역과 공간적인 상관관계가 있는 영역에서 H<sub>2</sub> 2.12  $\mu$  m 방출을 검출했다. 분자와 이온 충격파가 동일한 지역에서 발생하지만, 그들의 특성으로 볼 때 Fe II와 H<sub>2</sub> 방출은 N63A의 서로 다른 충격파를 추적하는 것으로 해석된다.

마지막으로, 주변 물질과의 상호 작용을 조사하기 위해 SNR N63A의 환경을 연구했다. SNR의 중심에서 11 - 19 pc 떨어진 지역에서, H $\alpha$ 에서  $\sim 2 \times 10^{-5}$  erg cm<sup>-2</sup> s<sup>-1</sup> sr<sup>-1</sup>의 평균 밝기를 가지는 반 “고리 모양”의 구조를 발견했다. 이 구조는 N63A의 이전 천체의 질량 손실에 의해 생성되었거나, 주변의 OB형 별에 의해 생성된 물질일 수도 있다. 또 다른 가능성으로는, 이 구조가 성간 물질의 일부이거나, SNR과 관련이 없다는 것이다.

**주요어:** 성간물질: 초신성 잔해 - 성간물질: 개별 천체 (N63A) - 성간물질: 분자운  
**학번:** 2015-22234



